

OKINAWA INSTITUTE OF SCIENCE AND TECHNOLOGY
GRADUATE UNIVERSITY

Thesis submitted for the degree

Doctor of Philosophy

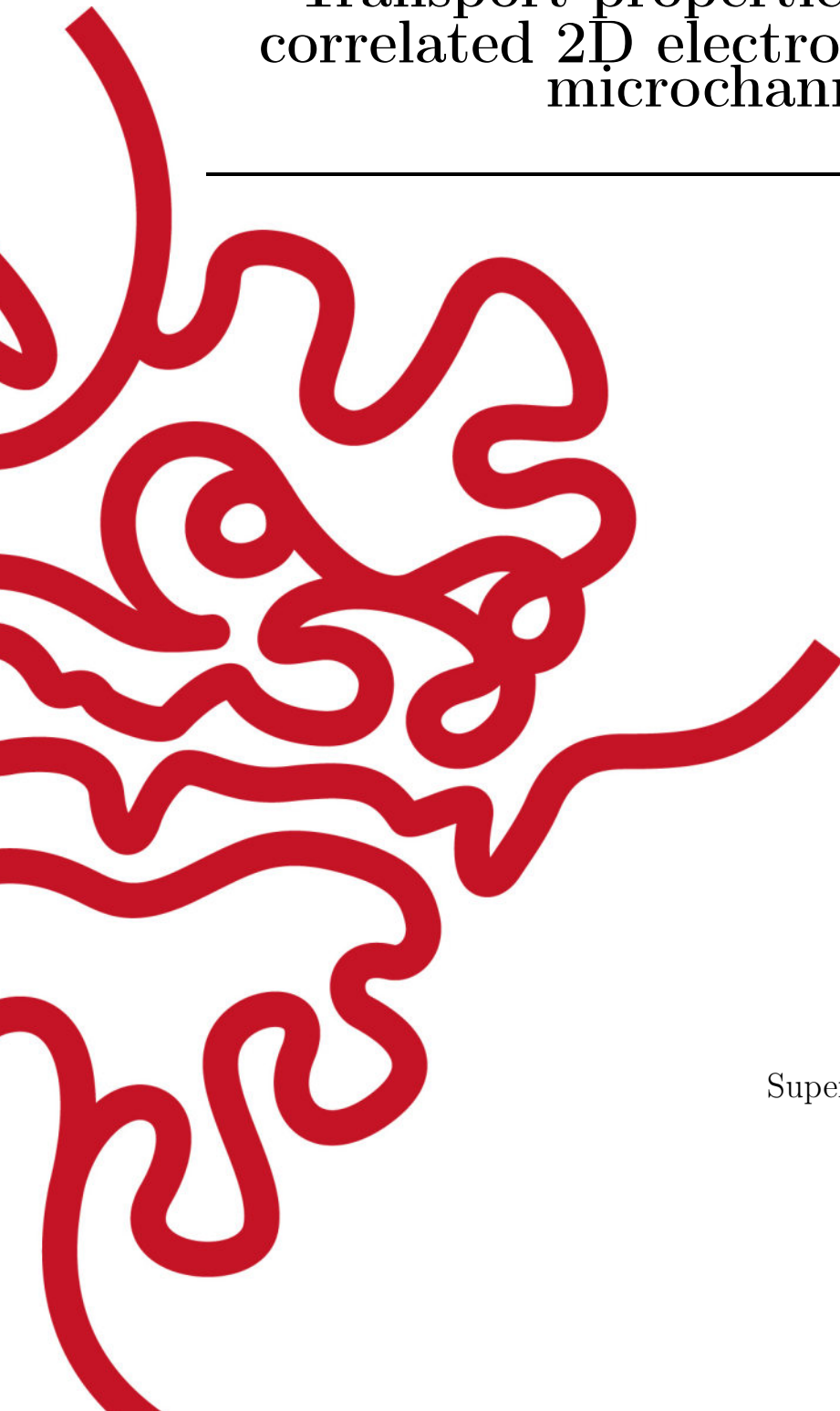
Transport properties of strongly
correlated 2D electrons confined in
microchannels

by

Jui-Yin Lin

Supervisor: **Denis Konstantinov**

September, 2018



Declaration of Original and Sole Authorship

I, Jui-Yin Lin, declare that this thesis entitled *Transport properties of strongly correlated 2D electrons confined in microchannels* and the data presented in it are original and my own work.

I confirm that:

- No part of this work has previously been submitted for a degree at this or any other university.
- References to the work of others have been clearly acknowledged. Quotations from the work of others have been clearly indicated, and attributed to them.
- In cases where others have contributed to part of this work, such contribution has been clearly acknowledged and distinguished from my own work.
- None of this work has been previously published elsewhere, with the exception of the following:

Nonlinear transport of the inhomogeneous Wigner solid in a channel geometry, Physical review B **94**, 195311 (2016) [1]

Sliding of an electron crystal of finite size on the surface of superfluid ^4He confined in a microchannel, Physical review B **98**, 085412 (2018) [2]

Date: September, 2018

Signature:

Abstract

Transport properties of strongly correlated 2D electrons confined in microchannels

Wigner crystal is the solid phase of strongly correlated electrons. The main theme of this thesis work is employing a two-dimensional Wigner solid (WS) formed on the surface of liquid helium to probe interplay between, on the one hand, strong internal forces arising from electron-electron interaction and, on the other hand, external forces due to substrate and applied electrostatic potentials. To accomplish these studies we developed and employed a number of microchannel devices to confine WS system and measure its transport properties. First, we characterize the transport properties of a homogeneous electron crystal, an island of WS, and an inhomogeneous electron crystal in a microchannel geometry. We show how interplay between transport regimes of two individual electron crystals effect the overall I - V curves. A further study of WS system of varied size demonstrates how the energy dissipates from the edges of electron crystal through emission of ripplons, which thus affects the breaking of the strong coupling of WS with substrate excitations. Then, by introducing an external spatial periodic potential, we observed suppression of WS-ripplon coupling and re-entrant melting of WS when the amplitude of external potential is sufficiently high. We interpret these phenomena as arising from the structural phase transitions in WS confined in a microchannel with spatially varied potential. This work is also relevant to the general study of the Frenkel-Kontorova model of interacting particles subject to a periodic substrate potential. Finally, some interesting features in the transport of strongly-correlated electrons have been studied in a T-shaped microchannel geometry. In particular, experiments showed a breakdown of the conventional Drude behaviour at sufficiently low temperatures and high electron densities, which could be due to effect of inertia of the surface excitations coupled to the WS.

Acknowledgment

Theses must acknowledge assistance received in the following areas:

- Designing the research: Denis Konstantinov, Alexander V. Smorodin, Alexander O. Badrutdinov, David Rees
- Sample fabrication: Laszlo Szikszai, Alexander V. Smorodin, Alexander O. Badrutdinov, David Rees
- Executing the research: Alexander V. Smorodin, Alexander O. Badrutdinov, David Rees
- Analyzing the data: Alexander V. Smorodin, Alexander O. Badrutdinov, David Rees
- Interpreting the data/research: Denis Konstantinov, Alexander V. Smorodin, Alexander O. Badrutdinov, David Rees

Abbreviations

2DEG	two-dimensional electron gas
BC scattering	Bragg-Cherenkov scattering
BTE	Boltzmann transport equation
CVD	chemical vapor deposition
DL	dimple lattice
DSF	dynamical structure factor
EBL	electron-beam lithography
EL	electron liquid
FEM	finite element model
FK model	Frenkel-Kontorova model
GS	Ground state
IDC	inter-digital capacitor
KTHNY theory	Kosterlitz-Thouless-Halperin-Nelson theory
MOSFET	metal-oxide-semiconductor field effect transistor
QTT	quantum transport theory
RIE	reactive ion etching
SG equation	sine-Gordon equation
SSE	surface-state electron
WS	Wigner solid

Nomenclature

c	speed of light ($2.997\,924\,58 \times 10^8 \text{ ms}^{-1}$)
\hbar	Planck constant ($1.054\,572\,66 \times 10^{-34} \text{ Js}$)
k_B	Boltzmann constant ($1.380\,658 \times 10^{-23} \text{ JK}^{-1}$)
ϵ_0	permittivity of vacuum ($8.854 \times 10^{-12} \text{ C}^2/(\text{Jm})$)
ϵ_{He}	relative permittivity of liquid helium (1.056 for ^4He , 1.042 for ^3He)
e	electrical charge of electron ($1.602 \times 10^{-19} \text{ C}$)
m_e	mass of electron ($9.109 \times 10^{-31} \text{ kg}$)
α	surface tension of liquid ^4He ($3.76 \times 10^{-4} \text{ kg/s}^2$ at 0.6 K) ($3.72 \times 10^{-4} \text{ kg/s}^2$ at 0.88 K) ($3.69 \times 10^{-4} \text{ kg/s}^2$ at 1.1 K)
ρ	volume density of liquid ^4He (145.1 kg/m^3 about 1 K)

Contents

Declaration of Original and Sole Authorship	iii
Abstract	v
Acknowledgment	vii
Abbreviations	ix
Nomenclature	xi
Contents	xiii
List of Figures	xv
List of Tables	xvii
Introduction	1
1 Electrical transport in highly correlated electron systems	3
1.1 Bound states of electrons on liquid helium surface	5
1.2 Overview of transport theories	8
1.3 Scatterers: vapor atoms and ripplons	10
1.4 Electron-electron interaction	13
1.5 Nonlinear transport of electron crystal	16
1.6 Summary	20
2 Experimental methods	21
2.1 Device structure and manufacturing process	21
2.2 Experimental setup	24
2.3 Measurements and analysis	27
3 Inhomogeneous WS and multiple BC plateaus	33
3.1 Experiment	33
3.2 Results and Discussion	35
3.3 Summary	37

4	Effect of finite size of WS on its nonlinear transport	41
4.1	Theoretical framework	41
4.2	Experiment	42
4.3	Results	44
4.4	Discussion	49
4.5	Summary	52
5	WS in microchannel subject to spatial periodic potential	53
5.1	Frenkel-Kontorova model	53
5.2	Experiment	55
5.3	Results	56
5.3.1	Phase diagram of electron system without applying periodic potential	56
5.3.2	Effect of periodic potential	57
5.4	Discussion	61
5.5	Summary	62
6	Electron flow in T-channel geometry	63
6.1	Experiment	63
6.2	Results	63
6.3	Discussion	67
6.4	Summary	68
	Conclusion	69
	Bibliography	71

List of Figures

1.1	$\mu_{4\text{He}}^{-1}(n_e)$ vs T	4
1.2	$\mu_{4\text{He}}^{-1}$ vs T at $n_e = 3.2 \times 10^8 \text{ cm}^{-2}$	5
1.3	SSE above bulk liquid helium	6
1.4	Probability density of bound SSE eigenstates	7
1.5	Fractional population of the ground state	8
1.6	$\mu_{4\text{He}}, \mu_{3\text{He}}$ vs T	11
1.7	$\tau(E_{\perp})$ vs T	12
1.8	SE on an uneven interface	13
1.9	Topological defects in a hexagonal 2D lattice	15
1.10	Cherenkov radiation	17
1.11	BC scattering of WS	18
1.12	BC scattering: dimple lattice and nonlinear mobility	18
1.13	Force balance for an electron in dimple	19
2.1	FET vs. microchannel device	22
2.2	Microchannel device	23
2.3	Microchannel device in a copper cell	24
2.4	Liquid helium film in the channel	25
2.5	Parallel-plate capacitor model	26
2.6	n_e estimation	27
2.7	Lump circuit model	28
2.8	Locus for lump circuit	29
2.9	Time-resolved transport measurement for SSEs in BC scattering regime	31
2.10	Current I_{out} measured by a lock-in amplifier for WS in nonlinear transport regime	31
3.1	Inhomogeneous-WS microchannel device	34
3.2	I_{out} vs V_{pp}	36
3.3	$dI_{\text{out}}/dV_{\text{in}}$ vs V_{in} and V_{G}	38
4.1	Resistance oscillations under ac conditions	43
4.2	Finite-size effect microchannel device	44
4.3	Data sets S1D1-S1D3 measured in Sample 1	45
4.4	Data sets S1D4-S1D6 measured in Sample 1	46
4.5	Data sets S2D1-S2D3 measured in Sample 2	47
4.6	Data sets S1D4, S1D5 measured in Sample 2	48

4.7	$E_s^{(\max)}$ vs L_{WS}	50
5.1	FK model	53
5.2	Periodic potential device	55
5.3	I vs $V_{\text{sg}}, V_{\text{ch}}$	56
5.4	I vs $V_{\text{in}}, \Delta V_{\text{F}}$	58
5.5	GS of odd/even number of particles in one period	59
5.6	I vs $V_{\text{sg}}, \Delta V_{\text{F}}$	60
6.1	T-shaped microchannel device	64
6.2	Flow of SSEs in T-channel at $T = 0.4$ K	65
6.3	Temperature dependence of current difference $I_{\text{R}} - I_{\text{T}}$	66

List of Tables

1.1	KTHNY predictions for a 2D isotropic system.	14
-----	--	----

Introduction

Understanding transport properties of strongly correlated electron systems is one of the important fundamental problems of modern condensed-matter physics. Superconductivity is one famous example of a non-trivial transport property arising from the electron-electron interaction. The transport of electrons in such systems is a complicated affair that involves different processes, such as stochastic scattering processes with background scatterers, interaction of electrons with each other and with an external driving field, etc. In general, all these processes are interconnected with each other.

The classical equation for transport of particles that involves the stochastic scattering processes in a dilute gas system is the Boltzmann transport equation (BTE):

$$\frac{df}{dt} = \left(\frac{\partial f}{\partial t} \right)_{\text{collision}}, \quad (1)$$

where $f = f(\vec{r}, \vec{p}, t)$ is the distribution function of particle in the phase space. It essentially describes the balance of forces due to, on the one hand, an external drive and, on the other hand, collisions with background scatterer. In a quantum mechanical treatment, the description of scattering is more intricate and involves quantum correlation functions, but the mechanism of force balance is universal. An average physical quantity of interest is described by the trace of a corresponding quantum mechanical operator over the statistical operator $\hat{\rho}$, the density matrix operator, that must satisfy the quantum Liouville equation:

$$i\hbar \frac{\partial \hat{\rho}}{\partial t} = - [\hat{\rho}, \hat{H}], \quad (2)$$

where \hat{H} is the Hamiltonian of the system studied. Similarly to the classical kinetic theory, the quantum transport theory (QTT) derives system's transport properties from the quantum Liouville equation using various approximations, such as the *linear response approximation*, etc. The main task in both classical and quantum transport theories is to deal with the scattering term, and the situation becomes significantly more complicated when the interactions between particles comprising the system can not be ignored. Unlike in the dilute weakly interacting systems which can be well described theoretically by the properties of the individual particles, qualitatively new behavior of a strongly correlated system, such as the superconductivity mentioned earlier, usually can not be predicted from a single-particle description. Strong inter-particle interaction results in a collective behavior, therefore new global and macroscopic properties may

appear. As often happened in the history of science, experimental observations of such new properties happen earlier than their theoretical development.

On the theoretical side, quantum Monte Carlo methods and density functional theory provide certain understanding of strongly correlated system. Nevertheless, such studies are significantly impeded by complexity of the problem and insufficiency of computation resources. As an alternative pathway, some theoretical models can be studied experimentally using a well controlled physical system [?]. For example, some unsolved standard theoretical models of strongly interacting systems, such as the Hubbard and Frenkel-Kontorova models, has been recently studied using ultracold atoms and ions [3? ? -5]. Such experiments allowed not only to probe correlation effects between atoms and ions but also study effects of their interaction with external (substrate) potentials which can have great implications, for example, for the general study of friction [6].

Surface State Electrons (SSEs) floating above a free surface of liquid helium is a very promising candidate system for such studies. Unlike in other two-dimensional electron systems, the nature of background scatters is very well understood and theoretically described [7, 8]. Owing to a weak interaction with polar liquid, SSEs essentially reside in vacuum at a relatively large distance of 10 nm above the liquid and interact with each other by the *unscreened* Coulomb repulsion. In general, the potential energy of electron-electron interaction is much larger than electron kinetic energy and the system crystallizes into the solid phase already at temperatures about 1 K. Unique nature of the substrate, a quantum liquid which does not solidify down to the temperature of absolute zero, allows to study regime of strong coupling of SSEs to surface deformations. This brings additional intriguing properties to the strongly-corrected system of SSEs on liquid helium.

This thesis is mainly about the experimental study of the transport properties of strongly-correlated SSE system, especially focusing on its solid phase. Experimentally, we study SSEs in microchannel devices which are built using microfabrication methods, and measure electrical transport of SSEs subject to various device geometries and configurations of applied electrostatic potentials depending on the particular topic of research. In Chapter 1, we will briefly describe general properties of SSEs and outline main theoretical frameworks used to describe electrical transport in this system. The microfabricated devices and experimental methods will be briefly described in Chapter 2. Different experiments with SSEs in such devices will be described in the following four chapters (Chapters 3-6). This thesis will end with our prospective for future studies.

Chapter 1

Electrical transport in highly correlated electron systems

After the theoretical proposals of SSE system on liquid helium were introduced in 1969 [9, 10], many experiments with this system have been reported. It can be expected that SSE could serve as an ideal system for testing approaches in QTT because the properties of SSE scatterers are well known. It was found that for a dilute SSE system, the predictions of QTT are comparable with the experimental results. However, when approaching the strongly correlated regime at high electron densities, discrepancies between theoretical predictions and experimental observations become prominent. For example, in 1984 R. Metrota et al. have reported a systematic measurements of SSE mobility at different temperatures for various SSE densities n_e [11]. As shown in Fig. 1.1, for the liquid phase of SSEs the deviation of single-electron theory from experimental data increases with increasing n_e . For example, at $n_e = 0.53 \times 10^8 \text{ cm}^{-2}$ the experimental data are well described by the theoretical curve, see Fig. 1.1 (a). However, at $n_e = 3.2 \times 10^8 \text{ cm}^{-2}$ the discrepancy between experimental data and theoretical curve is significant, see Fig. 1.1 (d).

Clearly, the *single-electron approximation* fails under the condition of high n_e and low temperatures. Unfortunately, the up-to-date theoretical models which attempt to include the inter-electron interaction are still unable to account for the discrepancy. Inclusion of electron-electron interaction into the transport theory has been discussed by Monarkha and Kono in Chapter 3.3 of the book *Two-dimensional Coulomb liquids and solids* [7]. Predictions of many-electron theory are shown in Fig. 1.2. The theoretical prediction (solid curve) for highly correlated electrons can only partly explain the observed increase in the resistance of SSE. The discrepancy between theory and experiment is still an open question.

At lower temperatures a sudden jump in the resistance seen in Figs. 1.1 and 1.2 indicates that the SSEs crystalize into a solid phase, i.e. the Wigner solid (WS). The transport of WS is nonlinear and rather complicated due to resonant coupling between WS and capillary waves on helium surface. This mechanism of resonant coupling between WS and ripplon is related to coherent emission of ripplons by moving electron lattice; the corresponding transport regime is called the Bragg-Cherenkov (BC) scattering [?]. This regime is rich of interesting physical phenomena discussed later in this thesis.

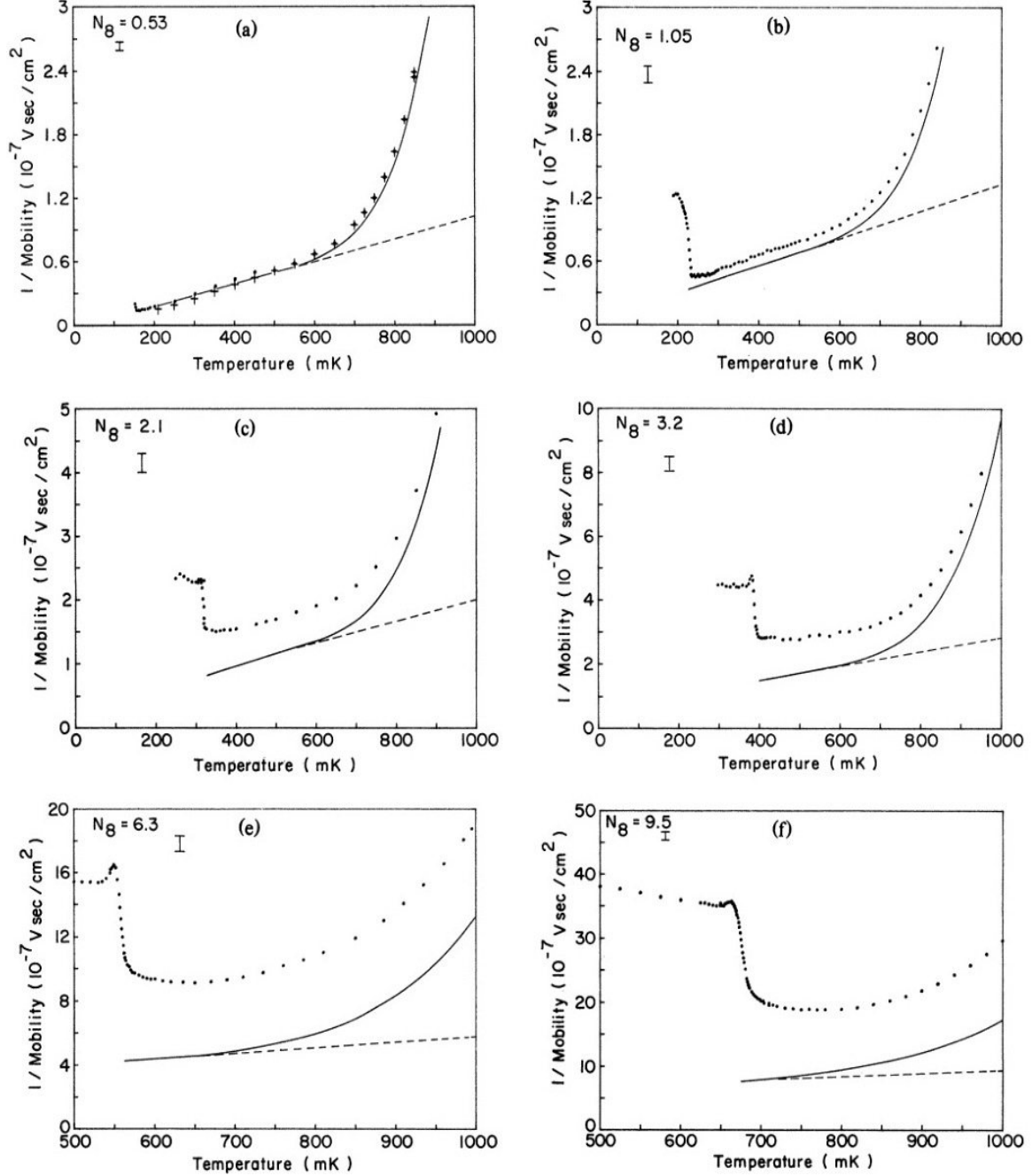


Figure 1.1: Inverse mobility vs temperature for various densities. The electron densities denoted by N_8 is in units of 10^8 cm^{-2} . The solid dots and cross symbols are the experimental data. The curves are the theoretical predictions of the single-electron approximation (dashed: consider ripplon scattering only; solid: ripplon and helium gas atoms). Figures are reproduced from [11].

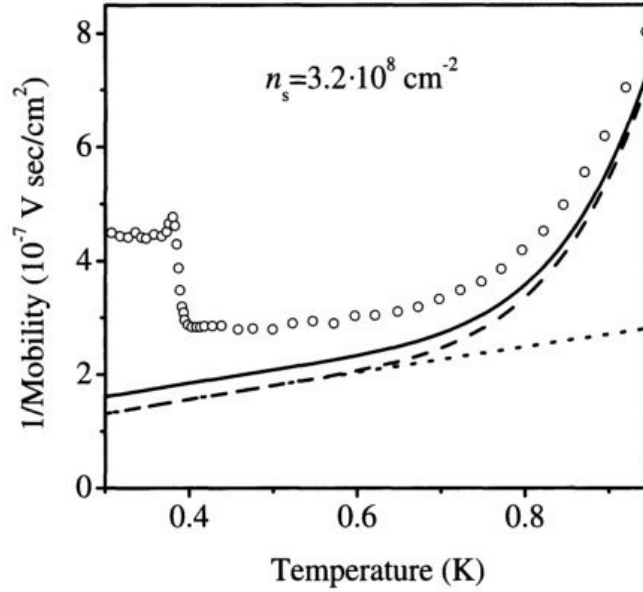


Figure 1.2: Inverse mobility vs temperature for SSEs with electron density $n_e = 3.2 \times 10^8 \text{ cm}^{-2}$. The experimental data (open circle) are taken from Fig. 1.1 (d). The dashed curve is the theoretical result of the single-electron approximation for ripplon and helium gas atom scattering, the dotted curve is for ripplon scattering only. The solid curve is the prediction of many-electron theory. Figure is reproduced from [7].

This chapter will start with the description of the structure of quantized states of SSE. Then, the general theoretical frameworks used to describe electrical transport in strongly-correlated electron systems will be briefly reviewed in Sect. 1.2. The single-electron interaction with two kinds of background scatterers in our system, the vapor atoms and ripples, will be discussed in Sect. 1.3. The consequences of the strong electron-electron interaction in SSEs are discussed in Sect. 1.4. The final section Sect. 1.5 will be focused on the Bragg-Cherenkov scattering, which is the main theme of the experimental studies described in this thesis.

1.1 Bound states of electrons on liquid helium surface

SSEs residing above the surface of liquid helium form a stable physical system. To illustrate the basic structure of SSEs, we consider the following simplified model of a particle of charge $-e$ ($e > 0$) in vacuum (relative permittivity $\epsilon = 1$) at a distance z away from the plane interface of liquid helium (with relative permittivity ϵ_{He}). Helium is an inert atom that heads the noble gas group in the periodic table. Its 1s orbitals are fully occupied. Owing to the Pauli exclusion principle, an additional electron in the vicinity of He atom must have its wavefunction to be orthogonal to occupied atomic states, which leads to the strong repulsion between electron and He atoms. Therefore, a strong repulsive force will prohibit electrons from entering liquid helium. The resulting potential barrier at the liquid helium surface V_0 is about 1 eV [12, 13]. In addition

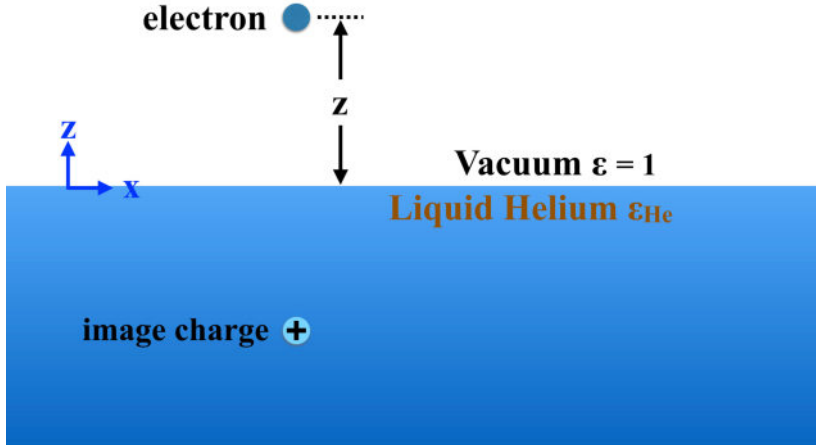


Figure 1.3: Simplified classical model for a single electron along liquid helium. A particle of charge $-e$ representing electron floats above the free surface of liquid helium at a distance z . The image charge $+e\Lambda$ locates below the electron at the same distance z inside the liquid helium.

to a strong short-range repulsion, there is a long-range attraction between electrons and bulk liquid. Whenever an electrical charge locates near a dielectric, instantaneous dipole moments of the polar atoms comprising the dielectric medium are induced. The electric field produced by induced dipoles exerts an attractive force on the electron. The repulsive barrier and attractive potential are entirely responsible for the bound surface states of electrons above liquid helium.

For a flat unconfined liquid helium surface, the method of electrical images is used to yield an effective image charge $q' = +e\frac{(\epsilon_{\text{He}}-1)}{(\epsilon_{\text{He}}+1)}$ located inside the liquid at the same distance z from the liquid surface. Thus, the potential energy of electron at distance z can be approximated as

$$U_e(z) = V_0\theta(-z) - \frac{k_e\Lambda}{z+z_0}e^2\theta(z) + eE_{\perp}z, \quad (1.1)$$

where $\Lambda = \frac{(\epsilon_{\text{He}}-1)}{4(\epsilon_{\text{He}}+1)}$ is a dimensionless constant much less than 1, $\theta(z)$ is the unit step (Heaviside) function, and E_{\perp} is the magnitude of an external electrical field applied normal to the surface. The parameter $z_0 \simeq 1 \text{ \AA}$ is introduced in order to avoid the singularity of the image potential at the liquid helium surface [14]. Because V_0 is much larger than the typical eigen-energies of electron in the potential Eq. (1.1), the simplified model with $V_0 \rightarrow \infty$ and $z_0 \rightarrow 0$ is usually used. When $E_{\perp} = 0$, the corresponding 1D Schrödinger equation is identical to that of the radial motion of electron in the hydrogen atom. The quantized energy levels along z axis for SSEs thus can be written as

$$\varepsilon_n^{(\perp)} = -\frac{\Lambda^2 R_e}{n^2} \simeq -\frac{0.65}{n^2} \text{ meV} \simeq -\frac{7.5}{n^2} \text{ K}, \quad n = 1, 2, 3, \dots, \quad (1.2)$$

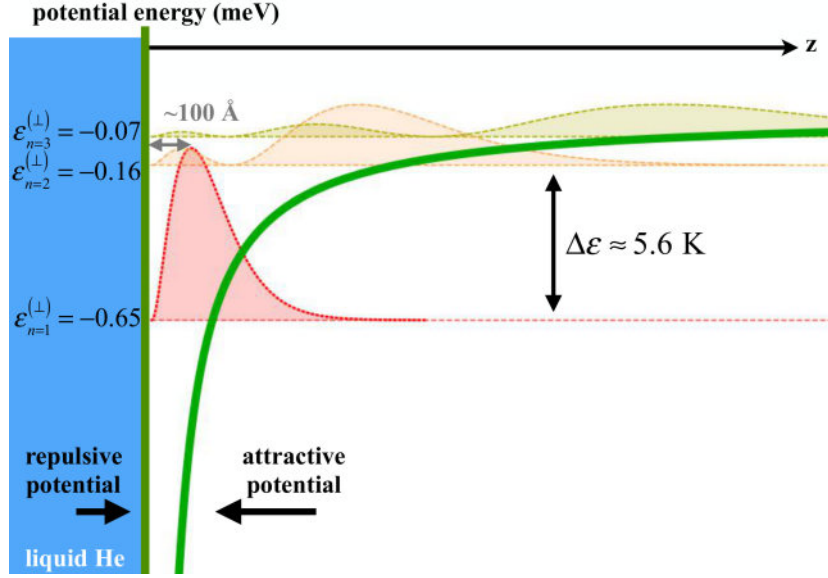


Figure 1.4: Probability density of SSE eigenstates. Schematic diagram of the potential energy of interaction and the first three eigenstates of a single SSE above liquid helium surface.

where R_e is the effective Rydberg constant for SSE. The corresponding wave-functions are

$$\Psi_n(z) = R_{10}(z), \quad n = 1, 2, 3, \dots, \quad (1.3)$$

where $R_{10}(r)$ is the well-known expression for the radial wavefunction of electron in the hydrogen atom. The probability density of the first three eigenstates and the image potential are plotted in Fig. 1.4.

Eq. (1.2) is obtained under the condition $E_{\perp} = 0$. In most cases of the experiments with SSE system, an external electric field E_{\perp} is applied normal to the liquid helium surface. For weak E_{\perp} the correction to eigen-energy can be considered in the first order perturbation theory, which results in the linear Stark shift:

$$\delta\varepsilon_n^{(\perp)} \simeq eE_{\perp} \langle n | z | n \rangle. \quad (1.4)$$

For sufficiently strong E_{\perp} , that is such that the image potential can be disregarded, Eq. (1.1) results in a triangular-shaped potential well. Therefore,

$$\varepsilon_n^{(\perp)} = eE_{\perp} \frac{\zeta_l}{\gamma_F}, \quad (1.5)$$

where $\gamma_F = \left(\frac{2m_e e E_{\perp}}{\hbar^2}\right)^{1/3}$ and ζ_l is the l -th zero of the Airy function, $\text{Ai}(-\zeta_l) = 0$ [15]. The corresponding wave-functions are

$$\Psi_n(z) = \text{constant} \times \text{Ai} \left[\left(z - \frac{\varepsilon_n^{(\perp)}}{eE_{\perp}} \right) \gamma_F \right]. \quad (1.6)$$

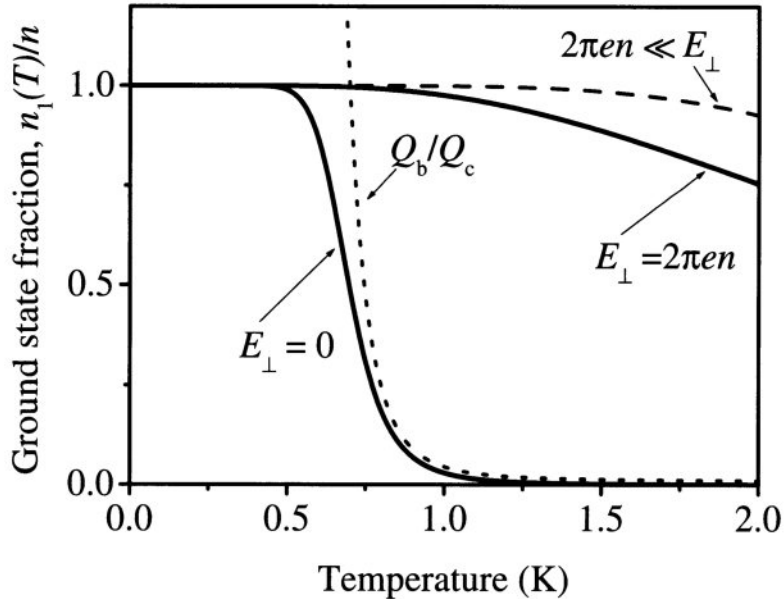


Figure 1.5: Fractional population of the ground state. Fractional population of the ground state plotted against temperature for different relations between holding electric field E_{\perp} and electron density. The dotted curve is the ratio of Q_b/Q_c , where Q_b and Q_c are the partition functions of the bound states $Q_b = \sum_{l=1}^{\infty} e^{-\varepsilon_l^{(\perp)}/T}$ and the continuous spectrum states (determined by the container length L_z) $Q_c = \sqrt{\frac{m_e T}{8\pi\hbar^2}} L_z$, respectively. The ground state population is calculated according to $\frac{n_1}{n} = \frac{\exp(-\varepsilon_1^{(\perp)}/T)}{\sum_l \exp(-\varepsilon_l^{(\perp)}/T)}$, where n is the electron density. The dashed curve is evaluated for $E_{\perp} = 9$ V/cm. Figure is reproduced from [7].

In the presence of E_{\perp} , the binding energy of a ground state electron and the energy difference between different eigenstates substantially increases. Accordingly, the fractional population of the ground state increases with E_{\perp} . As shown in Fig. 1.5, the fractional population of the ground state is almost 100% even for rather small pressing fields E_{\perp} . Correspondingly, for typical temperatures and pressing fields used in the experiments, SSEs are mostly in the ground state. Therefore, we can safely ignore occupancy of the higher eigenstate and focus on the transport of electrons confined in a 2D plane.

1.2 Overview of transport theories

In transport experiments we are interested with an effect of driving force on the motion of the whole electron system. In a semiclassical theory, the relation between the electron drift velocity v_d and the external driving field \vec{E}_{ex} is obtained from the BTE using the *relaxation time approximation*. As outlined in the Introduction, BTE accounts for stochastic scattering processes occurring in the system due to interaction with background scatterers. Although the stochastic scattering events are random, a moving

electron will receive more impacts from the collisions in the direction opposite to its motion. The number of such impacts is proportional to the velocity of the moving electron. The impacts due to background scatterers, therefore, give rise to the frictional force on an electron subjected to a driving force. The frictional force and the random background collisions must be related. The internal relationship of these microscopic forces is manifested in the so-called *fluctuation-dissipation theorem*. Without external driving force, the equation of motion including the thermal noise is

$$m\dot{v} = -m\gamma v + \eta, \quad (1.7)$$

where γ is a coefficient appearing in the frictional force in the units of T^{-1} and η is the fluctuating force (noise) due to collisions with background scatterers. The solution to Eq. (1.7) is

$$v(t) = v_0 e^{-\gamma t} + \frac{1}{m} \int_0^t dt' \eta(t') e^{-\gamma(t-t')}, \quad (1.8)$$

where $v_0 = v(0)$. The physical meaning of the introduced coefficient γ is clear. It represents the inverse of the time scale during which an electron relaxes to attain equilibrium with the background thermal bath (the relaxation time approximation). For a large thermal bath we typically assume that the background noise η is *white*, that is the corresponding correlation function can be represented as $\langle \eta(t') \eta(t'') \rangle = \Gamma \delta(t' - t'')$, where Γ is a measure of strength of thermal fluctuations. Then, by equating, on the one hand, the statistical average $\langle v^2 \rangle$ obtained using Eq. (1.8) and, on the other hand, its thermal equilibrium average, a useful relationship between fluctuating and thermal equilibrium quantities can be obtained. For example, for a classical system we obtain the relation $\Gamma = 2m\gamma k_B T$. In other words, the frictional dissipation rate γ , that is the inverse of the relaxation time, is related to measure of the strength of fluctuations in the background scatterers Γ . This relation represents the famous fluctuation-dissipation theorem.

Now let's consider a system under an applied external electric field. The full derivative in the BTE, see Eq. (1) in the Introduction, can be expressed as

$$\frac{df}{dt} = \frac{\partial f}{\partial t} + \frac{\vec{p}}{m} \cdot \vec{\nabla}_r f + \vec{F}_{\text{ex}} \cdot \vec{\nabla}_p f. \quad (1.9)$$

Assuming that the system has a uniform density ($\vec{\nabla}_r f = 0$) and has attained an equilibrium ($\frac{\partial f}{\partial t} = 0$), we have

$$\frac{df}{dt} = \vec{F}_{\text{ex}} \cdot \vec{\nabla}_p f = e \vec{E}_{\text{ex}} \cdot \vec{\nabla}_p f, \quad (1.10)$$

where $\vec{F}_{\text{ex}} = e \vec{E}_{\text{ex}}$. Under the relaxation time approximation, RHS of BTE can be expressed as

$$\left(\frac{\partial f}{\partial t} \right)_c = f_{\text{eq}} \gamma - f \gamma = -\frac{f - f_{\text{eq}}}{\tau}, \quad (1.11)$$

where $\gamma = 1/\tau$, $f_{\text{eq}}\gamma$ and $f\gamma$ represent the rates of scattering in and out of the given volume of the phase space, respectively. Therefore,

$$f = f_{\text{eq}} - e\tau \vec{E}_{\text{ex}} \cdot \vec{\nabla}_p f = f_{\text{eq}} - e\tau \sum_b E_b \frac{\partial f}{\partial p_b}. \quad (1.12)$$

The electric current density is

$$J_a = \frac{e}{V} \int d^3\vec{r} \int \frac{d^3\vec{p}}{(2\pi\hbar)^3} f v_a \equiv \sum_{b=1}^3 \sigma_{ab} E_b, \quad (1.13)$$

where σ_{ab} is the conductivity tensor. For a quantum Fermi gas, $f_{\text{eq}} = \frac{1}{e^{(\varepsilon - \varepsilon_F)/k_B T} + 1}$, $\sigma_{ab} = \delta_{ab} \frac{n e^2 \tau}{M} = \sigma_{aa}$. Eq. (1.13) represents the Ohm's law, where σ_{ab} is the Drude conductivity¹. The condition of force balance between the driving field and the stochastic scattering events automatically results in a terminal (drift) velocity, v_d , of the electron system.

The general framework to describe the single SSE transport is similar to the classical Drude-Lorentz model [7, 16–18] outlined above. In a quantum treatment, the electron conductivity can be derived using the memory function expressed in terms of the electron density-density correlation function and its time and space Fourier transform, the equilibrium *dynamical structure factor* (DSF) [7?]. The conductivity of SSEs can be written using the effective collision rate γ_{eff} , which is determined by the ripplon scattering at low temperatures and vapor-atom scattering at high temperatures and in general depends on the electron density n_e , in the form of $\sigma = e^2 n_e / m_e \gamma_{\text{eff}}$. When n_e is sufficiently large, many-body effects become important, in particular the multiple scattering events involving at least two background scatterers. The relaxation time approximation may be no longer applicable. When the scattering time becomes shorter than the momentum relaxation time, the initial state of the system at each collision event do not correspond to the equilibrium state of the background. The retardation effects become important, and spectrum of fluctuating force exerted on electrons deviate from the white noise. This results in the correlations between particle motion and complicates the mathematical description of the scattering processes. For strongly correlated electron systems, the electron-electron interaction makes the equilibrium DSF hard to describe [19, 20]. For SSEs, in some cases it is still possible to incorporate effects of strong electron-electron interaction into the expression for equilibrium DSF using concept of the fluctuating many-electron field [7]. Nevertheless, in many cases the theoretical predictions of the many-body QTT are unable to explain experimental observations in SSEs, c.f. our earlier discussion and Fig. 1.2. Up to now, a complete theoretical tool for describing the electrical transport of electrons on helium is still missing.

1.3 Scatterers: vapor atoms and riplons

There are two kinds of background scatterer in the system of SSEs floating above the free surface of liquid helium. One is the vapor atoms of helium, and the other is the

¹The Hall conductivity σ_{ab} also can be derived from the conductivity tensor.

capillary waves of the liquid surface, or riplons in its quantized form. The number of both kinds of background scatterers decreases with cooling. The scattering rate by vapor helium atoms has been found to be independent of the SSE energy of the motion parallel to the liquid surfaces, and depends linearly on the density of vapor helium atoms $n^{(a)}$ [7, 18, 21]

$$n^{(a)}(T) = \left(\frac{M_a T}{2\pi\hbar} \right)^{3/2} \exp\left(-\frac{Q}{T}\right), \quad (1.14)$$

where Q is the evaporation constant and M_a is the mass of the helium atom. Therefore, while $n^{(a)}$ increases exponentially as the temperature rises, the electron mobility μ decreases exponentially with temperature

$$\mu = \frac{8ea_0}{3\pi\hbar A n^{(a)}} \propto T^{-3/2} \exp\left(\frac{Q}{T}\right), \quad (1.15)$$

where a_0 is the effective Bohr radius of SSE and A is the scattering cross section of a He atom [18].

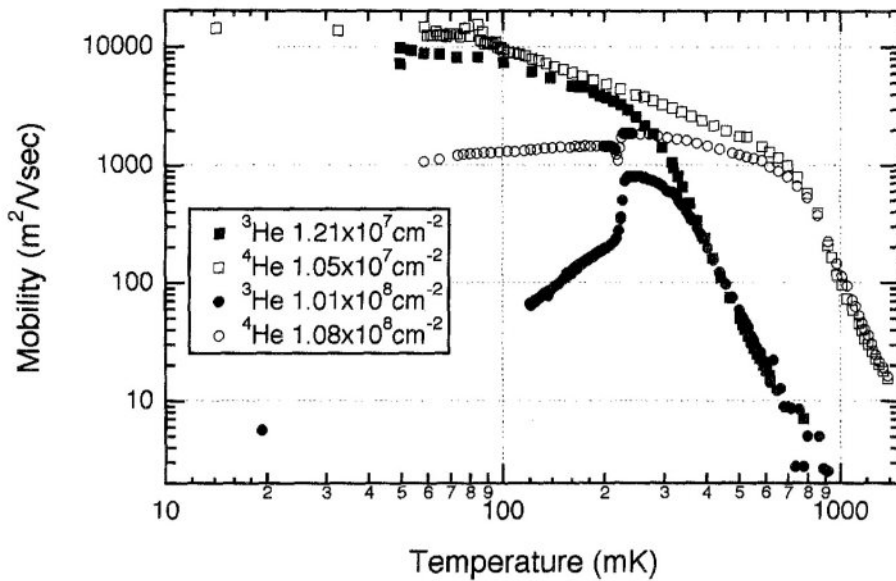


Figure 1.6: Comparison of $\mu_{4\text{He}}$ and $\mu_{3\text{He}}$ as a function of temperature. Temperature dependence of $\mu_{3\text{He}}$ is qualitatively same as the $\mu_{4\text{He}}$ data. The vapor-atom regime is shifted to lower temperatures for the ^3He surface than that for the ^4He case due to the higher vapor pressure of ^3He . In the case of ^4He , the gradual increase of $\mu_{4\text{He}}$ below 700 mK is due to the crossover from atom- to ripplon-dominated scattering regime. Figure is reproduced from [22].

At low temperatures $T < 0.7$ K, the vapor density is extremely low. Therefore, the SSE scattering is dominated by riplons. The number of riplons is described by the Bose distribution function, and only the low energy ones are involved in the momentum relaxation of SSEs, $q \leq 2k$, where q is the wave number of riplons and k is the wave number of SSEs corresponding to their thermal motion along the liquid

surface. For ripples with such q their energy $\hbar\omega_q \ll k_B T$, which is the consequence of the ripplon dispersion relations $\omega_q = \sqrt{\alpha/\rho} q^{3/2}$. The corresponding density of such ripples, therefore, decreases linearly with decreasing temperature [7, 14]:

$$n_q^{(r)}(T) = \frac{1}{e^{\frac{\hbar\omega_q}{k_B T}} - 1} \simeq \frac{k_B T}{\hbar\omega_q}. \quad (1.16)$$

As a result, electron-ripple scattering rate decreases linearly with T . For liquid ${}^3\text{He}$ which has higher vapor pressure than ${}^4\text{He}$ at the same T , the electron-vapor scattering extends to a lower temperature region, as shown in Fig. 1.6 [22]. At sufficiently low T , the mobility drops abruptly. This is caused by the Bragg-Cherenkov scattering when the SSEs are in solid phase. This will be discussed in the Sect. 1.5.

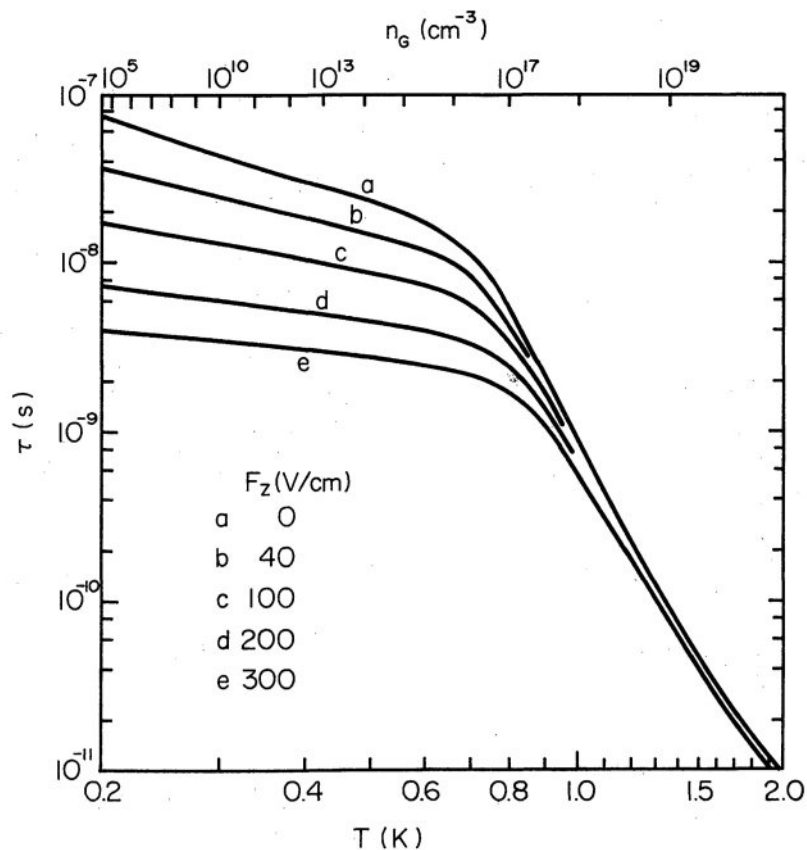


Figure 1.7: Momentum relaxation time τ as a function of temperature for various values of pressing field F_z . Below $T \approx 0.7$ K, the ripplon scattering becomes dominant and shows significant F_z dependence. Note that Ohmic mobility $\mu = e\tau/m_e$. Figure is reproduced from [18].

The electron-ripple interaction is described by the displacement function $\xi(r)$ of the liquid surface entering into the polarization interaction potential of an electron with helium. It is strongly affected by the SSE probability distribution near the interface. As discussed in Sect. 1.1 the SSE wavefunction $\Psi_n(z)$ is strongly affected by the pressing field E_\perp , therefore the electron-ripple scattering is expected to depend on E_\perp . Intuitively, at high E_\perp the coupling of electrons and ripples increases, so SSE

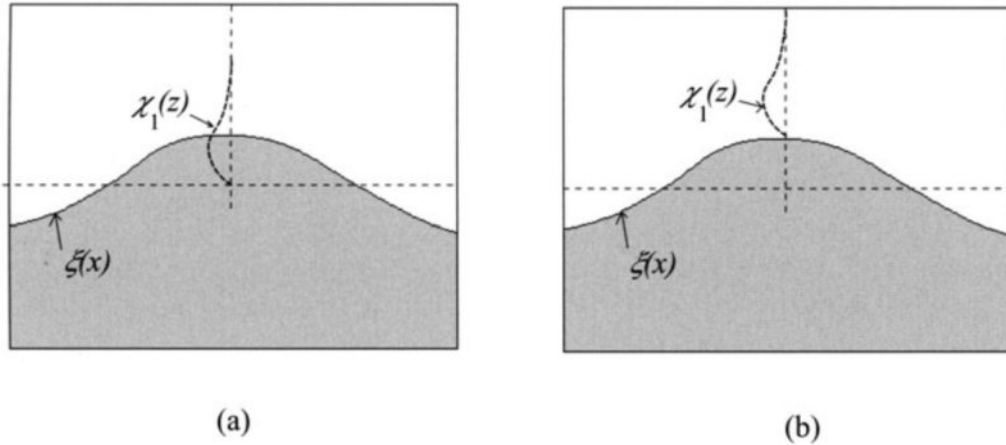


Figure 1.8: A single SSE on an uneven surface. The diagram shows the wave function of an electron which do not follow the interface displacement (a) and for an electron that remains in the bound state (b). Figure is reproduced from [7].

mobility decreases [18, 23]. The momentum relaxation time of SSE for various values of pressing field E_{\perp} is shown in Fig. 1.7 [18]. The coupling term in electron-rippon interaction which is linearly proportional to E_{\perp} mainly results from the fact that an electron wave function in the bound surface state should be zero at the helium vapor-surface interface, see Fig. 1.8 [7]. Therefore, when an electron encounters ripples it should follow the surface displacement which results in the interaction potential energy $U_{\text{int}} \approx eE_{\perp}\xi$, where ξ is the surface displacement.

1.4 Electron-electron interaction

There is no intrinsic difference between scattering of an electron from another electron and that from other sources of scatterers, like vapor atoms and ripples. Electron-electron collisions preserve total momentum of particles like other collisions do. But when describing the dynamics of the system of electrons under the influence of the environment, electron-electron scattering within the electron system does not contribute to the momentum balance between the external forces applied to the electron system and the friction forces from their background scatterers. In other words, the exchange of momentum between electrons does not change the total momentum of the electron system, therefore, it doesn't affect the long-wavelength conductivity directly [?]. The electron-electron interaction mainly affects the electron distribution function f (in the classical kinetic equation treatment) or the density matrix ρ (in the quantum treatment) [7, 24]. In the case when the corresponding momentum and energy redistribution within the electron system is mainly governed by the inter-electron interaction, the regime of electron transport is called the complete control regime. In another case when only the energy redistribution is governed by the electron-electron collisions, it is called the partial control regime. The redistribution of $f(\vec{r}, \vec{p}, t)$ is strongly related to the relation between electron-electron collision rate ν_{e-e} and momentum/energy relaxation rate γ , and thus influences the transport properties significantly. The study

Table 1.1: KTHNY predictions for a 2D isotropic system.

	Solid	Hexatic	Liquid
Dislocations	bound in pairs	free	free
Disclinations		bound in pairs	free
Positional correlations	quasi-long range	short range	short range
Elastic constant	$\neq 0$	0	0
Bond-orientational correlations	long range	quasi-long range	short range

The difference between the three phases predicted by KTHNY theory. There are difference on two levels: (1) the presence of different types of topological defects, and (2) the type and range of correlations [8].

of strongly correlated electron systems is largely about the competition between individualistic and collective behavior of electrons.

Correlations between electron motion due to mutual interaction between particles have large impact on statistical properties of SSEs. Owing to the property of self-organization, this is largely manifested in the emergence of some kind of ordered structures, such as the spatially ordered Wigner crystal [25]. Wigner crystal is the solid phase of the electrons in a structureless positive background. When the potential energy of interaction between electrons U_{ee} becomes significantly larger than the kinetic energy K_e , the electrons eventually localize at the lattice sites in order to reduce their total energy. The ratio of the mean interaction energy to the mean kinetic energy is called the plasma parameter, $\Gamma \equiv \langle U_{ee} \rangle / \langle K_e \rangle$. For the system of SSEs floating above liquid helium, $\Gamma = e^2 \sqrt{\pi n_e} / k_B T$. The transition for SSEs into the solid phase is expected to occur at $\Gamma \geq 130$. The spatial structure of WS in SSEs on liquid helium is a 2D hexagonal lattice [8]. According to the KTHNY (Kosterlitz-Thouless-Halperin-Nelson) theory, melting of WS occurs in two stages through two continuous phase transitions: solid phase to hexatic phase, and hexatic phase to liquid phase. The phase transition is mediated via the unbinding of pairs of topological defects: disclinations and dislocations, as shown in Fig. 1.9. A disclination is an orientational defect that can be viewed as a particle having the wrong number of nearest neighbors, the so-called coordination number. A dislocation is a bound pair of disclinations of +1 and -1 coordination numbers. It maintains the long distance ordering with a much lower energy than an isolated disclination. The unbinding of dislocations will cause the system to lose its long-distance order and its resistance to shear stress. The response to shear stress is a key property to distinguish between solid and liquid phases. The melting of WS is generally mediated via the spontaneous unbinding of dislocations due to thermodynamic instability. In KTHNY theory, WS is elastic and characterized by the shear modulus G . The temperature dependence of the shear modulus can be expressed as $G(T) = G - (1 - A \cdot T/T_c)$, where T_c is the temperature of the first melting transition from the solid phase to the hexatic phase, and A is a constant which can be determined from the experiments [8].

There are two phonon modes of WS excitation spectrum. In long-wavelength limit, the longitudinal phonon mode coincides with the 2D plasmon spectrum, while the transverse mode follows the usual sound-like dispersion relation [7]. In WS, the phonon

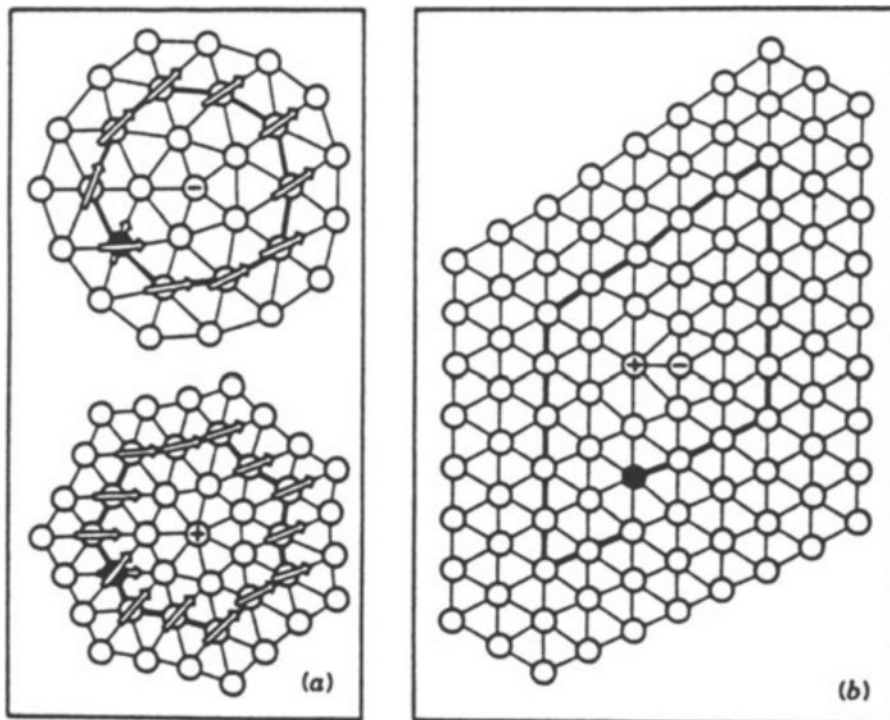


Figure 1.9: Topological defects in a triangular lattice. (a) Isolated disclinations. For a hexagonal lattice (coordination number is 6) there are disclinations with coordination 5 and 7. They are indicated by (-) and (+) respectively and can be viewed as topological charges. Note that a disclination is characterized by a mismatch in orientation and the energy of such a defect is large. (b) Isolated dislocation. A dislocation is a tightly bound pair of +1 and -1 disclinations. The ordering at long distance will not be disrupted by a dislocation. And consequently such a bound pair has a much lower energy. Figure is reproduced from [8].

modes and the motion of dislocations strongly interact with riplons (one of the background scatterers). The interaction of WS with a soft liquid substrate can result in a complicated dynamics associated with polaronic states when an electron becomes self-trapped into a surface dimple that it creates [26]. The coupled WS-dimple system can show striking behaviour, such as the nonlinear conductivity of WS in the Bragg-Cherenkov scattering regime and decoupling (sliding) transition [27?].

1.5 Nonlinear transport of electron crystal

Cherenkov radiation (Nobel Prize in 1958) occurs when a charged particle moves in a medium at a speed faster than or equal to the phase velocity of the electromagnetic radiation it triggers in the medium [28, 29]. Although exact theory for this effect involves a full quantum mechanical treatment, main features of Cherenkov radiation are classical or semiclassical in origin. A moving charged particle polarizes the polar atoms of the medium. The coherent response of the medium as a whole is described by the distribution of electrical dipoles induced by the charged particle along its trajectory. When the charged particle velocity v_p is faster than the local phase velocity of light in the medium, the induced dipole distribution is asymmetric and has a non-zero total dipole moment which radiates EM waves. Cherenkov radiation, accordingly, has a threshold velocity for the moving particle $v_p^{(\text{th})} = c/\sqrt{\epsilon}$, where c is the speed of light in vacuum, and ϵ is the relative permittivity of medium. The propagation direction of the collective wavefront tangent to all circular wavefronts of the radiated EM waves is at an angle θ_c to the direction of the moving charged particle. This characteristic angle θ_c can be interpreted qualitatively in terms of "shock waves" like the supersonic bomb or the bow shock from the moving object on liquid surface, see Fig. 1.10 [30]. The angle θ_c is approximately defined by the travel distance of the moving particle and the travel distance of the wave triggered at time $t_0 = t - \Delta t$,

$$\theta_c \approx \cos^{-1} \left(\frac{v_{\text{wave}} \times \Delta t}{v_p \times \Delta t} \right), \quad (1.17)$$

where v_{wave} is the phase velocity of the triggered wave. At $v_p = v_{\text{wave}}$, that is $\theta_c = 0$, the Cherenkov radiation wavefront is moving in the same direction as particle.

For an array of moving particles, the Cherenkov waves emitted by different particles would interfere with each other. For the particles in an ordered structure, such as the Wigner crystal on the surface of liquid helium, the interference of the capillary waves generated by moving electrons is constructive when the wave vector \vec{q} of radiated riplons equals the reciprocal lattice vectors \vec{G} of WS, see Fig. 1.11. This is similar to the Bragg scattering of X-rays or neutrons from a lattice. Enhancement in the amplitude of the radiated riplons increases the collision rate of electrons with such riplons, which results in strong increase of the momentum loss of WS. Therefore, the frictional drag force dramatically increases and results in the terminal velocity of WS:

$$v_{\text{BC}} = v_G = \sqrt{\alpha G/\rho}, \quad (1.18)$$

where G is the magnitude of the reciprocal lattice vector. This is the model of the Bragg-Cherenkov scattering which was introduced in 1997 by Dykman and Rubo [?]

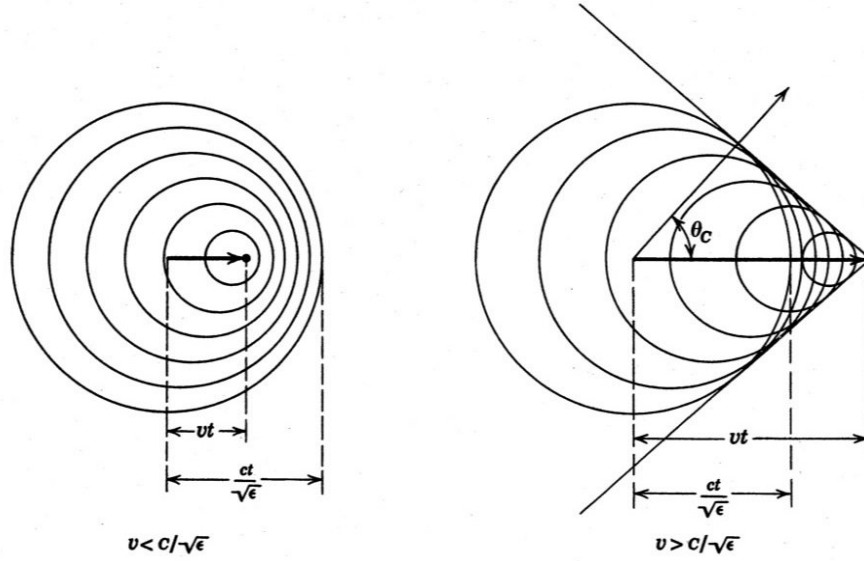


Figure 1.10: Cherenkov radiation. Spherical wavelets of EM field radiated by a particle traveling with a speed less (on the left) and greater (on the right) than the speed of light in the medium. For $v > c/\sqrt{\epsilon}$, an electromagnetic "shock" wave appears moving in the direction given by the Cherenkov angle θ_c . Figure is reproduced from [30].

in order to explain the anomalous electrical conductivity observed in SSEs [27, 31]. In the BC scattering regime, the strong coupling between the WS and coherently emitted ripplons occurs. The constructive interference of surface waves form a commensurate dimple lattice (DL) underneath the electron lattice, such that the deepened surface deformation increases the friction force on electrons and slows down WS, see Fig. 1.12 (a). Under this condition, the effective electron mass increases and the WS mobility decreases dramatically. The drift velocity of the electron lattice is locked at v_{BC} so the electrical current of SSEs is $I_{BC} = en_e v_{BC} w$, where w is the width of WS. Therefore, in the BC scattering regime the differential conductivity of SSEs $dI/dV \approx 0$, until decoupling occurs.

The decoupling of WS from dimples has been shown to be strongly related to the external driving force F_{ext} applied to the WS [27, 32, 33]. The two systems decouple when F_{ext} is larger than some threshold value, $F_{ext}^{(th)}$. For example, as shown in Fig. 1.12 (b), the WS mobility abruptly jumps up when the driving voltage V_{in} exceeds 0.16 V for upward sweep and gets back to its value in the BC scattering regime when V_{in} is lower than 0.135 V for the downward sweep. The threshold voltages for both sweeps vary from run to run within about 10 %. A classical model aimed to explain origin of the threshold driving force $F_{ext}^{(th)}$ was proposed by Vinen who used a simple classical argument [34]. The terminal velocity of WS in the BC scattering regime results from the balance between the driving force F_{ext} and the friction forces exerted on WS. Vinen considered this friction force $F_{DL}^{(||)}$ directed opposite to the WS motion as arising from the reaction force \vec{N} exerted on WS from the dimple lattice, see Fig. 1.13. Correspondingly, he related the friction force $F_{DL}^{(||)}$ to the pressing force $F_{WS}^{(\perp)} \approx eE_{\perp}$

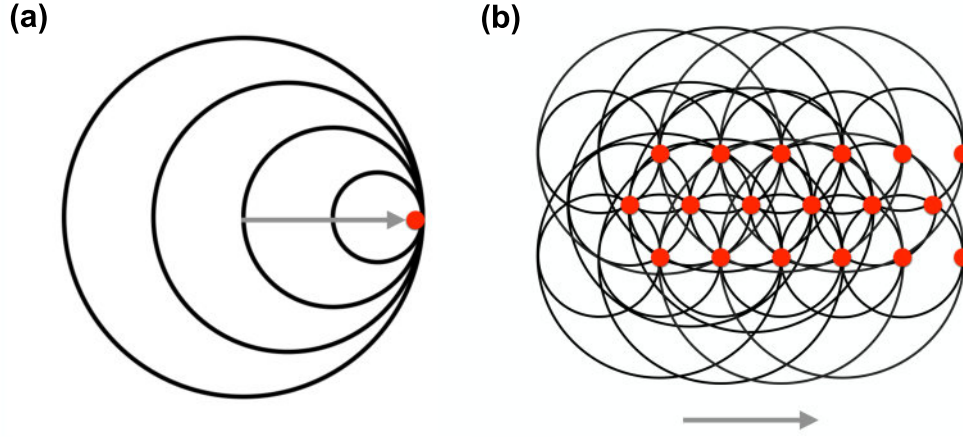


Figure 1.11: BC scattering of moving WS. (a) Cherenkov radiation of a single moving particle when $v_p = v_{\text{wave}}$. The corresponding Cherenkov angle θ_c is zero. (b) Bragg-Cherenkov emission of surface waves by a moving WS on the surface of liquid helium.

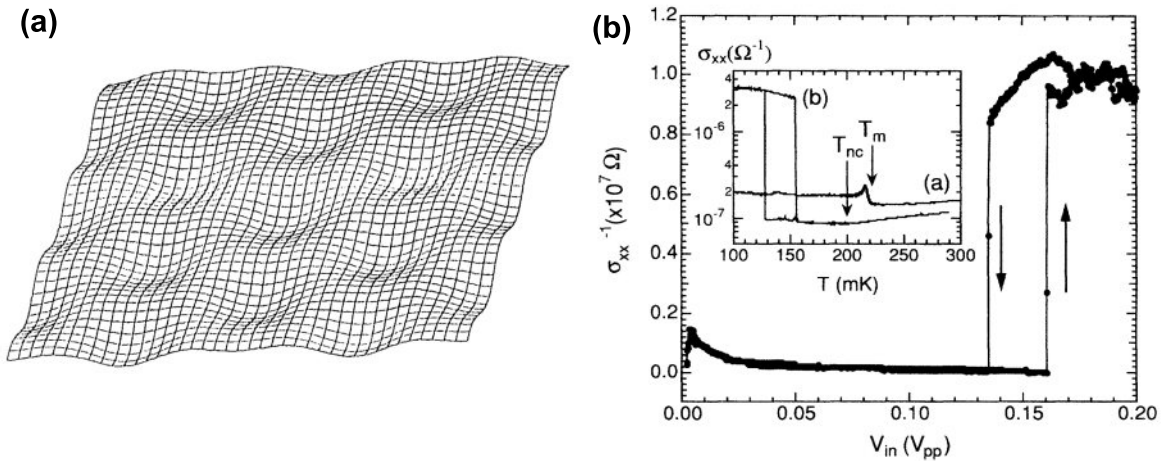


Figure 1.12: Dimple lattice and WS nonlinear mobility. (a) Schematic view of the surface deformation (dimple lattice) induced by the WS on liquid helium. (b) Nonlinear conductivity of WS in the BC scattering regime and sliding transition. Figure is reproduced from [27].

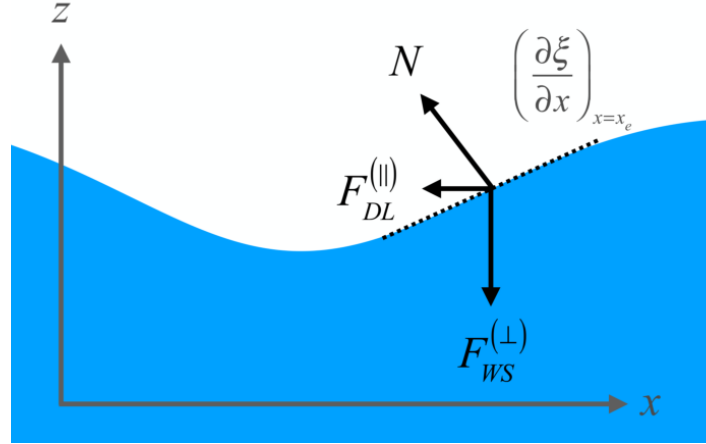


Figure 1.13: Force balance for an electron in dimple. The reaction force \vec{N} on electron from liquid surface must balance the normal force $F_{WS}^{(\perp)}$ and an external driving force F_{ext} (not shown).

exerted on the electron perpendicular to the 2D plane by

$$F_{\text{DL}}^{(\parallel)} = F_{\text{WS}}^{(\perp)} \left(\frac{\partial \xi}{\partial x} \right)_{x=x_e}, \quad (1.19)$$

where x_e is the position of the electron, and ξ is the vertical displacement of the liquid surface in the z direction. Note that the similar expression for the friction force $F_{\parallel} = \frac{\partial U_{\text{int}}}{\partial x}$ can be derived from the expression for the electron-ripplon coupling, $U_{\text{int}} \approx eE_{\perp}\xi$, which has been discussed in Sect. 1.3. Therefore, for a given value of the pressing electric field and a dimple profile $\xi(x)$ there exists a maximum friction force $F_{\text{DL,th}}^{(\parallel)}$ when the local slope attains maximum. Beyond this value the decoupling, or sliding, between WS and DL occurs, which leads to a sudden jump of WS conductivity as shown in Fig. 1.12 (b). However, this simple model does not account for bistable behaviour seen in this figure.

BC scattering occurs when the WS velocity approaches the resonance velocity of ripples and results in the constructive interference of surface waves forming a commensurate lattice of dimples. The physics is essentially described by the textbook problem of a forced harmonic oscillator, where surface vibrations represent the harmonic oscillator and the normal force exerted on the surface by WS represent the periodic driving of oscillator. The amplitude of the oscillator is essentially the depth of the dimple ξ . For an oscillator without damping ξ will become infinity. It is, of course, unphysical. To avoid this unphysical result, Vinen introduced a phenomenological damping coefficient v_d to account for the energy dissipation in the oscillator (the surface waves) and found that ξ decreases with increasing v_d [34]. He suggested that damping arises from two effects: the natural damping of the capillary waves and radiative loss of capillary waves from an electron crystal of finite size. This hints that the sliding properties of the WS can depend on its size. However, no experimental studies of such finite-size effects were done in this system until now.

1.6 Summary

In this chapter, we briefly reviewed the fundamental concepts of the transport theory (Sect. 1.2), the electron-ripplon and electron-atom scattering (Sect. 1.3), the electron-electron interaction and phase transition in SSEs (Sect. 1.4), and the non-linear transport of WS (Sect. 1.5). In the following chapters we describe our experiments where we aimed at achieving further understanding of some puzzling transport properties in the strongly-correlated SSE system on liquid helium, in particular focusing on the nonlinear transport of WS in the Bragg-Cherenkov scattering regime.

Chapter 2

Experimental methods

Recently, it was demonstrated that confining electrons in capillary-condensed microchannel structures facilitates control of the electron system by imposed electrostatic potentials and allow to observe new interesting features associated with the electron transport and phase transitions in the system, such as a clocked electron transport [35], discrete transport through a point-contact constriction [36, 37], suppressed and re-entrant melting of a quasi-1D electron crystal [38–40], stick-slip motion of WS [33], inhomogeneous WS [1], etc. Motivated by these works, we designed and fabricated several microchannel devices for different research topics. We introduced varied configurations of external potential imposed by microscopic electrode structures introduced along the microchannel. In most of our devices, there are two reservoirs located symmetrically on the two ends of a long microchannel in order to provide source of constant SSE flow in the microchannel. One of our device, which will be described in details in Chapter 6, features three such reservoirs connected by a T-shape microchannel. The transport properties of SSEs subjected to the external electrostatic potentials of varied configurations are measured by the standard capacitive (Sommer-Tanner) method and further characterized by the analysis of a lump circuit model.

2.1 Device structure and manufacturing process

In general, the experimental device to study electrical transport in SSEs has the same structure as one for 2DEG in semiconductors. As shown in Fig. 2.1, the device to study electron transport consists of an active channel through which electrons flow from the source to drain. For the system of SSEs floating above liquid helium, we need a channel structure to maintain liquid helium in the source, drain and gate electrode areas. The channels are etched in the insulating material, therefore the depth of channels is defined by the thickness of the insulating layer. The guard electrode on the top of insulating layer is used to avoid charging of the top of the insulating layer. It also helps to confine electrons inside the channel. More negative voltage V_{gu} confines SSEs stronger such that the effective width of the charged system in a channel can be tuned by V_{gu} . Therefore, in order to have an independent control of the width of the electron system in the center microchannel an independent top electrode, the split-gate electrode, is usually introduced along the center microchannel.

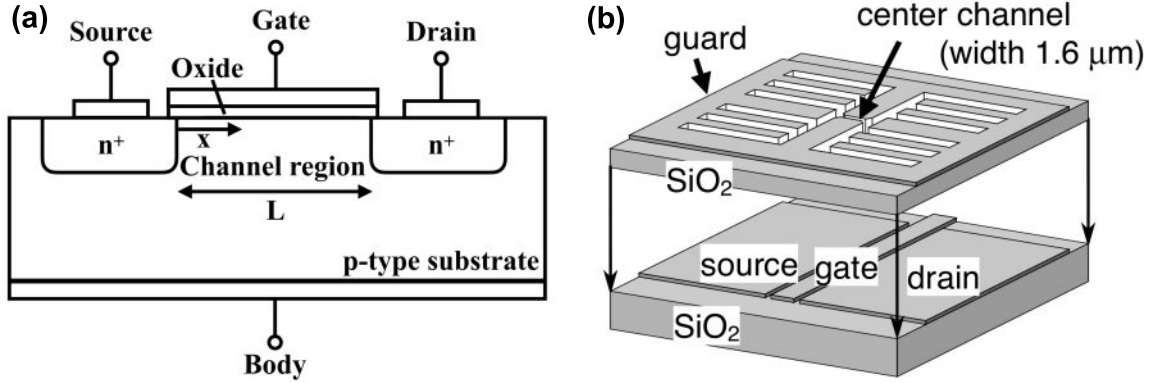


Figure 2.1: Schematic view of the device for SSE experiments. (a) Cross section of a n-type Metal-Oxide-Semiconductor Field Effect Transistor (MOSFET). An electrical potential applied to the Gate electrode controls electron density in channel region. The current of electrons is measured between Source and Drain. (b) Schematics of a microchannel device used for SSE transport measurements. The device has a double-layered structure with a top and bottom metal electrodes separated by an insulating layer. The center channel connects two reservoirs of SSEs. The SSEs are confined in the area above center channel by the negative-biased top guard electrode V_{gu} . The SSE surface density n_e in the center channel is controlled by the voltages applied on the bottom gate electrode and V_{gu} . Figure is reproduced from [41].

Exemplary images of one of the used devices are shown in Fig. 2.2. All the microchannel devices used here are composed of two patterned gold layers separated by an insulating layer. The two layers of gold electrode can be distinguished by the colors in Fig. 2.2 (b). The bottom layer contains the reservoir electrodes, whose functions are similar to the Source and Drain in MOSFET, and the center microchannel electrode, whose functions are similar to the Gate in MOSFET. The top layer is composed of the guard and split-gate electrodes. Those two layers of microscopic structure are prepared by the lithography techniques. For the pattern of spatial resolution higher than $1 \mu\text{m}$, the layer is prepared by the electron-beam lithography (EBL) technique. Otherwise, the micro structure is prepared by the UV lithography technique. The insulating layer varies for different microchannel devices from hard-baked photoresist to silicon nitride. The insulating layer of hard-baked photoresist was made by OFPR or Shipley on hot plate at $250 \text{ }^\circ\text{C}$ for 30 minutes. The silicon nitride insulating layer was prepared by the chemical vapor deposition (CVD) technique. The overall process of sample manufacture starts from the bottom gold layer, then adds a homogenous layer of insulating material of desired thickness. After finishing the top layer on the flat insulating layer, the sample was treated with reactive ion etching (RIE) with sulfur hexafluoride gas until the insulating material is removed and the bottom layer becomes exposed (Fig. 2.2 (e)). Because the etching rate for gold is much slower than the insulating material and the RIE is highly anisotropic, the top-layer gold pattern will act as a mask for etching and result in a vertical groove along the pattern's edge. In this manner, the channel structure is created (Fig. 2.2 (c) and (d)). The final step of the sample manufacture is to make the connections between the electrodes and the 8-lead side braze by a wire

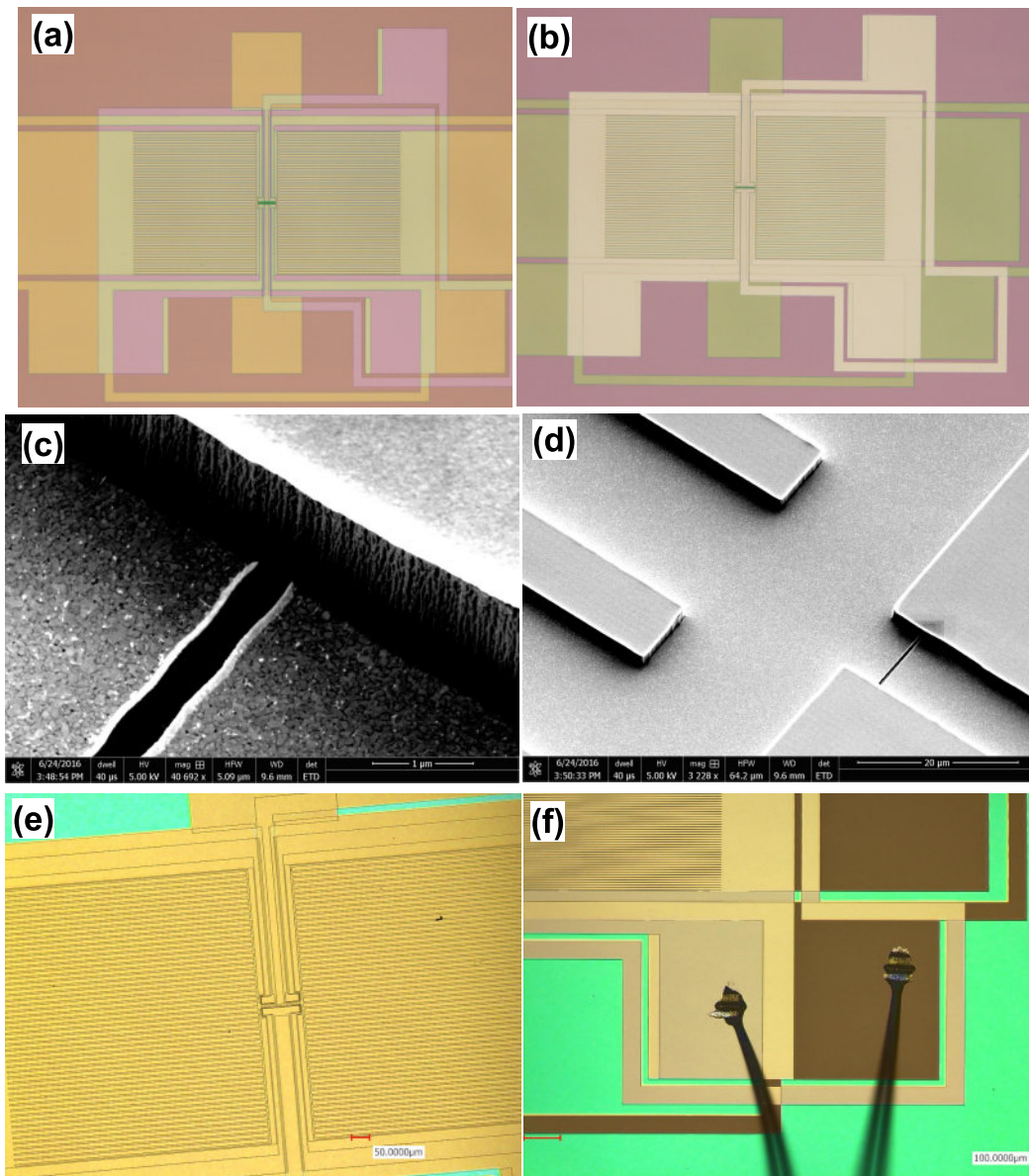


Figure 2.2: Images of microchannel device at different preparation stages. (a) (Microscopic image) The top view of sample after top-layer development. (b) (Microscopic image) The top view of sample after lift-off. The bottom layer is covered by a layer of insulating material which makes it darker than the top layer. (c) & (d) Scanning electron microscopic images of sample after etching. The walls of channel are vertical and sharp. (e) Microscopic image of sample after etching. The bottom layer is exposed such that the colors of bottom and top layers are almost the same. (f) Microscopic image of the wire bond on the sample electrodes.

bonder (Fig. 2.2 (e) and Fig. 2.3).

2.2 Experimental setup

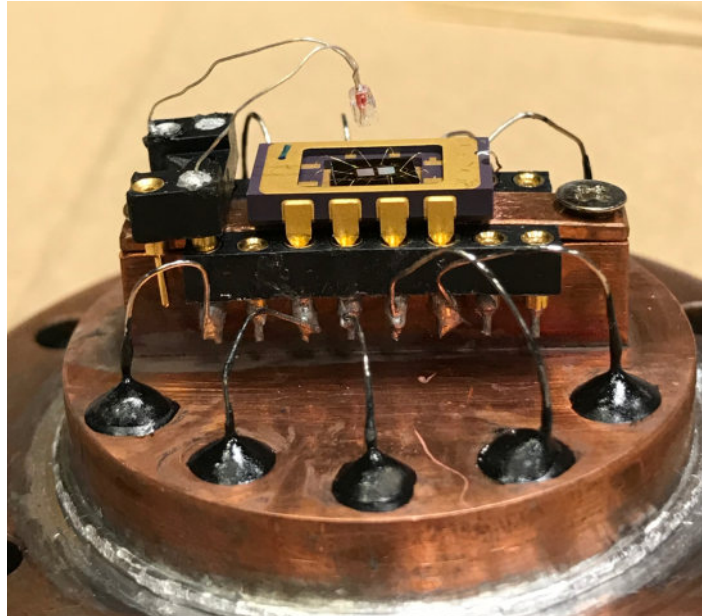


Figure 2.3: Photograph of a microchannel device mounted in a copper cell.

Each microchannel device was mounted horizontally in a vacuum-tight copper cell, see Fig. 2.3. A tungsten filament placed above the device at the distance about 5 mm served as the electron source for charging the liquid ^4He surface in all microchannels. The vacuum-tight copper cell was filled with liquid ^4He and the level of bulk liquid ^4He inside the cell was maintained to be slightly lower than the level of the microchannel device (about 1 mm). All the microchannels, therefore, are filled with the liquid ^4He by capillary action. The suspended helium surface in the microchannel will curve due to the Van der Waals attraction of liquid to the walls of the microchannel. The radius of curvature R_c of the liquid surface depends on the height of the device above the bulk helium level h , as shown in Fig. 2.4 [42]. For the channel of $10\text{-}\mu\text{m}$ width, the depth of the liquid ^4He meniscus ζ_0 is expected to be smaller than 50 nm. If the suspended helium film is charged, the electron pressure will result in the decrease of $R_c = \alpha / \left(\rho g h + \frac{n_e^2 e^2}{2\epsilon_0 \epsilon_{\text{He}}} \right)$, where α is the surface tension of liquid helium, and g is the acceleration due to gravity [43]. For $n_e \approx 10^{13} \text{ m}^{-2}$, we have $\zeta_{n_e} \approx 240 \text{ nm}$. For a sample of $5\text{-}\mu\text{m}$ channel width, $\zeta_0 \approx 12 \text{ nm}$ and $\zeta_{n_e} \approx 60 \text{ nm}$. In the experiments described in the following chapters, we use device with the width of microchannel in the range from 5 to $10 \mu\text{m}$, and channel depth in the range from 0.55 to $1.6 \mu\text{m}$. The reduction of liquid helium thickness for such microchannels is approximately 10 % of the physical channel height for electron density $n_e \sim 10^{13} \text{ m}^{-2}$ for such microchannels. Therefore, for the sake of simplicity the liquid helium height in the channel is assumed to be the geometrical height of channel. This simplification mainly affects the estimation of n_e from the parallel-plate capacitor approximation.

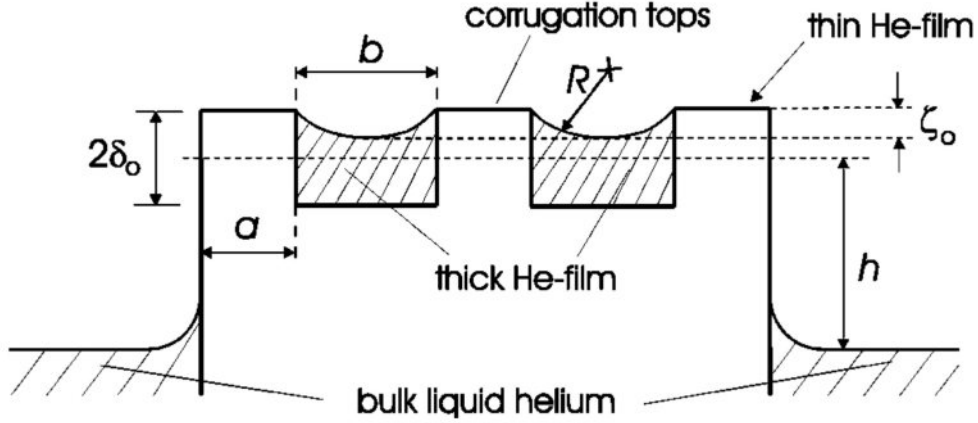


Figure 2.4: Schematic sketch of the suspended helium film in a corrugated surface. Figure is reproduced from [42].

It is convenient to use a simplified capacitance model to find a relation between the density of electrons in the microchannel and voltages applied to different electrodes of the device [37]. First, we define the total capacitance of the liquid surface in the central microchannel $C_\Sigma = C_{\text{bottom}} + C_{\text{top}}$, where C_{bottom} and C_{top} are capacitances between the liquid surface and channel's bottom and top electrodes, respectively (see Fig. 2.5)). It is also convenient to introduce the dimensionless coupling constants $\alpha = C_{\text{top}}/C_\Sigma$ and $\beta = C_{\text{bottom}}/C_\Sigma$, which satisfy the obvious relation $\alpha + \beta = 1$. Then, the potential at the uncharged liquid surface can be written as $V_s = \alpha V_{\text{top}} + \beta V_{\text{bottom}}$. When the device is charged with electrons, the potential of the charged liquid surface V_e has to be the same everywhere, owing to high mobility of the surface electrons on liquid helium. The value of V_e is determined by voltages applied to the reservoir's bottom and guard electrodes and amount of electrons in the reservoir, and is assumed to be fixed once the device is chargedⁱ. Then, by the definition of capacitance we can write for the total charge Q of electrons in the channel $Q = C_\Sigma(V_e - V_s)$. A further simplification can be made by assuming a uniform density distribution of electrons in the channel, that is $Q = -en_e S$, where n_e is the areal density of surface electrons, $e > 0$ is the electron charge, and S is the channel area. Such a parallel-plate capacitance approximation is partially justified by a large aspect ratio (~ 10) of a wide and shallow microchannel used in our device. Using $C_{\text{bottom}} = \epsilon\epsilon_0 S/d$, where d is the height of the microchannel in our device, we obtain required relation

$$n_e = \frac{\epsilon\epsilon_0}{\beta ed} (\alpha V_{\text{top}} + \beta V_{\text{bottom}} - V_e) = \frac{\epsilon\epsilon_0}{\beta ed} (V_s - V_e). \quad (2.1)$$

In addition to the simplified capacitance model mentioned above, the electron density n_e can be calculated by numerically solving the Poisson equation with the aid of finite-element model (FEM). We define an electrostatic model of our channel, where the SSE system is represented by an equipotential plane along the helium surface at

ⁱOccasionally, loss of electrons from the device is observed, which is reflected in discontinuous jumps of the measured current I . Such data are not considered here.

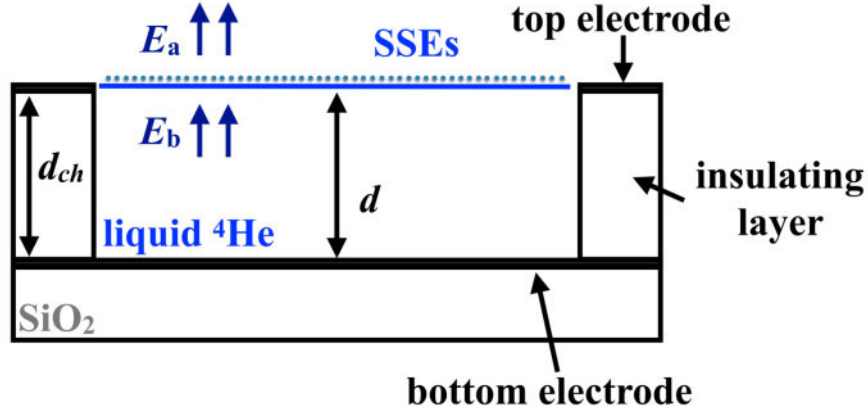


Figure 2.5: Parallel-plate capacitor model. The charged liquid helium surface is approximated by a conducting plate parallel to the bottom electrode. From this model, relation between electron density n_e and voltages applied to electrodes can be found, see Eq. (2.1) in the text.

potential V_e . According to the Gauss's law, the electron-density distribution $n_e(x, y)$ is retrieved from the difference of perpendicular components of electric fields E_a and E_b above and below the electron system, respectively, see Fig. 2.5, $n_e = \frac{\epsilon\epsilon_0}{e} (E_a - E_b)$. From these calculations, we directly obtain the width w and length l of the electron system in the channel, which is always somewhat less than the geometric channel size W and L . An example of calculated profiles are shown in Fig. 2.6. The value of V_e (horizontal dotted line), which represents the potential of the electron system in our model, is determined experimentally. The resulting electron-density profile $n_e(y)$ across the channel is not homogeneous (orange closed square symbols). In the following, we define the electron density n_e as the average value $n_e^{(\text{aveg})} = (1/w) \int_{-w/2}^{w/2} n_e(y) dy$ (blue dash-dotted line).

The profile of potential $V_s(y)$ at the uncharged liquid surface can be numerically estimated by using FEM that solves the Poisson equation subject to the boundary conditions. It is found that $V_s(y)$ largely depends on the channel geometry (the black solid line in Fig. 2.6). For the shallow channel geometry, the profile can be approximated as a hyperbolic cosine function $V_s(y) = A[\cosh(By) - 1] + V_s(0)$ (the red dash-dotted line in Fig. 2.6). The coefficients A and B can be obtained from fitting to the exact profile obtained by the FEM calculations. Since $n_e(y)$ is maximal in the center and quickly decreases towards the channel walls, the effective capacitive coupling between the SSEs and the bottom channel electrode mainly comes from the SSEs at the channel center. In the simplified capacitance model mentioned above, see Eq. (2.1), the values of α and β , which determine V_b , are estimated by FEM calculated value of $V_s(y = 0)$. The value of $n_e(y = 0)$ estimated by Eq. (2.1) (the dark-yellow dashed line in Fig. 2.6) is fairly close to the averaged $n_e^{(\text{aveg})}$ estimated from the Gauss's law (the blue dash-dotted line in Fig. 2.6), while the width \bar{w} at $V_e = V_s(y)_{y=\pm\bar{w}/2}$ is close to the width of electron system w . Therefore, the $n_e^{(\text{aveg})}$ and w can be approximately retrieved by equating V_e to the fitted function $V_s(y)$. Similar approximate methods were used in previous

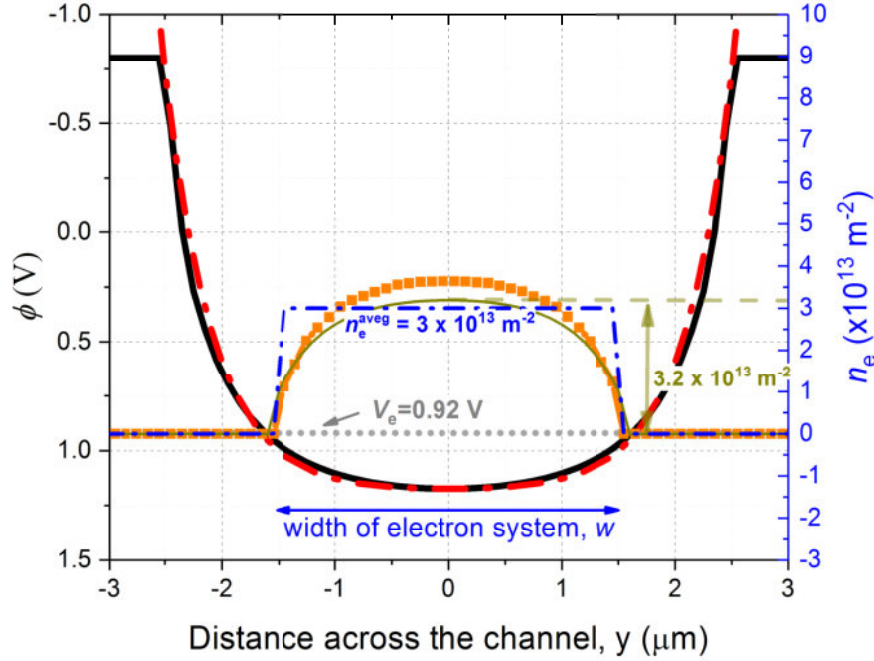


Figure 2.6: Electrostatic potential and electron density profiles across the channel obtained by different methods as described in the text. Left axis: The black curve is the FEM calculated potential profile across the center channel without SSEs. The red dot-dashed line is the fitting by a function $V_s(y) = A[\cosh(By) - 1] + V_{s,y=0}$. Right axis: The orange (closed squares) symbols is the SSE density profile calculated by FEM. The blue curve is the averaged n_e calculated from the above profile. The dark yellow curve is calculated using $n_{e,\text{ch}}(y) = \epsilon_0 \epsilon (V_s(y) - V_e) / (ed\beta)$. The simulations are done for a microchannel of width $w = 5 \mu\text{m}$ and height $0.55 \mu\text{m}$ with $V_{\text{sg}} = -0.8 \text{ V}$, $V_{\text{ch}} = 1.5 \text{ V}$ and $V_e = 0.92 \text{ V}$.

studies to obtain estimation of n_e in microchannel devices [37, 40]. Alternately, electron density of WS can be estimated from transport data in BC scattering regime, as will be described later.

2.3 Measurements and analysis

The current of SSEs through the center channel I_{ch} is measured by the standard capacitive (Sommer-Tanner) method and analyzed by the lumped-circuit model shown in Fig. 2.7. An ac voltage V_{in} at the frequency f was applied to the electrode of left reservoir, and the output current I_{out} is measured with a lock-in amplifier at the bottom electrode of right reservoir. Due to the symmetry of the left and right reservoir area of the microchannel device, the capacitances between the charged liquid surface and the bottom reservoir (top guard) electrode on both sides are assumed to be the

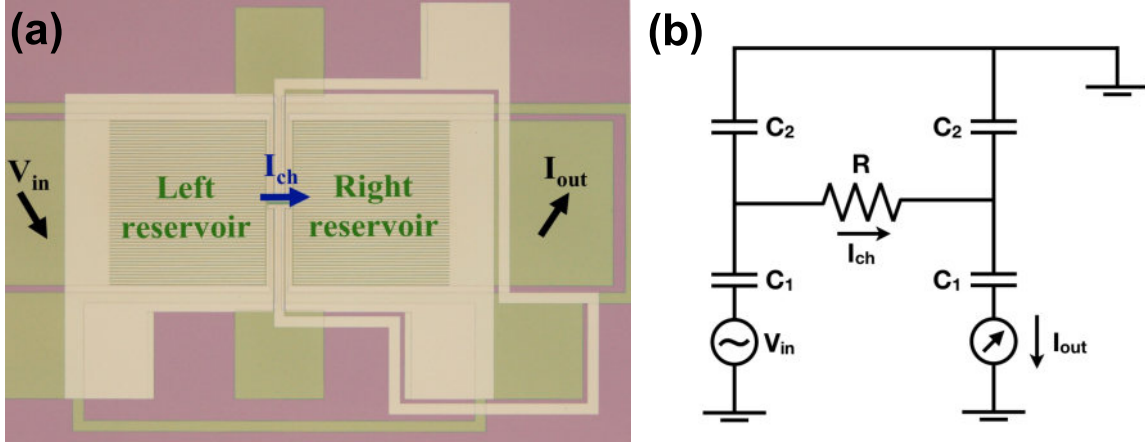


Figure 2.7: Electrical lumped-circuit model of a charged microchannel device. (a) The left reservoir electrode on the bottom layer is driven by V_{in} , and the response current I_{out} is measured from the right reservoir electrode. I_{ch} is the current of SSE flow in the center channel. (b) The electrical lumped-circuit model used for retrieving I_{ch} and the resistance of the SSEs in the center channel R .

same, indicated as C_1 (C_2). In the lumped-circuit model, we obtain

$$I_{\text{out}} = \frac{i\omega C_1}{2 + i\omega C_0 R} V_{\text{in}}, \quad (2.2)$$

where $C_0 = C_1 + C_2$. When R varies, the plot of the component of current I_{out} in phase with V_{in} , $\text{Re}(I_{\text{out}})$, versus the quadrature component, $\text{Im}(I_{\text{out}})$, is a semicircle. The relation between the radius of the semicircle r_0 and C_0 is $C_0 = (4r_0)/(\omega\beta V_{\text{in}})$, where $\beta = C_1/C_0$. Therefore, the value of C_0 for a particular microchannel device can be determined by the numerical fitting of the $\text{Re}(I_{\text{out}})$ vs $\text{Im}(I_{\text{out}})$ plot (Fig. 2.8), while the value β can be numerically determined by the finite element method (FEM) [37, 44]. After the value of C_0 is found, the resistance R and the current I_{ch} of electrons in the center channel can be obtained by the following equations

$$R = \frac{1}{2\pi f C_0} \sqrt{\frac{V_{\text{in}}^2 (2\pi f)^2 C_0^2 \beta^2}{I_{\text{out}}^2} - 4}, \quad (2.3)$$

$$I_{\text{ch}} = \frac{I_{\text{out}}}{\beta}, \quad (2.4)$$

With the knowledge of R and I_{ch} , the voltage drop across the channel V_{ch} can be also estimated.

As discussed in Ch. 1, in the regime of BC scattering we observe a BC plateau of current $I_{\text{BC}} = en_e v_{\text{BC}} w$. Therefore, we can retrieve the electron density n_e from the measured current I_{BC} by the following relation

$$n_e = \left(\frac{I_{\text{BC}}}{ew} \sqrt{\frac{\rho}{\sqrt{2}\sqrt[4]{3}\pi\alpha}} \right)^{4/5}. \quad (2.5)$$

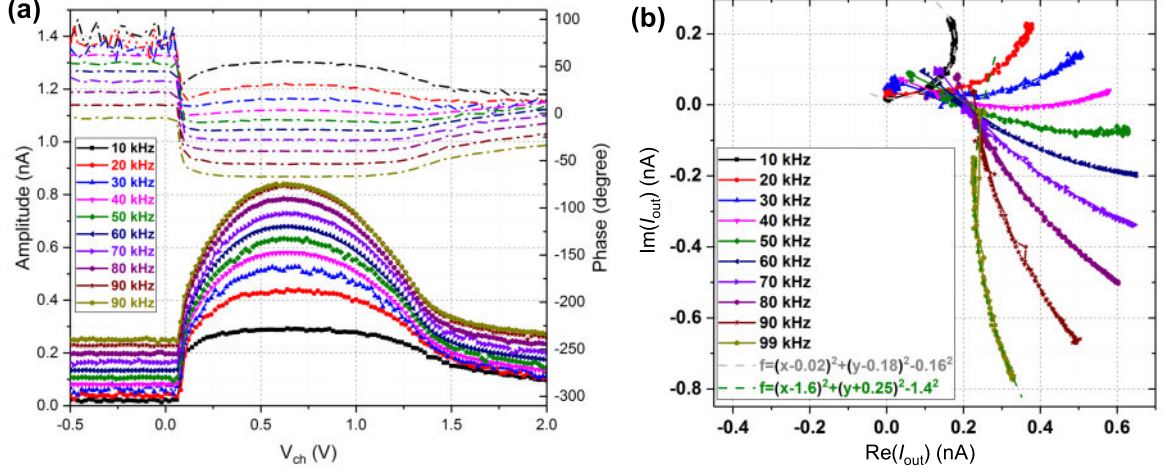


Figure 2.8: Examples of experimental data obtained using one of our microchannel devices. (a) Amplitude (symbols) and phase (dashed-dotted lines) of current I_{out} versus voltage V_{ch} applied to bottom electrode of central channel for different values of driving frequencies. The data were taken using device described in Ch. 4 at $V_{in} = 5$ mV_{p.p.}. With the increase of V_{ch} , n_e in the channel starts to increase from zero, where it shows a constant amplitude and phase of background current, to a higher value close to WS crystallization. The current amplitude first increases due to conduction through the channel and then decreases due to crystallization of SSEs and increase of the resistance R of the channel. (b) Plots of $\text{Im}(I_{out})$ vs $\text{Re}(I_{out})$ using data in (a).

As described above, the effective width of SSE system in the channel $w = w(n_e)$ can be determined by equaling V_e to $V_s(y)_{y=\pm w/2}$. Therefore, from Eq. (2.1) we get

$$n_e = \frac{\varepsilon\varepsilon_0}{ed} A \left[\cosh\left(B\frac{w}{2}\right) - 1 \right]. \quad (2.6)$$

Consequently, for a given I_{BC} , both n_e and w can be retrieved by solving Eq. (2.5) and Eq. (2.6).

In the lumped-circuit analysis of ac-driven SSEs described earlier we assumed the linear relationship between applied voltage V_{in} and SSE current I_{ch} . For the transport of WS in the BC scattering regime, the analysis is slightly complicated by a nonlinear dependence of I_{ch} on driving voltage. Fig. 2.9 shows time-resolved measurements of current I_{out} in the BC scattering regime. The measured current significantly deviates from sinusoidal due to its saturation at the BC value I_{BC} . This affects the results obtained by a lock-in amplifier which measures the first harmonic of the current signal at the reference frequency. The lock-in signal in the case of a non-linear response of SSE can be modeled by an analytical expression

$$I_{\text{lock-in}} = \frac{\pi}{4} \left(\int_{-\frac{\pi}{2}}^{-\frac{\pi}{2} + \arcsin\left(\frac{I_{BC}}{s \times V_{in}}\right)} s \times V_{in} \cos \phi \times e^{-i\phi} d\phi + \int_{-\frac{\pi}{2} + \arcsin\left(\frac{I_{BC}}{s \times V_{in}}\right)}^0 I_{BC} \times e^{-i\phi} d\phi \right), \quad (2.7)$$

where I_{BC} is an adjustable parameter and s is an experimentally determined slope of the linear IV -dependence far from the BC scattering regime. The amplitude and phase measured by lock-in, together with fitting by Eq. (2.7), as shown in Fig. 2.10.

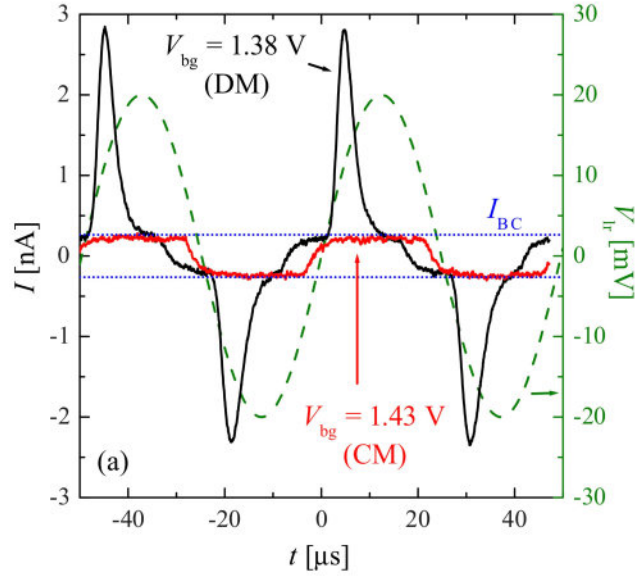


Figure 2.9: Time-resolved transport measurement for SSEs in the BC scattering regime. Current recorded for SSEs in the BC scattering regime (solid lines, left axis) as well as the sinusoidal driving voltage V_{tr} (dashed line, right axis) versus time t . The blue dotted lines show the value of current I_{BC} at the BC plateau. Sharp peak of current observed in trace marked by DM is due to WS sliding. Figure is reproduced from [45].

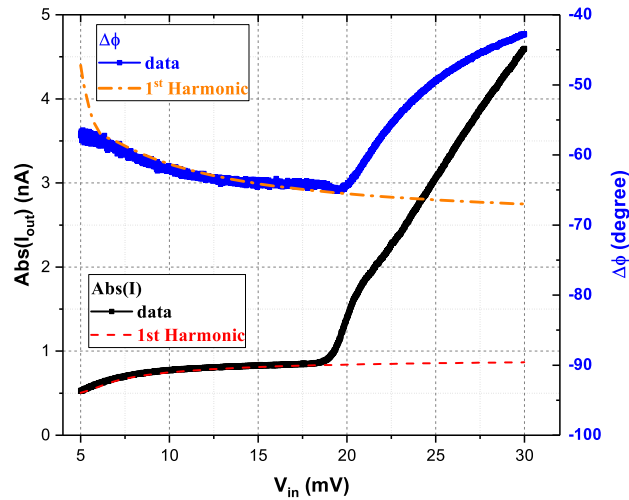


Figure 2.10: Amplitude and phase of current I_{out} measured by a lock-in amplifier versus the amplitude of driving voltage for WS in nonlinear transport regime. The dashed and dash-dotted lines are fittings using Eq. (2.7) with fitting parameter $I_{\text{BC}} = 0.51$ nA.

Chapter 3

Inhomogeneous WS and multiple BC plateaus

In our first experiments, we studied transport of SSEs which had a nonuniform density n_e along the channel. In particular, the transport features attributed to the electron ordering, such as the BC scattering and the WS sliding, were probed and compared for three cases: (1) a homogeneous WS in a 400 μm -long channel, (2) a small WS island of 20 μm in length formed at the center of the channel filled with electron liquid (EL), and (3) an inhomogeneous WS composed of two electron lattices with different lattice constants. For the inhomogeneous WS, we found two separate BC scattering plateaus and WS sliding transitions attributed to each individual WS. The corresponding IV -curves are explained in terms of an interplay between transport properties of two WSs connected in series.

3.1 Experiment

The microchannel device used in the experiment is shown in Fig. 3.1 (a). The device consisted of an array of 1.5- μm -deep channels, fabricated on a silicon dioxide substrate using optical lithography. Four sets of 20- μm -wide channels connected in parallel, which serve as electron reservoirs, are connected to a single central channel that is 10 μm wide and 400 μm long (Fig. 3.1 (a), inset). A schematic picture of the device is shown in Fig. 3.1 (b). In the experiments discussed here only two electron reservoirs (R1 and R2) of the device were used in the measurements, while two others were kept empty.

The electrostatic potential in the reservoirs and the central channel is controlled by several electrodes integrated into the device architecture. Two electrodes, each covering the bottom of one of the reservoirs and the adjacent part of the central channel, are denoted as reservoir electrodes. The potential of these electrodes is denoted as V_R . The electrode covering the top of the channel ribs is denoted as the guard electrode, and its potential is denoted as V_{Gu} (during the measurements it was always grounded, so $V_{\text{Gu}} = 0$). The potential difference $V_R - V_{\text{Gu}} > 0$ confines the electron system and controls the electron density in the reservoirs (n_r) and in the central channel (n_{ch}). The $20 \times 10 \mu\text{m}$ gate electrode, with potential V_G , is defined in the middle of the central

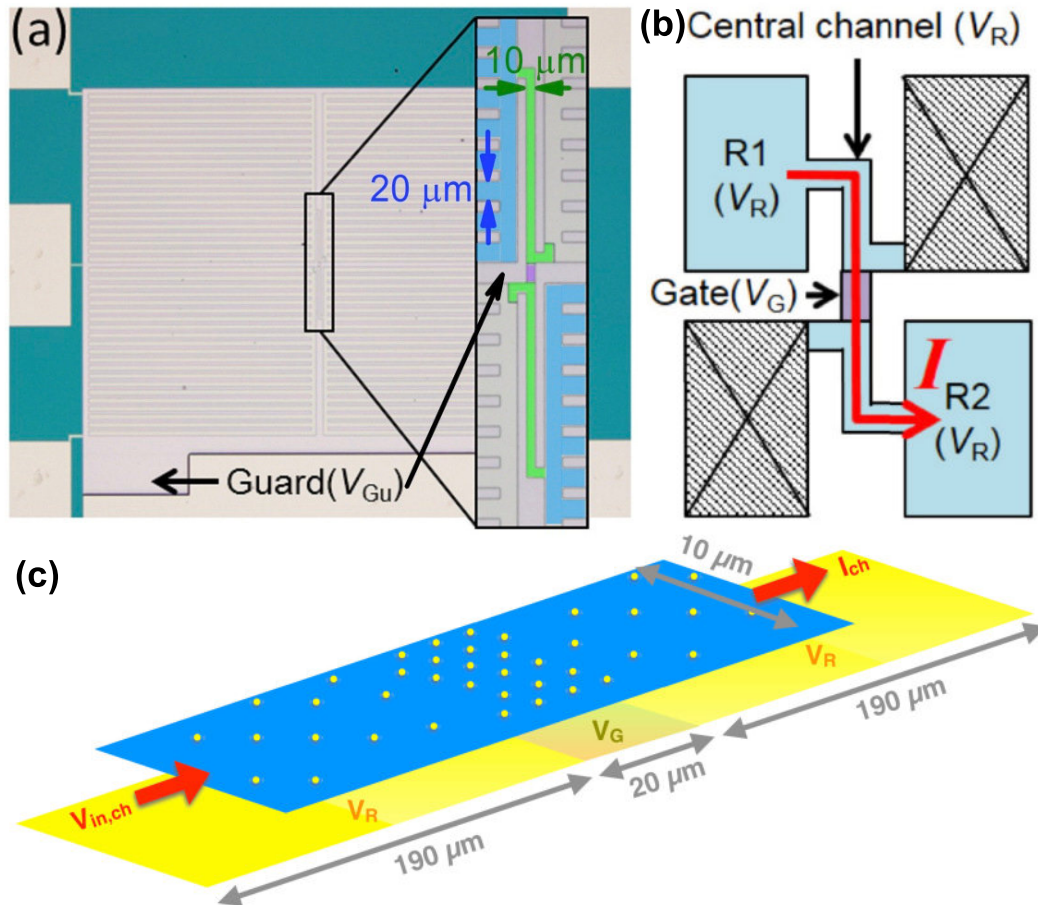


Figure 3.1: Microchannel device for study of an inhomogeneous WS. (a) Microscopic image of the microchannel device used for the inhomogeneous WS study. There are four reservoirs in this sample. Only two reservoirs (R_1 and R_2 in (b)) are used in the measurement, while two others were kept empty (negatively biased). Inset: (false colored) the structure of the center channel. (b) & (c) A sketch of the experimental circuit, where the current of SSEs is driven between reservoirs R_1 and R_2 through the center channel.

channel at the bottom. The potential difference $V_G - V_{Gu} > 0$ controls the electron density in the section of the central channel above the gate n_g . Thus, n_g could be made significantly different from n_{ch} . The current of SSEs through the central channel is measured by the Sommer-Tanner techniques described in Ch. 2 at driving frequency of 99.5 kHz.

The possibility to apply different independent potentials V_R and V_G to channel and gate electrodes allows for three distinct states of SSEs in microchannel. In the first case, we apply the same potential $V_R = V_G$ to each electrode. Under this condition, the SSE density is homogeneous along the whole center channel, $n_{ch} = n_G$. For high enough density n_{ch} , a homogeneous WS is formed and fills the whole channel. In the second case, sufficiently large voltage $V_G > V_R$ is applied to the gate to form WS only along the gate electrode, while keeping EL in the rest of the channel. In the third case, sufficiently large independent voltages V_G and V_R are applied to form distinct WSs above both the gate and channel electrodes, with different n_e and lattice constants.

3.2 Results and Discussion

Fig. 3.2 shows the IV curves measured at 0.58 K for the three cases mentioned above. Fig. 3.2 (a) shows IV -curves when $V_R = V_G$ (homogeneous n_e along the channel) for three different values of V_R . As V_R increases, the n_e increases and SSEs form a WS in the center channel. The expected length of the WS is about the length of the whole center channel, 400 μm . When the WS forms, the clear BC scattering plateau appears. This data also show that decoupling onset of BC scattering increases with the applied voltage V_R . Fig. 3.2 (b) is the second case of a WS island above the gate electrode. In this case, V_R is maintained at 0.3 V while a different bias V_G is applied to the gate. Fig. 3.2 (b) shows IV -curves for several values of V_G . With increasing V_G , the BC scattering plateau starts to develop, and the decoupling onset shows the same trend as the homogeneous WS case. The length of the WS island is estimated to be about the length of the gate electrode, i.e. 20 μm . Fig. 3.2 (c) is the third case of inhomogeneous WS. For sufficiently large V_G and V_R , there are three segments of WS in the center channel connected in series, see Fig. 3.1 (c). Fig. 3.2 (c) shows IV -curves for fixed value of $V_R = 1.5$ V and different values of V_G . In general, IV -curves exhibit multiple plateaus. While one plateau of BC scattering is always presented when V_R is fixed at 1.5 V, the second plateau starts to develop with increasing V_G . In Fig. 3.2 (d), we compared the individual plateaus of individual WS from the first and second case with the multiple plateaus from the third case. It is found that the I_{BC} values of the two plateaus in case of two WSs in series are the same as the values in the case of the single WS. This allows to identify two plateaus to be due to BC scattering induced by two individual WSs.

The behavior of the whole IV -curve for different values of V_G can be understood as an interplay between transport properties of two individual WSs connected in series, which in turn depend on driving electrical field E_{\parallel} in each segment of inhomogeneous WS. Since the density of SSE in microchannel is fixed, the current I through the cross section of different segments of microchannel should be the same. For Drude model, $I = en_e v_d w$, where $v_d = \mu E_{\parallel}$ is the drift velocity. For the WSs connected in series, the

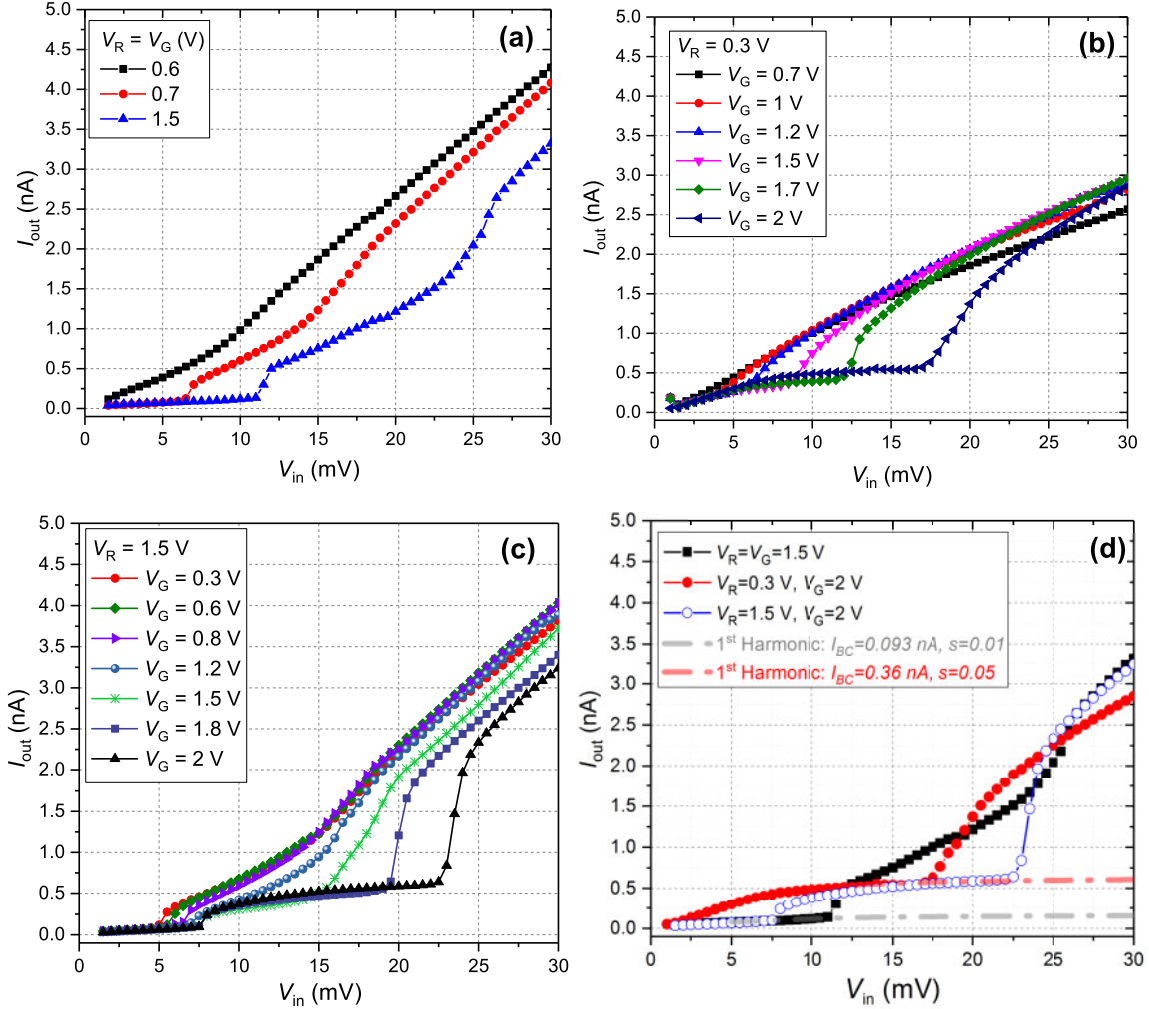


Figure 3.2: I_{out} vs V_{pp} measured at $T = 0.58$ K and $V_{\text{Gu}} = 0$ V. (a) Homogeneous WS all along the channel. The expected length of the WS is about the length of the whole center channel, $400 \mu\text{m}$. (b) WS island above the gate electrode. The length of the WS island is estimated to be about the length of the gate electrode, i.e. $20 \mu\text{m}$. The other parts of the center channel is maintained in the liquid phase. (c) Inhomogeneous WS. The two BC scattering plateaus result from the interplay of the WSs of different lattice constants in the center channel. (d) Three above cases plotted together on the same graph. The dash-dotted lines are fitting of the lock-in response as described in Chapter 2.

applied driving voltage V_{in} is the sum of voltage drops of each segment. Therefore,

$$V_{\text{in}} = V_{\text{in}}^{(\text{ch})} + V_{\text{in}}^{(\text{G})} = E_{\parallel}^{(\text{ch})} \times L_{\text{ch}} + E_{\parallel}^{(\text{G})} \times L_{\text{G}} = \frac{I}{e} \left[\frac{L_{\text{ch}}}{n_{\text{ch}} \mu_{\text{ch}} w_{\text{ch}}} + \frac{L_{\text{G}}}{n_{\text{G}} \mu_{\text{G}} w_{\text{G}}} \right], \quad (3.1)$$

where L_{ch} and L_{G} are the length of channel and gate electrodes, respectively. Because V_{G} and V_{R} are different and because the two crystalline sections L_{ch} and L_{G} have different lengths, the driving electric field E_{\parallel} applied to the SSE in each WS is different. In Fig. 3.2 (c), the shifts of sliding onset of the first BC scattering plateau may be affected by the fact that the ratio of $V_{\text{in}}^{(\text{ch})}$ to $V_{\text{in}}^{(\text{G})}$ is changing.

For each WS, the sliding from the dimple lattice occurs when the driving force per electron eE_{\parallel} reaches a threshold value that depends on the electron density and the pressing electric field. Once decoupled from the dimple lattice, the WS resistivity drops significantly. For two WSs connected in series, the sliding of one WS from the dimple lattice therefore leads to an increase in the driving force applied to SSEs in the second WS. While the drift velocity of second WS increases with increasing $V_{\text{in}}^{(\text{G})}$ and approaches its resonance velocity of BC scattering $v_{\text{BC}}(n_{\text{e}})$ (see Eq. (1.18)), the BC plateau of the second WS develops. When the $V_{\text{in}}^{(\text{G})}$ is sufficiently large to decouple the WS above the gate electrode, the second sliding occurs. For the short gate region, E_{\parallel} becomes very large once the SSEs in the rest of the channel are decoupled from the dimple lattice; the BC scattering can be observed only when the pinning force becomes sufficiently strong, thus when V_{G} is large. For lower V_{G} , once the SEs in the main part of the channel become decoupled, the value of E_{\parallel} in the gate area becomes large enough to immediately induce sliding of SEs above the gate area. As a result, we observe a single sliding transition in the whole channel at lower V_{G} and two distinct sliding transitions in the main part of the channel and above the gate at higher V_{G} .

The decoupling of WS from dimples leads to an abrupt change in electron current. Therefore, it is convenient to represent data in terms of the differential conductivity dI/dV . Such data are summarized and plotted in Fig. 3.3. The line between the area I and III in the figure indicates the first sliding transition due to the long WS above the center channel electrode. When n_{G} approaches n_{ch} , the transition line splits into two lines to form a characteristic Y-shape. The two lines correspond to two WS sliding transitions, one in the WS above the center channel electrode and the other in the WS above the gate electrode. Since the width of microchannel in the reservoirs is wider than the one in the central channel, $n_{\text{r}} > n_{\text{ch}}$. Therefore, whenever n_{ch} is high enough to form a WS, the SSEs in reservoir area much have been in crystal phase already. While in general, the resistance of the device is mainly determined by the flow of SSEs in the channel, in BC scattering regime the total current I_{out} can be affected by the transport of electrons in the reservoirs. Therefore, we suspect that the line enclosing the area IV is due to the sliding transition of WS in the reservoir.

3.3 Summary

We have investigated and compared transport properties of (1) a homogeneous WS, (2) a WS island in EL, and (3) an inhomogeneous WS formed on the surface of liquid

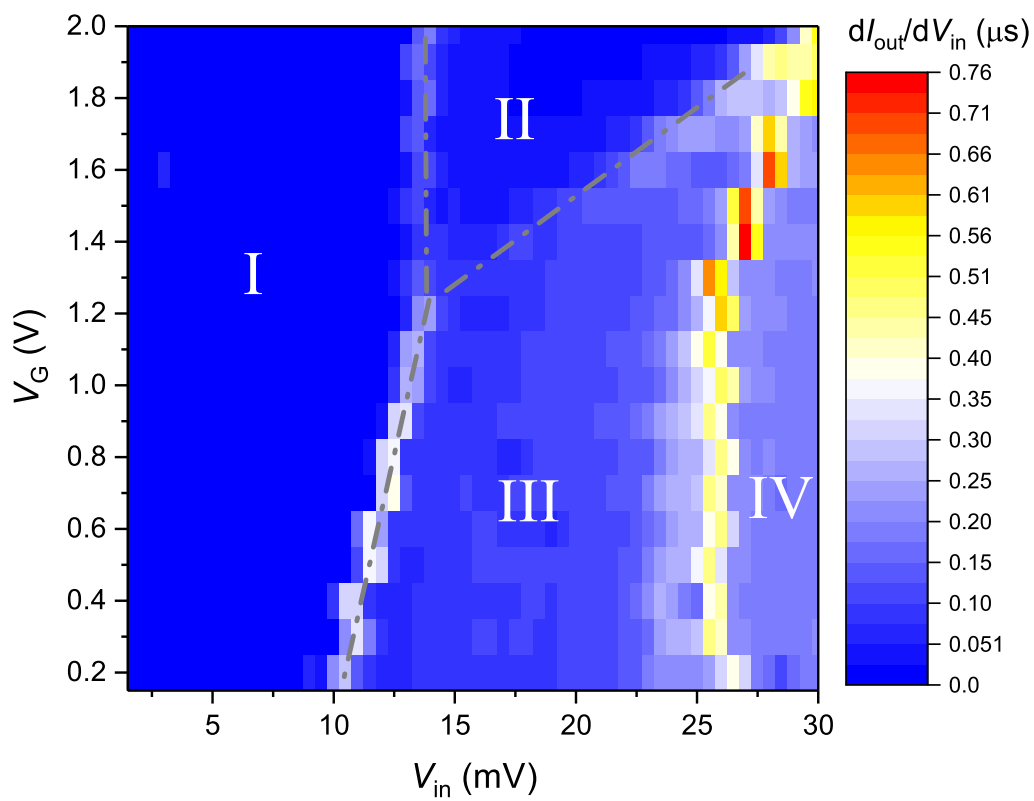


Figure 3.3: Differential conductance $dI_{\text{out}}/dV_{\text{in}}$ vs V_{in} and V_{G} measured at $T = 0.58 \text{ K}$, $V_{\text{ch}} = 1.5 \text{ V}$. Labels I-IV correspond to different transport regimes as discussed in the text. The Y-shaped dash-dotted line serves as an eye guide.

helium, in a microchannel geometry. For the homogeneous WS our observations are in good agreement with previous studies. For the WS island, we found that characteristic WS transport phenomena are retained at least down to a WS size of $20 \mu\text{m}$. For the inhomogeneous WS, the transport properties can be explained by the interplay of the transport of two distinct WSs connected in series.

In our first experiment, we have demonstrated possibility to create a WS of sufficiently small size ($\approx 20 \mu\text{m}$) and studied its transport properties. In the next chapter, we described our studies of the relationship between the size of WS and its nonlinear transport properties.

Chapter 4

Effect of finite size of WS on its nonlinear transport

As discussed in Ch. 1, Vinen predicted dependence of the nonlinear transport features for WS, in particular the sliding threshold of driving force, on the size of WS. This arises from the loss of coherently excited riplons from the system's boundary. In the previous chapter, we demonstrated possibility to study nonlinear transport properties of a small WS island created in a microchannel. This motivated us to design a sample suitable to study nonlinear transport of WS of varied size to observe the finite-size effects predicted by Vinen. This studies are subject of this chapter.

4.1 Theoretical framework

As a theoretical framework for our experiments we use Vinen's model which has been discussed in Sect. 1.5. In addition to explaining the mechanism of resonant enhancement of dimples and their coupling to driven WS, it also allows to estimate the maximum (threshold) driving force before WS decouples from dimples. According to Vinen's model, the friction force exerted by a dimple on the electron is related to the surface displacement, see Fig. 1.13. The latter can be found from the Laplace equation describing waves on a free surface of liquid:

$$-\frac{\partial p}{\partial t} + \rho \frac{\partial^2 \phi}{\partial t^2} - \alpha \frac{\partial}{\partial z} \left(\frac{\partial^2 \phi}{\partial x^2} \right) = 0, \quad (4.1)$$

where ϕ is the velocity potential, p is the pressure on the surface exerted by the WS, ρ is density of liquid, α is the surface tension, z -direction is perpendicular to the surface, and x -direction is in the direction of the WS motion. In addition, the relation between the velocity potential ϕ and the displacement of the surface element ξ is $\partial\phi/\partial z = \partial\xi/\partial t$. The pressure on the surface exerted by an infinitely long WS moving with velocity v_x can be described as $p = n_e e E_{\perp} \text{Re} [e^{i(G_1 x - \omega t)}]$, where G_1 is the magnitude of the smallest reciprocal lattice vector, $\Omega = v_x G_1$, and we take into account only the first harmonic of Fourier expansion of $p(x)$. Eq. (4.1) is similar in structure to the equation of motion for a frictionless harmonic oscillator driven by a periodic force. In our case, the eigenfrequencies of oscillator correspond to the capillary wave spectrum, $\omega_q = \sqrt{q^3 \alpha / \rho}$, and

the resonance is expected when $\omega_q = v_x G_1$. The steady-state solution of Eqs. (4.1) and $\partial\phi/\partial z = \partial\xi/\partial t$ describes the surface deformation. The maximum amplitude of the periodic surface displacement is

$$\xi_0 = \frac{n_e e E_\perp}{\rho G_1} \frac{1}{v_1 v_d}, \quad (4.2)$$

where $v_1 = \sqrt{G_1 \alpha / \rho}$ and v_d is the phenomenological damping coefficient introduced by Vinen to account for the energy dissipation in the oscillator. The energy loss in the coupled WS-DL system includes the natural damping of riplons and the radiative loss of riplons through system's boundary [34]. In addition, distribution of defects in the electron lattice may also contribute to v_d . Eq. (4.2) shows that the maximum amplitude of the resonant riplons ξ_0 decreases with increasing damping parameter v_d and increases linearly with increasing pressing force from WS. The corresponding maximum force obtained by Vinen is given by

$$F_{\max} = e E_\perp \left(\frac{\partial \xi}{\partial x} \right)_{x=x_1} = \frac{n_e e^2 E_\perp^2}{\rho v_1 v_d}, \quad (4.3)$$

where the slope of the liquid surface in the above equation is evaluated at $x_1 = \Omega t / G_1$.

Situation could be more complicated when the driving force on the moving WS is not constant as usually happen in ac driven WS. Since the Fourier components of the dimple profile are time-averaged quantities, they were found to be strongly dependent on the alternating driving field conditions [46]. Under an ac driving at frequency ω , the dimple profile appears to be dependent on the ratio ω/γ_q , where γ_q is damping rate of riplons with wave number q . For $\omega \ll \gamma_q$, the resulting dimple shape is close to the one obtained for dc driving. For $\omega \geq \gamma_q$, interference of riplons generated at different times during oscillatory period of ac drive makes it more complicated. Fig. 4.1 shows the theoretical curves for a dimensionless function Q , where Q represents the driving electric field E_x , versus the normalized drift velocity $u_0 = v_x/v_1$ (note that in the Drude regime $v_x = \mu E_x$) [46]. In particular, there appear multiple resonances in addition to the main resonance at $v_x = v_1$ predicted for the dc driving.

The dimple profile also depends on the orientation of the direction of WS motion with respect to the symmetry axes of the WS. For simplification, here we assume direction of WS motion to be parallel to the line connecting two nearest neighbors of the electron lattice. Despite some complications arising from ac-driving, etc., in general the maximum depth of the dimples is given by ξ_0 from Eq. (4.2). As shown in Fig. 1.13, the maximum horizontal reaction force from the surface deformation is proportional to ξ_0 , $F_{\text{DL,th}}^{(||)} \propto \xi_0$, thus is strongly affected by the phenomenological damping coefficient v_d . Therefore, by measuring the threshold driving force at the decoupling onset, the factors affecting damping of resonant riplons can be studied. In particular, we are interested to study effect of finite size of WS on damping of resonant riplons

4.2 Experiment

Two microchannel devices were used in the experiments described here. The first device, hereafter called Sample 1, was composed of two patterned gold layers separated

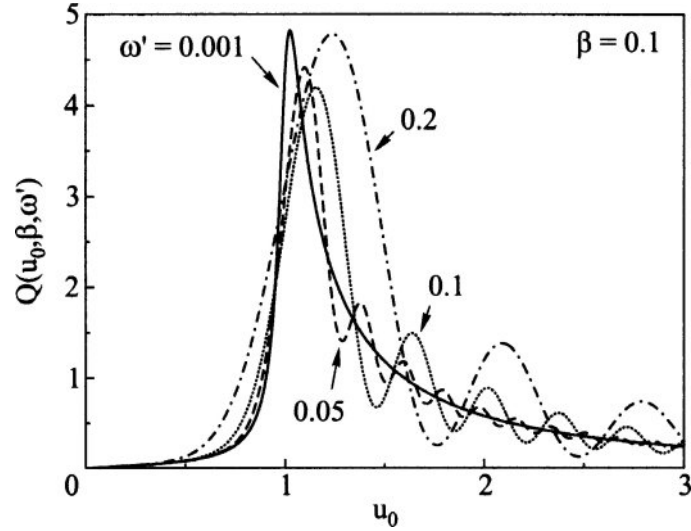


Figure 4.1: Field-velocity characteristic of the BC resonance under ac driving of WS. The dimensionless function $Q(u_0, \beta, \omega')$, which describes the field-velocity characteristic, versus the normalized drift velocity u_0 of the ac-driven WS. Curves are for several values of dimensionless ω' which is the ratio between the driving frequency and frequency of resonant ripples. Fixed parameter β characterizes the damping rate for resonant ripples. Figure is reproduced from [46].

by a insulating hard-baked photoresist layer with $1.6 \mu\text{m}$ in height, while the second device, Sample 2, was composed of same patterned gold layers but with the insulating silicon nitride layer with $1.5 \mu\text{m}$ in height. The bottom layer contains a left and right reservoir electrodes connected by a $215 \mu\text{m}$ long channel, which is formed with one $5 \mu\text{m}$, one $10 \mu\text{m}$, one $20 \mu\text{m}$, and two $90 \mu\text{m}$ long segments. The top layer contains a split-gate electrode and a guard electrode, by which the microchannels are defined (Fig. 4.2). Adjacent electrodes were separated by $1 \mu\text{m}$ gaps.

The transport of electrons through the microchannel device was measured by the Sommer-Tanner method as described in Ch. 2. An ac voltage V_{in} at the frequency f in the range $30 - 100 \text{ kHz}$ was applied to one of the reservoir electrodes, while both the in-phase and quadrature components of the current I_{out} induced by electron motion in the other reservoir's electrode was measured with a lock-in amplifier. The capacitance value C_0 for both samples are retrieved from the measured trajectory data by the method mentioned in Sect. 2.3. The values of C_0 are 2.04 pF and 6.82 pF for Sample 1 and 2, respectively. As mentioned in Sect. 2.3, the FEM-determined values of β for both samples are 0.77225 and 0.7875 . The current of electron in the center microchannel flows between reservoirs I_{ch} is further retrieved by the electrical lumped-circuit model as has been shown in Fig. 2.7 (b).

The WS of different length is created by applying a positive bias V_{tr} to a certain group of adjacent segments that comprise the center microchannel electrode, while keeping the rest of segments at a small positive potential V_L (typically $0.3 - 0.5 \text{ V}$). In this case, at sufficiently large V_{tr} we observed formation of WS of the effective length corresponding to the total length of the adjacent segments biased by the potential $V_{\text{tr}} = V_{\text{WS}}$, while electrons above the rest of the segments in the central channel were

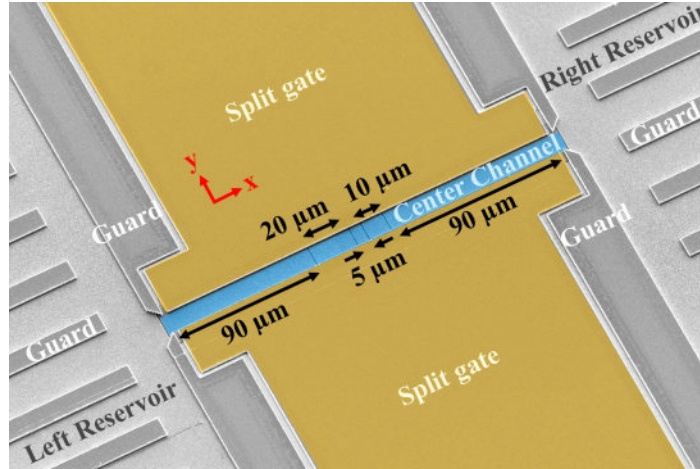


Figure 4.2: Microchannel device for study of finite-size effect. False-color scanning electron microscopic image of the microchannel device consisting of two reservoirs connected by a center channel of $215 \mu\text{m}$ in length and $10 \mu\text{m}$ in width. The bottom electrode of the center channel is segmented into pieces of different length as indicated in the figure.

in the liquid phase. Using a segmented channel electrode, shown in Fig. 4.2, we thus could create WS with effective lengths of $5, 10, 15, 20, 25, 35, 90, 100, 110, 115, 125,$ and $215 \mu\text{m}$. The results of measured IV -dependence for WS of different lengths by varying the amplitude of driving voltage V_{in} are presented in the following sections.

4.3 Results

Here we present 6 different data sets measured in Sample 1 (Fig. 4.3 and Fig. 4.4), and 5 data sets measured in Sample 2 (Fig. 4.5 and Fig. 4.6). The conditions for each measurement are as listed in the figures. The electron density of the WS $n_{e,\text{WS}}$ is estimated by solving Eq. (2.6) and Eq. (2.5) using the value of I_{BC} obtained from fitting experimental data with Eq. (2.7), as has been described in Sect. 2.3. The pressing electric field $E_{z,\text{WS}}$ exerted by the WS towards the liquid helium surface is the sum of the pressing electric field due to applied voltages and the pressing electric field due to the image charge in the liquid. The results for the amplitude and phase of current measured by the lock-in amplifier as a function of driving voltage V_{in} for different length of WS are shown in Fig. 4.3–Fig. 4.6. Both the BC plateau and the onset of sliding are observed for the WS when its length is at least $15 \mu\text{m}$. The threshold driving voltage at the onset of sliding steadily increases with the size of the WS and is maximal when WS occupies the whole channel (curve marked as WS $215 \mu\text{m}$). The red dashed line shows the fitting of the experimental data by Eq. (2.7) as described in Sect. 2.3.

In order to find the values for the threshold electric field $E_{s,\text{max}}$ at the onset of sliding for each length of WS, we used a simple model to account for the resistance of the microchannel filled with electrons in both solid and liquid phases. Such a model proved successful in explaining the main experimental features of the electron transport in a microchannel observed in the experiments discussed in the previous chapter [1]. In

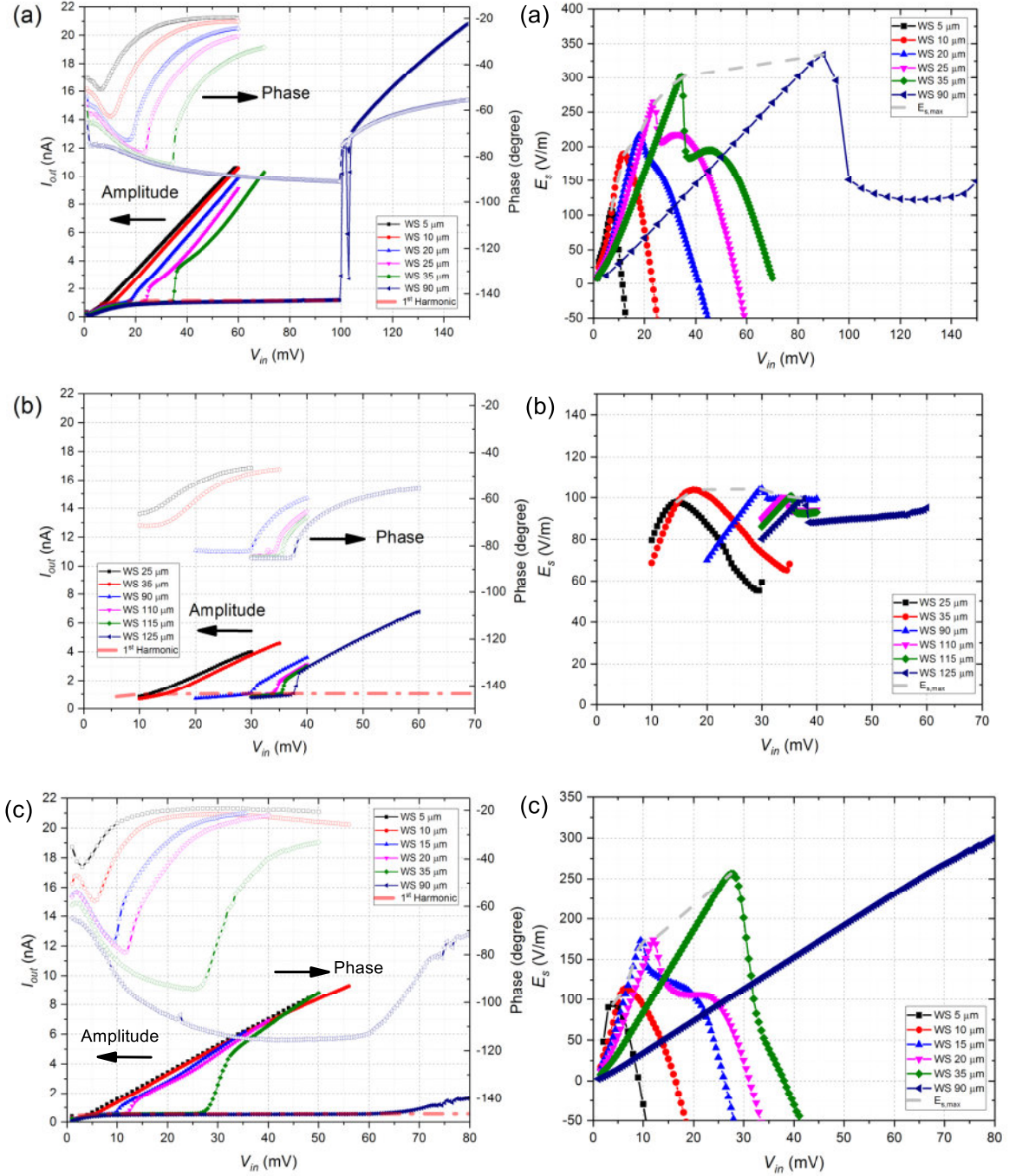


Figure 4.3: Data sets S1D1-S1D3 measured in Sample 1. Figures on the left side are the amplitude (the left axis) and the phase (the right axis) of the current measured by lock-in amplifier plotted as a function of driving voltage V_{in} . Data (a) are measured at $T = 0.88$ K and $n_e = 7.03 \times 10^{13} \text{ m}^{-2}$; data (b) are measured at $T = 1.08$ K and $n_e = 6.28 \times 10^{13} \text{ m}^{-2}$; data (c) are measured at $T = 0.58$ K and $n_e = 4.11 \times 10^{13} \text{ m}^{-2}$. The red dashed line is the fitting of experimental data by Eq. (2.7) as described in Sect. 2.3. The figures on the right side show the calculated electric field E_s across the WSs for each data plot on the left side. The maximum values of E_s at the onset of sliding for each data set are connected by a grey dashed line that serves as an eye guide.

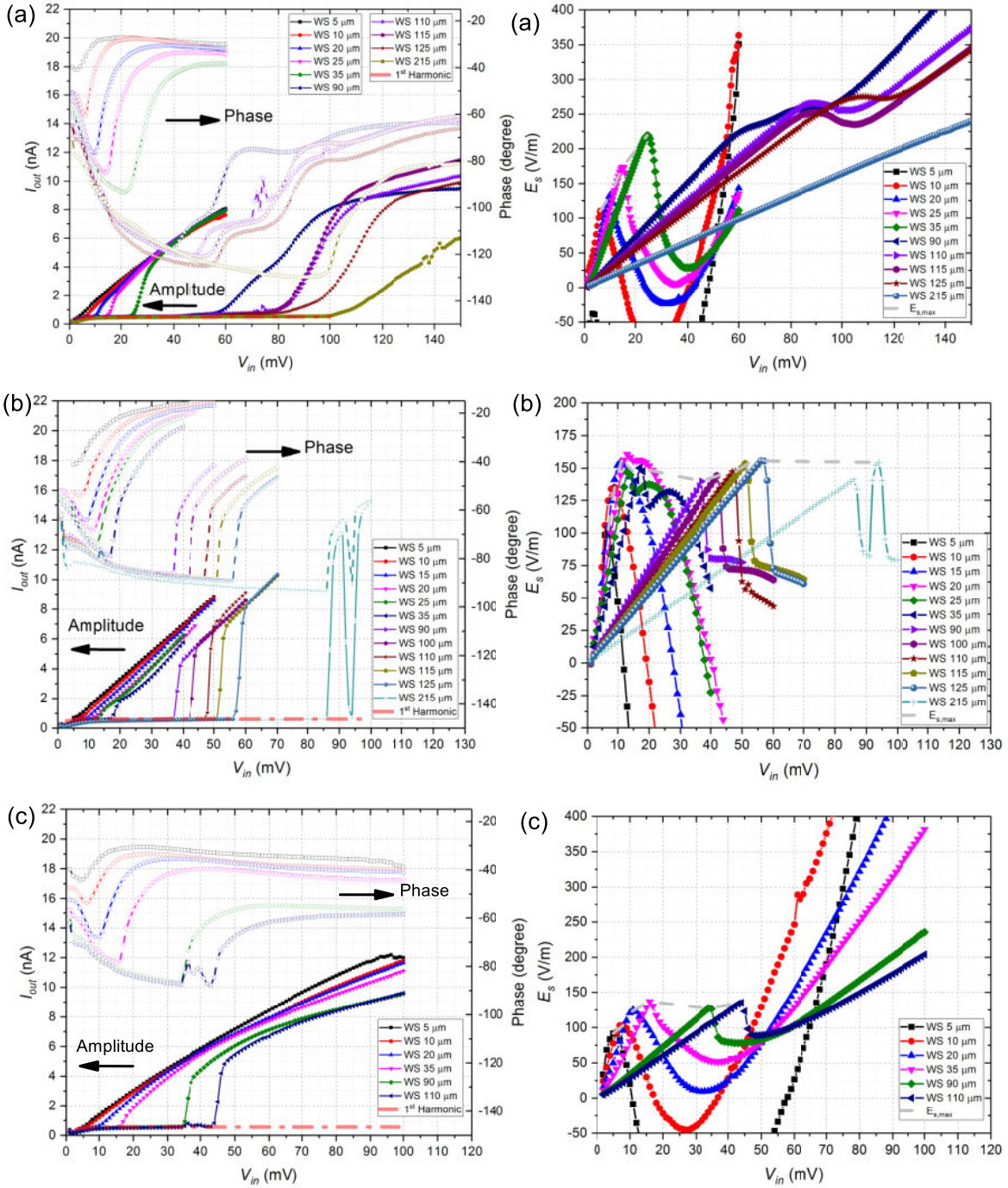


Figure 4.4: Data sets S1D4-S1D6 measured in Sample 1. Figures on the left side are the amplitude (the left axis) and the phase (the right axis) of the current measured by lock-in amplifier plotted as a function of driving voltage V_{in} . Data (a) are measured at $T = 0.58$ K and $n_e = 3.85 \times 10^{13} \text{ m}^{-2}$; data (b) are measured at $T = 0.88$ K and $n_e = 4.37 \times 10^{13} \text{ m}^{-2}$; data (c) are measured at $T = 0.88$ K and $n_e = 4.12 \times 10^{13} \text{ m}^{-2}$. The red dashed line is the fitting of experimental data by Eq. (2.7) as described in Sect. 2.3. The figures on the right side show the calculated electric field E_s across the WSs for each data plot on the left side. The maximum values of E_s at the onset of sliding for each data set are connected by a grey dashed line that serves as an eye guide.

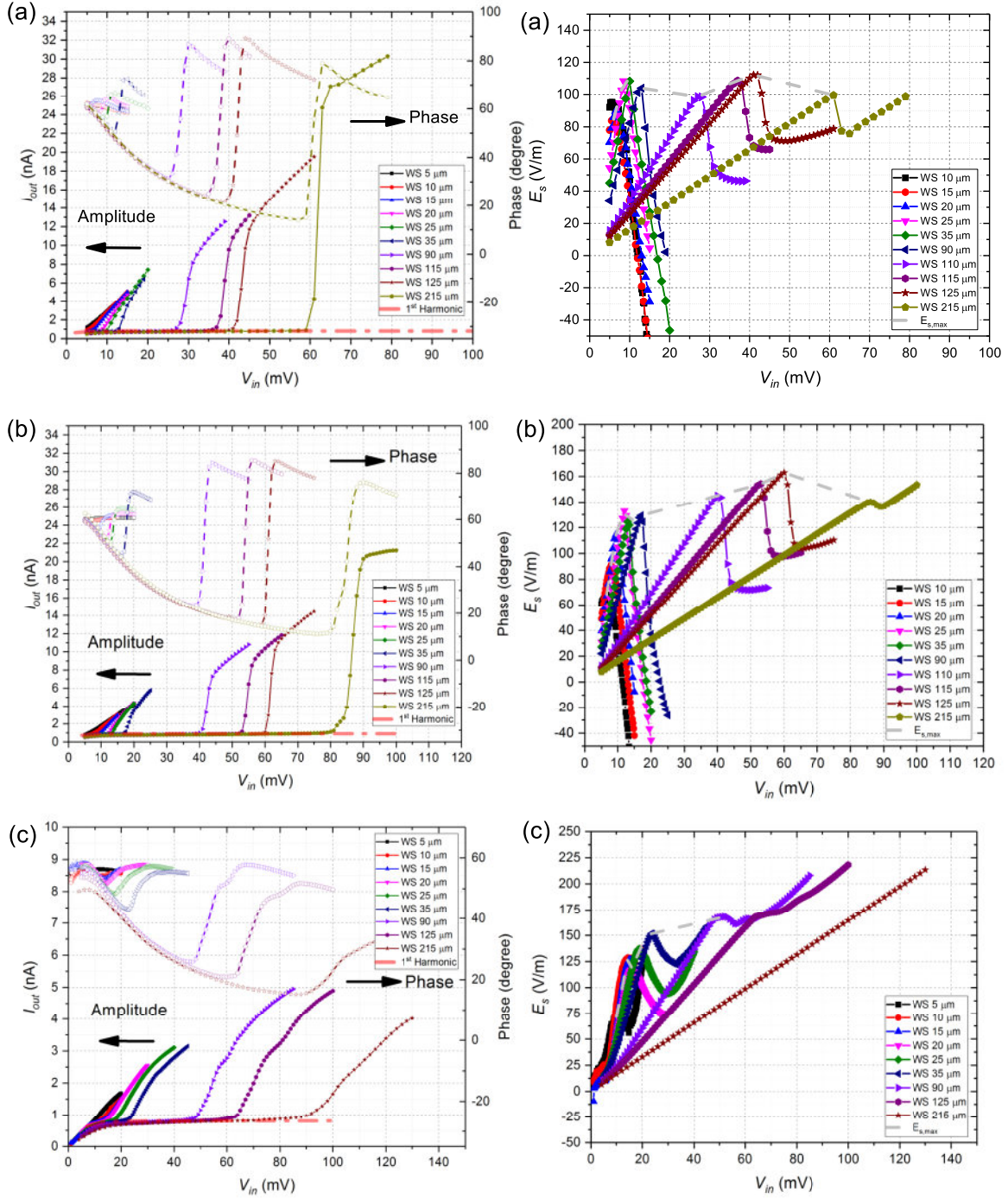


Figure 4.5: Data sets S2D1-S2D3 measured in Sample 2. Figures on the left side are the amplitude (the left axis) and the phase (the right axis) of the current measured by lock-in amplifier plotted as a function of driving voltage V_{in} . Data (a) are measured at $T = 0.91$ K and $n_e = 5.01 \times 10^{13} \text{ m}^{-2}$; data (b) are measured at $T = 0.91$ K and $n_e = 5.44 \times 10^{13} \text{ m}^{-2}$; data (c) are measured at $T = 0.91$ K and $n_e = 5.05 \times 10^{13} \text{ m}^{-2}$. The red dashed line is the fitting of experimental data by Eq. (2.7) as described in Sect. 2.3. The figures on the right side show the calculated electric field E_s across the WSs for each data plot on the left side. The maximum values of E_s at the onset of sliding for each data set are connected by a grey dashed line that serves as an eye guide.

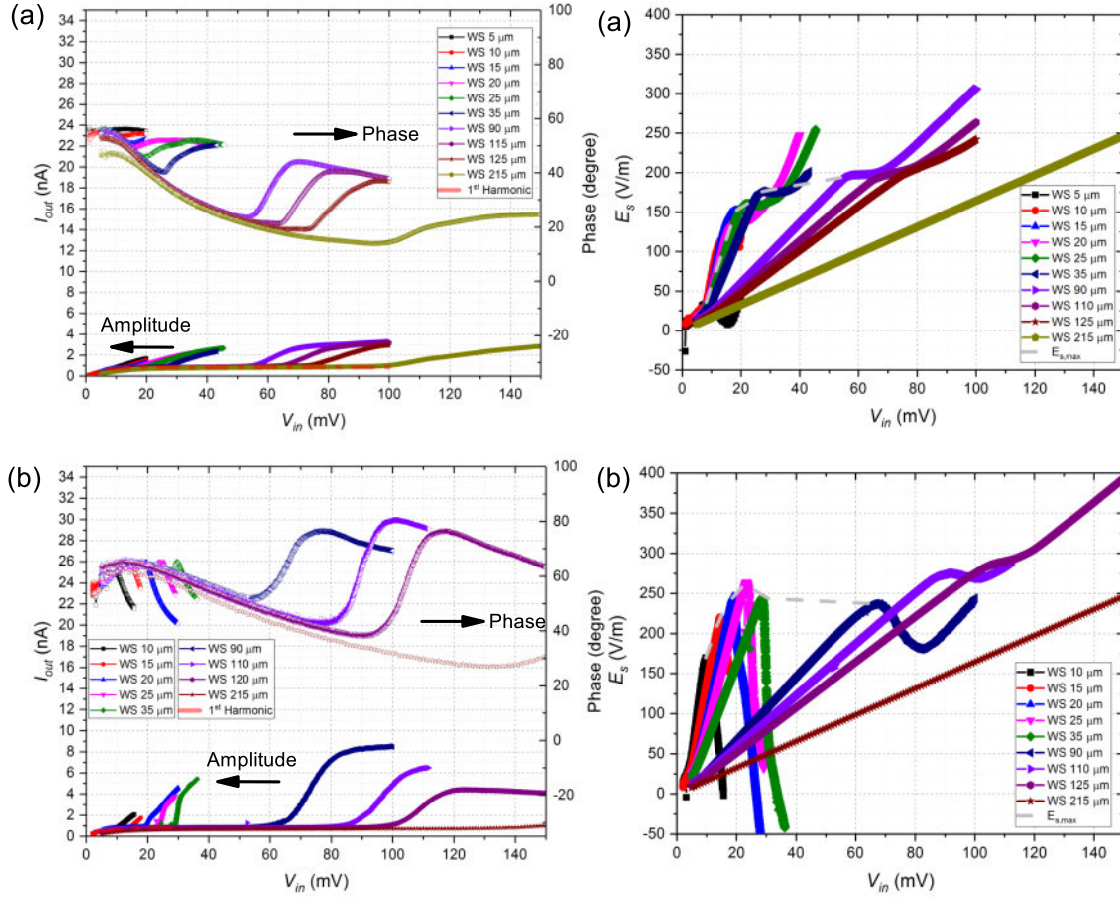


Figure 4.6: Data sets S1D4, S1D5 measured in Sample 2. Figures on the left side are the amplitude (the left axis) and the phase (the right axis) of the current measured by lock-in amplifier plotted as a function of driving voltage V_{in} . Data (a) are measured at $T = 0.89$ K and $n_e = 5.27 \times 10^{13} \text{ m}^{-2}$; data (b) are measured at $T = 0.88$ K, 30 kHz and $n_e = 5.24 \times 10^{13} \text{ m}^{-2}$. The red dashed line is the fitting of experimental data by Eq. (2.7) as described in Sect. 2.3. The figures on the right side show the calculated electric field E_s across the WSs for each data plot on the left side. The maximum values of E_s at the onset of sliding for each data set are connected by a grey dashed line that serves as an eye guide.

particular, we assume that the total resistance of the microchannel, R_{ch} , comes from the resistance of electrons in solid and liquid phase, R_{s} and R_{L} , respectively, which are connected in series, that is $R_{\text{ch}} = R_{\text{s}} + R_{\text{L}}$. The total resistance of the microchannel is found for a given value of the driving voltage V_{in} using the lumped-circuit model, as described in Sect. 2.3. Then the electric field across the WS can be estimated from the corresponding voltage drop $R_{\text{s}}I_{\text{ch}}$ according to

$$E_{\text{s}} = \frac{I_{\text{ch}}(R_{\text{ch}} - R_{\text{L}})}{L_{\text{tr}}}, \quad (4.4)$$

where I_{ch} is the current of electrons in the microchannel and L_{tr} is the length of the strongly-biased segmented electrodes, which determines the length of the WS. The resistance R_{L} is estimated as $R_{\text{L}} = R_{\text{LC}}(L_{\text{ch}} - L_{\text{tr}})/L_{\text{ch}}$, where $L_{\text{ch}} = 215 \mu\text{m}$ is the length of the microchannel and R_{LC} is the resistance of the microchannel when it is biased at V_{L} , entirely filled with electron liquid. Similar to R_{ch} , values of R_{LC} were found from the lumped-circuit analysis, too.

The calculated values of E_{s} of each data set in the left-hand side of Fig. 4.3–Fig. 4.6 are shown in the figures on the right-hand side, respectively. In the BC scattering region, E_{s} increases linearly with the driving voltage V_{in} until an abrupt reduction in E_{s} occurs at the onset of sliding. This determines the threshold electric field $E_{\text{s}}^{(\text{max})}$. Note that after sliding, the behavior of the measured I_{ch} and E_{s} becomes rather complicated. For some data sets, the sliding transition becomes hard to determine. This could be due to effects of ac-driving, as discussed in previous section, or other reasons. We did not analyse such data.

Values of the threshold electric field $E_{\text{s}}^{(\text{max})}$ at the onset of sliding extracted from data are plotted in Fig. 4.7 for different lengths of WS. It shows that the threshold electric field is essentially independent of the size of the WS, unless its length is shorter than about $25 \mu\text{m}$, while for WS of shorter length there is a significant decrease of $E_{\text{s,max}}$. A theoretical analysis of the observed results is given in the next section.

4.4 Discussion

The observed threshold driving electric field $E_{\text{s}}^{(\text{max})}$ shows a significant decrease at sufficiently small L_{WS} . Such a size-dependent behavior could be caused by different factors. One of the interesting possibilities is related to the structural order transition in WS due to the finite-size confinement, which has been demonstrated to be strongly dependent on the commensurability of WS lattice constant and the confinement geometry [47]. A reentrant solid-liquid-solid transition is the feature of this KT-type melting of a WS under the condition of varying commensurability with respect to the WS confinement in the direction normal to the transport direction. This type of behavior will be discussed in the next chapter. Here, we attribute the observed finite-size effect to the loss of resonant ripplons through WS boundary.

To account for the observed finite-size effect, we follow Vinen's classical model and consider an essentially one dimensional model of finite size electron lattice of length L and periodicity a moving along the microchannel at velocity v_x . The force exerted by

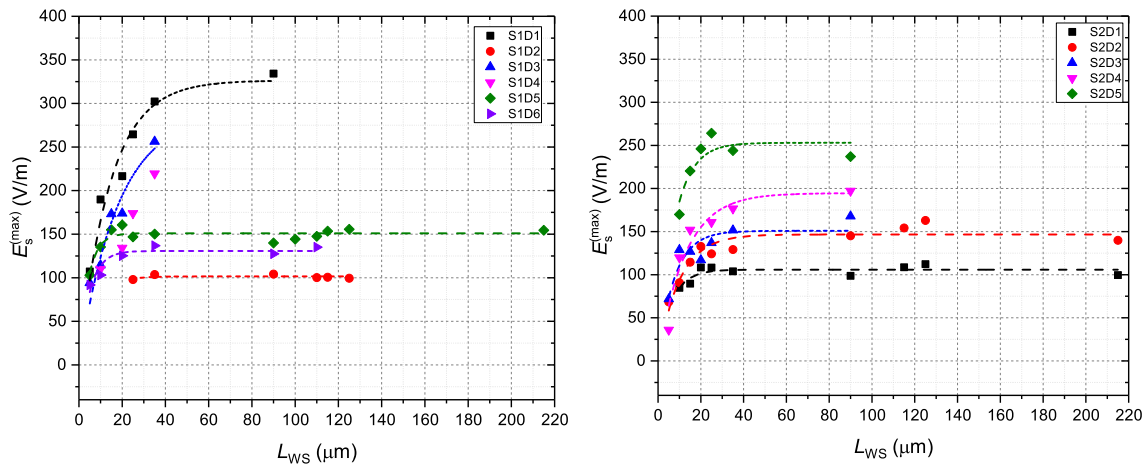


Figure 4.7: Threshold electric field $E_s^{(\max)}$ at the onset of WS sliding plotted as a function of WS length. The values of $E_s^{(\max)}$ are extracted from data taken using Sample 1 (left panel) and Sample 2 (right panel) using data set shown in Fig. 4.3–Fig. 4.6. The dashed line is the fitting line using expression $E_s^{(\max)} = E_0(1 - \exp(-L/L_{WS}))$, see explanation in the text in Sect. 4.4.

electrons on the liquid surface per unit length is given by

$$f(x, t) = eE_{\perp} \sum_{n=0}^N \delta(x - X_n - v_x t), \quad (4.5)$$

where $N = L/a$ and $X_n = an$ is the average x -coordinate of electrons at $t = 0$. We assume that the force was averaged over the fast thermal motion of electrons, thus the pressing field E_{\perp} was appropriately corrected by the Debye-Waller factor [7]. To proceed further it is convenient to write the Fourier expansion of $f(x, t)$ over one-dimensional wave vectors q . This can be easily done by representing the above expression for $f(x, t)$ as a product of an infinite train of delta-functions $\delta(x - X_n - v_x t)$, $-\infty < n < +\infty$, and a pulse function $\pi(x) = \Xi(L/2 + x) - \Xi(L/2 - x)$, where $\Xi(x)$ is the Heaviside step function. This results in

$$f(x, t) = \frac{NeE_{\perp}}{\pi} \sum_{m=-\infty}^{\infty} \int_{-\infty}^{\infty} e^{i(qx - m\Omega t)} \frac{\sin [L(q - mG_1)/2]}{L(q - mG_1)} dq, \quad (4.6)$$

where G_1 is the first reciprocal lattice vector and $\Omega = v_x G_1$. Similar to Vinen, we consider distortion of the liquid helium surface only due to the term $m = 1$ in the above expansion, which is expected to give resonant excitation of ripples with the wave vector G_1 when the electrons velocity v_x approaches the ripplon phase velocity $v_1 = \sqrt{\alpha G_1 / \rho}$. Higher harmonics in the expansion will give resonances at higher velocities, therefore can be neglected. Using the Laplace equation of the free surface waves, Eq. (4.1), and replacing the pressure on the surface from the electron lattice with the relation $p = f(x, t)/w$, the resulted amplitude of the surface distortion in

z -direction ς is

$$\xi(x, t) = \frac{2NeE_{\perp}}{\pi\rho w} \int_{-\infty}^{\infty} \frac{qe^{i(qx-\Omega t)}}{\Omega^2 - \omega_q^2 + i\gamma_q\Omega} \frac{\sin(L(q - G_1)/2)}{L(q - G_1)} dq. \quad (4.7)$$

The real part of the above equation represents the amplitude of the liquid surface deformation caused by the propagating electron lattice. Following Vinen, we introduced a phenomenological damping rate γ_q that accounts for natural damping of ripples with the wave vector q due to internal losses of energy in the liquid. Note that due to damping the propagating periodic surface deformation described by the above equation has a phase lag with respect to the propagating electron lattice, that is the positions of the minima of surface distortion do not coincide with the positions of electron lattice sites. As a result, the reaction force exerted on electrons normal to the liquid surface has a horizontal component which results in the friction force F exerted on the electron system in the direction opposite to their motion, see Fig. 1.13 in Ch. 1. This force can be found by equating the normal component of the reaction force to eE_{\perp} , from which we obtain $F = eE_{\perp} (\partial\xi/\partial x)_{x=x_t}$, where the slope of the liquid surface in the above equation is evaluated at $x_t = \Omega t/G_1$. Plugging the real part of Eq. (4.7) into the above expression and considering the relevant wave numbers q close to G_1 , the maximum force F obtained at $v_x = v_1$ can be found in the analytical form

$$F_{\max} = \frac{n_s e^2 E_{\perp}^2}{\rho v_d v_1} \left[1 - \exp\left(-\frac{\gamma_{G_1} L}{2v_1}\right) \right], \quad (4.8)$$

where we introduced notation for the damping coefficient $v_d = \gamma_{G_1}/G_1 \approx \gamma_q/q$ which was used by Vinen. The above equation gives the maximum friction force on the electron lattice that can be provided by surface dimples. In the BC scattering regime ($v_x \approx v_1$), this force equilibrates the driving force on electrons due to applied electric field in x -direction. Thus, the maximum force given by the above equation determines the threshold electric field E_{th} discussed in Sect. 1.5. Note that at $L \rightarrow \infty$ the Eq. (4.8) recovers the Vinen's result given by Eq. (4.3) in Sect. 4.1. More interestingly, as the length of electron lattice L decreases and becomes close to $2(v_1/\gamma_{G_1})$ the maximum force, therefore the threshold electric field E_{th} , also decreases. This is in agreement with our experimental observation described in the previous section. The decrease of the maximum friction force with decreasing effective size of the electron lattice has a simple physical meaning. The quantity v_1/γ_{G_1} represents the typical propagation length of ripples with the wave vector G_1 due to internal energy losses in the liquid. As long as this length is much shorter than the length of the electron lattice L , the damping of resonant ripples do not depend on the system size. On the other hand, when the propagation length becomes longer than L , contribution to the loss of resonant ripples via their escape from the area occupied by the electron lattice becomes significant. This leads to the diminishing of dimples, therefore decrease of the threshold electric field E_{th} , which is in agreement with our experiment data shown in Fig. 4.7. The dashed lines are fitting curves using Eq. 4.8 in the form $F_{\max} = E_0 \left[1 - \exp\left(-\frac{L}{L_{\text{WS}}}\right) \right]$, where E_0 and $L_{\text{WS}} = 2v_1/\gamma_{G_1}$ are adjustable parameters. From L_{WS} the damping rate γ_{G_1} could be estimated.

The estimated damping rate of ripples is about 10^6 s^{-1} . The damping of micron-wavelength capillary waves on superfluid ^4He was experimentally studied by Roche *et al.* using an interdigital capacitor setup [48]. The authors concluded that the main contribution to damping of such ripples comes from the ripple-phonon interaction and provided a theoretical expression for γ_q [49]

$$\gamma_q = \frac{\pi^2 \hbar}{90 \rho} \left(\frac{k_B T}{\hbar s} \right)^4 q, \quad (4.9)$$

where s is the first sound velocity in liquid ^4He . Using this expression, we obtain $\gamma_{G_1} = 3 \times 10^5 \text{ s}^{-1}$ for $T = 0.88 \text{ K}$ and $G_1 = 5 \times 10^7 \text{ m}^{-1}$. This is in very satisfactory agreement with our order-of-magnitude estimate $\gamma_{G_1} = 10^6 \text{ s}^{-1}$ considering extreme simplicity of our model and that the theoretical formula by Roche *et al.* underestimates the experimentally measured attenuation coefficient at temperatures above 0.7 K [48, 49].

4.5 Summary

We have studied the non-linear transport of WS coupled to a commensurate deformation on the surface of liquid helium. In particular, we employed a microchannel device that allowed us to vary the effective size of the electron crystal and study its transport in a microchannel geometry. We observed dependence of the sliding threshold of driving electric field, therefore the maximum friction force exerted on the electron crystal from the liquid substrate, on the crystal size. In particular, we found that the friction force significantly decreases when the crystal length is shorter than about $25 \mu\text{m}$. We explain this effect by weakening of the surface deformation due to radiative losses of ripples coherently emitted by the driven electron lattice of finite size. To account quantitatively for the observed effect, we employed a simple hydrodynamic model that allowed us to estimate the natural dumping of ripples due to internal energy losses in the liquid. In particular, we found a good agreement of our result with predicted dumping of ripples due to their interaction with bulk excitations in liquid helium. This indicates that our experimental method can be viable for studies of not only the transport of electron systems on liquid substrates but also interaction between surface and bulk excitations in superfluid helium.

Chapter 5

WS in microchannel subject to spatial periodic potential

The experiments described in two previous chapters demonstrated that satisfactory control of SSEs confined in a microchannel can be achieved by imposing an electrostatic potential whose profile can be designed by a proper micro-electrode structure. In this chapter, we describe experiments where we studied transport of WS in a microchannel subjected to a spatially periodic potential. The long-term motivation to our work comes from the possibility to use SSE system as a simulator of the Frenkel-Kontorova (FK) model.

5.1 Frenkel-Kontorova model

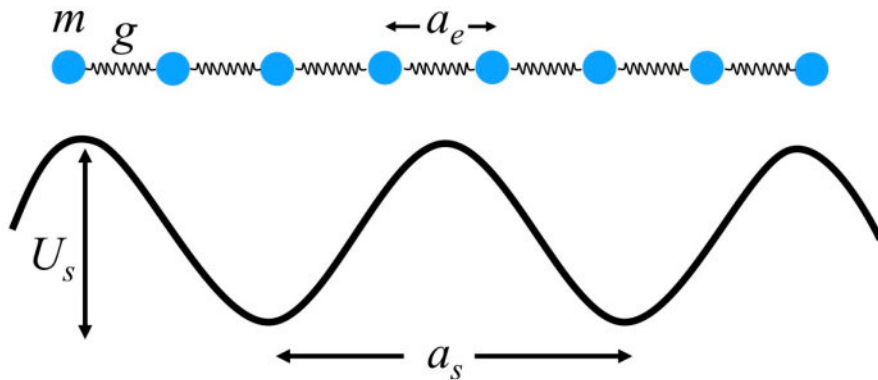


Figure 5.1: FK model. Schematic presentation of the Frenkel-Kontorova model: A chain of particles interacting via harmonic springs with elastic coupling g is subjected of an external periodic potential with period a_s .

FK model is a simple model that describes the dynamics of a chain of particles harmonically coupled with their nearest neighbors and subjected to a periodic substrate potential, as shown in Fig. 5.1. The corresponding classical Hamiltonian can be

expressed in the form

$$H = \sum_{n=-\infty}^{\infty} \left[\frac{m}{2} \left(\frac{dx_n}{dt} \right)^2 + \frac{1}{2} g (x_n - x_{n-1} - a_e)^2 + \frac{U_s}{2} \cos \left(\frac{2\pi}{a_s} x_n \right) \right], \quad (5.1)$$

where m is the particle mass, x_n is the coordinate of the n -th particle in the chain, U_s and a_s are the depth and period of the external on-site periodic potential, g is the elastic constant of the harmonic coupling string, and a_e is the equilibrium distance between particles in the absence of the on-site potential. In the continuum limit approximation, the standard FK model reduces to the integrable sine-Gordon (SG) equation

$$\frac{\partial^2 u}{\partial t^2} - \frac{\partial^2 u}{\partial x^2} + \sin u = 0, \quad (5.2)$$

where u is the particle displacement defined by the relation $x_n = na_s + u_n$ in the continuum limit approximation. SG equation allows exact solutions for different types of elementary excitations, such as phonons, kinks (topological solitons) and breathers (dynamical solitons). The general behavior of traditional FK model, therefore, can be determined by the dynamics of these three elementary excitations. In spite of the simplicity of FK model itself and further approximations resulting in SG equation, it was shown that FK model can provide deep physical insight into the nonlinear transport phenomena such as the dynamics of charge-density waves [50], competing interactions of different periodicities in adsorbed atomic layers [51], commensurate-incommensurate phase transition in dielectrics [52], dynamics of disordered Wigner crystals in 2D heterostructure [53], models of interfacial slip [54], etc. Note that the real physical systems mentioned above are mostly two dimensional, while only simplified one dimensional FK model has been studied. Further studies of FK model in higher dimensions are impeded by the inherent difficulty of describing a strongly correlated system theoretically.

The idea of quantum simulator realized in a highly pure, controllable physical system have been proposed for testing several standard non-trivial models of strongly correlated systems such as the Hubbard model [3], FK model [4], etc. So far, the only experimental system extensively exploited is the system of cold trapped ions. The system of electrons floating above liquid helium possesses high purity such that its solid phase, the Wigner solid, shows a promising potential for studying FK model. Here we propose to employ the WS on the surface of liquid helium as a 2D particle lattice, and introduce an external electrostatic periodic potential as the periodic substrate potential for FK model simulation. The transport of WS along microchannel can be studied, and the FK model driven dynamics can be characterized by the measured current as a function of the strength of applied periodic electrostatic potential. Here we report our preliminary studies of the transport of WS in a microchannel subject to a spatially periodic (period 1 μm) potential along the channel.

5.2 Experiment

As in our previous experiments, the microchannel device used in this study consisted of two reservoirs and a central channel. The microscopic image of the device is shown in Fig. 5.2 (a). The device is composed of two layers of gold electrodes which can be distinguished by the colors in Fig. 5.2 (a). The darker golden pattern is the bottom layer while the lighter one is the top layer. The bottom layer contains two reservoirs (left and right) and a pair of finger-like electrodes, also known as the inter-digital capacitor (IDC), which form the center channel electrode, as shown in Fig. 5.2 (c). The top layer contains the usual guard electrode and split gate electrode as described in Ch. 2. The depth of the central microchannel is $0.55 \mu\text{m}$ determined by the thickness of an insulating silicon nitride layer separating two gold layers. Each reservoir consists of 51 rows of $5 \mu\text{m}$ -wide and $700 \mu\text{m}$ -long channels to provide large area for storing SSEs. The central channel was $5 \mu\text{m}$ -wide and $101 \mu\text{m}$ -long.

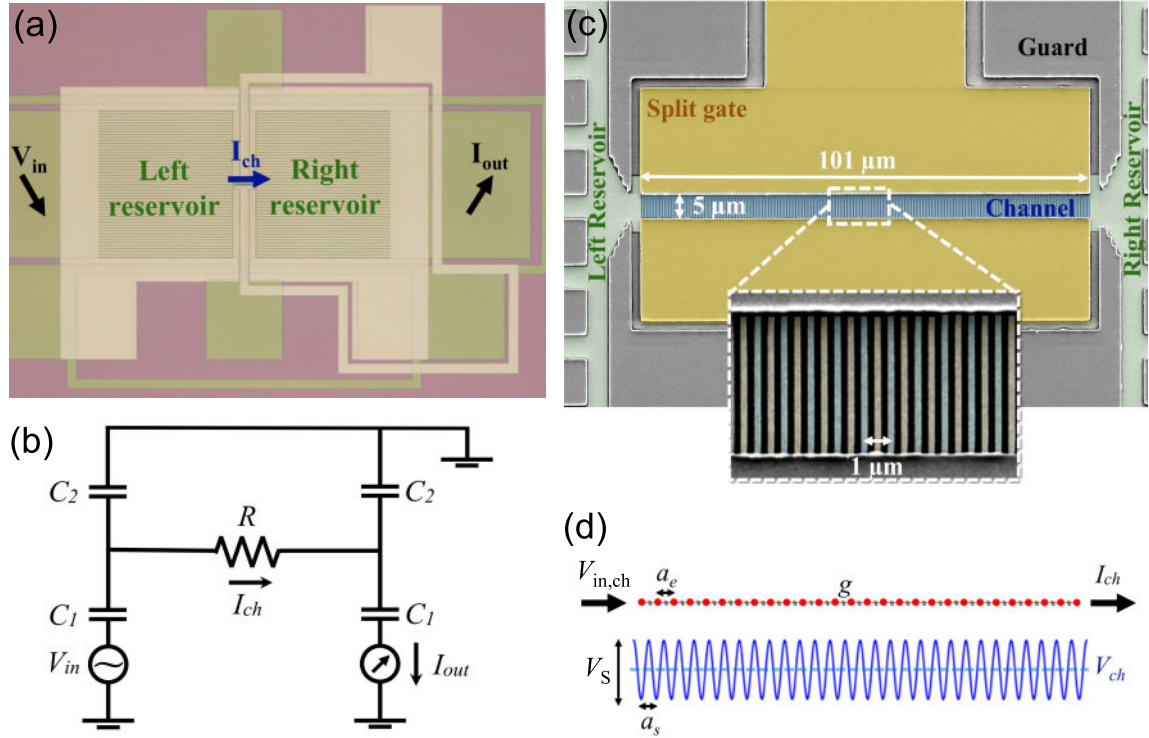


Figure 5.2: Microchannel device of ac driven FK model study. (a) Microscopic image of the microchannel device. (b) The electrical lumped-circuit model. (c) False-color scanning electron microscopic image of the area of center channel. (d) Schematic drawing of the external periodic potential defined by the bottom finger-like electrodes (blue curve), and the chain of particles represented by WS (red dots).

The IDC structure of the bottom channel electrode was fabricated by EBL method. Each finger of IDC was 250 nm -wide, and the distance between the adjacent finger was also 250 nm . By applying voltage difference ΔV_F between two electrodes of IDC, an external periodic potential along the channel with spatial periodicity of $1 \mu\text{m}$ could be introduced. The amplitude of the external periodic potential at the liquid surface V_S

is controlled by the voltage difference ΔV_F . The current of SSEs flowing through the center channel I_{ch} is measured by the Sommer-Tanner method at driving frequency 99.5 kHz as described in Ch. 2. As discussed in Sect. 2.3, the capacitance value $C_0 = 2.05$ pF was found from the measured trajectory data by fitting them with lumped-circuit model, see Fig. 5.2 (b). The FEM-determined value of β was 0.844.

5.3 Results

5.3.1 Phase diagram of electron system without applying periodic potential

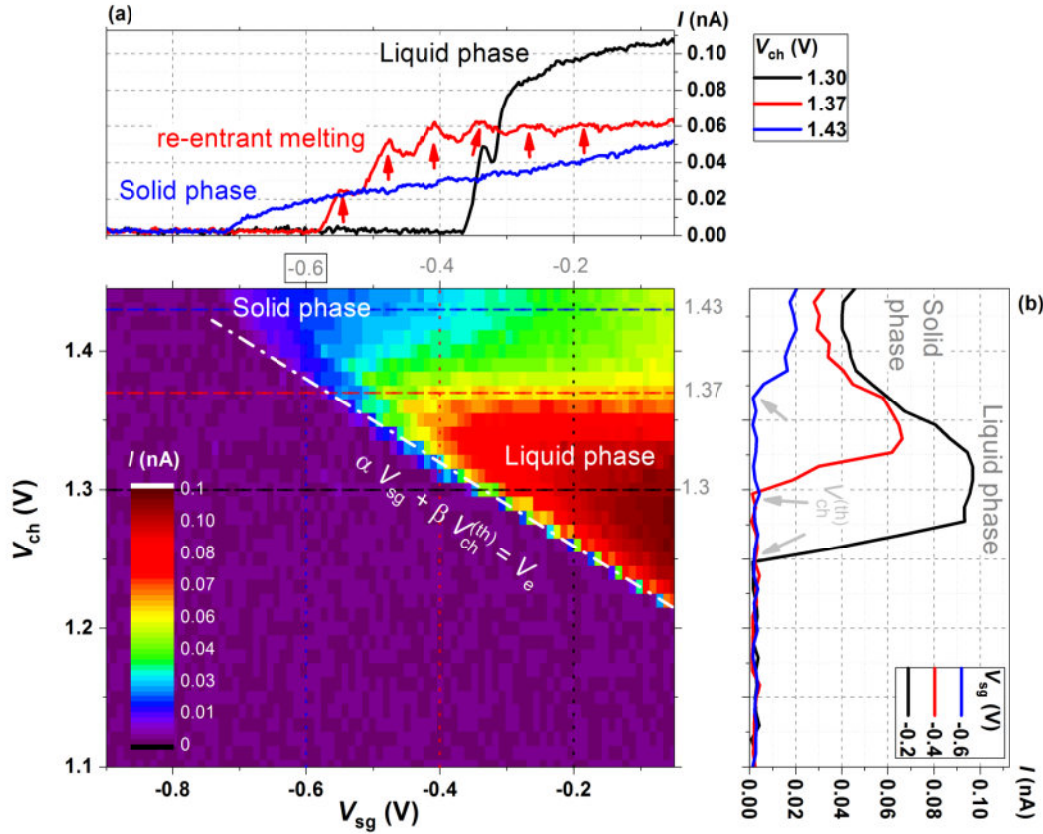


Figure 5.3: Measured current I_{out} in the device versus split-gate electrode potential V_{sg} and channel potential $V_{ch} = V_{ch1} = V_{ch2}$. Magnitude of electron current I_{out} measured at $T = 0.86$ K and $f = 99.5$ kHz. Dashed (white) line shows potential threshold values for channel opening, as described in the text. (a) I_{out} - V_{sg} curves for different values of channel potential V_{ch} as indicated. (b) I_{out} - V_{ch} curves for different values of split-gate electrode voltage V_{sg} as indicated

First, we check performance of the fabricated device by applying the same potential to both finger-like electrodes F1 and F2 of the central microchannel, $V_{ch} = V_{F1} = V_{F2}$, and measuring current in the device I_{out} while applying the peak-to-peak ac voltage $V_{in} = 5$ mV to the device. The absolute value of measured I_{out} is plotted in Fig. 5.3

for various values of V_{ch} and bias V_{sg} applied to the split-gate electrode of the central microchannel. To understand this diagram, it is convenient to use the simplified capacitance model described in Sect. 2.2. The potential at the uncharged liquid surface can be written as $V_s = \alpha V_{\text{sg}} + \beta V_{\text{ch}}$. When the electron potential V_e is smaller than V_s , the channel is closed such that no current can be detected. The zero current in the central microchannel corresponds to the condition $\alpha V_{\text{sg}} + \beta V_{\text{ch}} = V_e$, which determines the threshold value of the channel voltage for a given values of V_{sg} and V_e

$$V_{\text{ch}}^{(\text{th})} = \frac{1}{\beta} V_e - \frac{1 - \beta}{\beta} V_{\text{sg}}. \quad (5.3)$$

Below this threshold value, the potential at the uncharged surface in the central microchannel V_s is lower than V_e , therefore the central microchannel is completely depleted of electrons and the current I_{out} in the device is zero. The experimental values of $V_{\text{ch}}^{(\text{th})}$ are plotted in Fig. 5.3 by a dashed (white) line. By fitting this line using Eq. (5.3) we obtain $V_e = 0.92$ V and $\beta = 0.77$ (therefore $\alpha = 0.23$).

Above the threshold line in the V_{sg} - V_{ch} plane, the current in the device is determined by the resistance R of electrons in the microchannel, which in turn depends on the phase of the electron system, see Fig. 5.3 (a) and (b). For weak confinement of the electron system, which corresponds to lower values of V_{ch} and more positive values of V_{sg} , the system is in the liquid phase. This corresponds to low resistance R and large current I_{out} . For stronger confinement of the electron system, which corresponds to larger values of V_{ch} and more negative values of V_{sg} , the system undergoes crystallization into WS [38, 47]. As a result, the resistance R of electrons in the central microchannel increases due to formation of the commensurate dimple lattice, and the measured current I_{out} significantly drops. A spectacular behaviour is observed in the intermediate range of voltages, where current I_{out} oscillates with V_{sg} value, see Fig. 5.3 (a). This phenomenon was identified with the re-entrant melting of WS [39, 40]. As confining potential, therefore the width of the electron system in the microchannel, is varied by varying voltages applied to the electrodes, the WS in the microchannel undergoes intermittent melting as a result of increased fluctuations of position of electrons between stable configurations corresponding to different number of electron rows across the channel. Therefore, the oscillations in Fig. 5.3 (a) can be identified with different number of electron rows in the microchannel. The re-entrant melting, which results from the competition between stable configurations corresponding to different numbers of electron rows, is particularly important in studies of confined crystalline systems where the spatial order of particles is strongly affected by their confinement [47]. The interplay between the electron lattice configuration and confining potential is an interesting problem of structural phase transitions [55].

5.3.2 Effect of periodic potential

Next, we study effect of periodic potential by applying voltages $V_{\text{F1}} = V_{\text{ch}} + \Delta V_{\text{F}}/2$ and $V_{\text{F2}} = V_{\text{ch}} - \Delta V_{\text{F}}/2$. The measured current I_{out} against the amplitude of periodic potential and the driving voltage V_{in} is plotted in Fig. 5.4. At $\Delta V_{\text{F}} = 0$, the I - V curve demonstrates a clear BC scattering plateau and the sliding transition. The retrieved

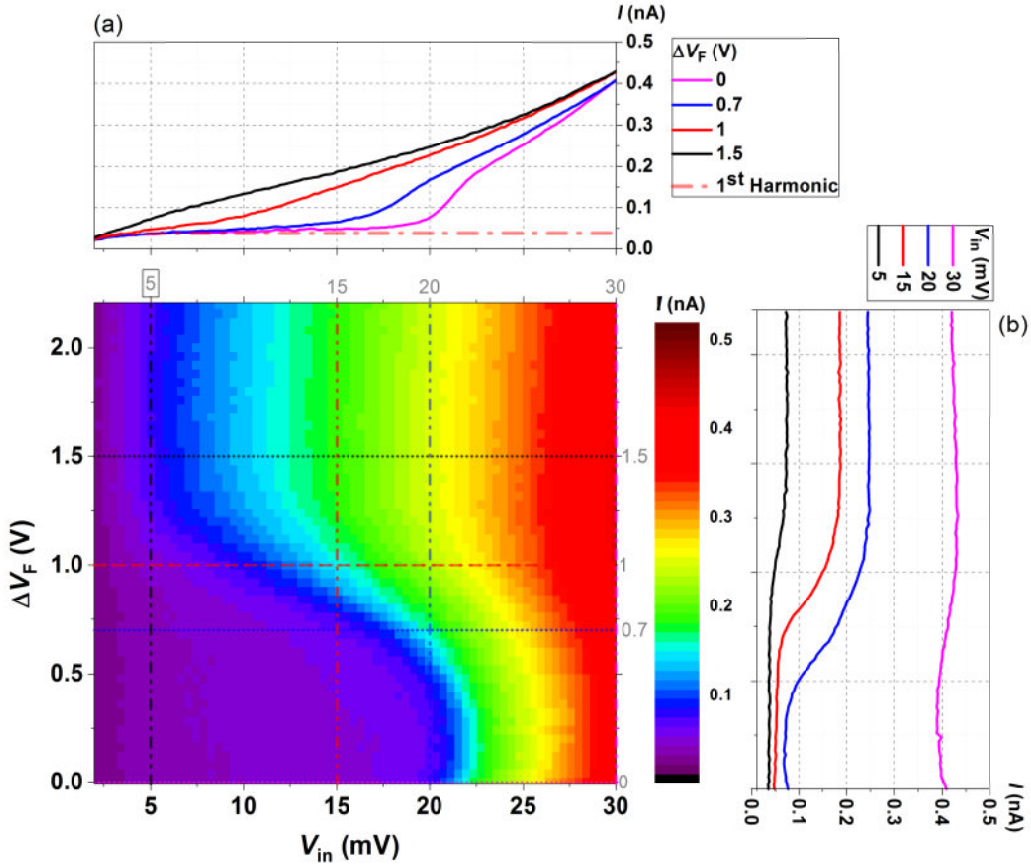


Figure 5.4: Measured electron current I_{out} versus driving ac voltage V_{in} and potential difference ΔV_F applied to the IDC electrodes. Magnitude of electron current I_{out} measured at $T = 0.86$ K for split-gate electrode potential $V_{sg} = -0.25$ V and the common bias for both channel electrodes $V_{ch} = 1.55$ V. (a) I_{out} - V_{in} curves for different values of periodic-potential depth ΔV_F as indicated. (b) I_{out} - ΔV_F curves for different values of driving ac voltage V_{in} as indicated.

electron density n_e from the procedure described in Sect. 2.3 is $1.1 \times 10^{13} \text{ m}^{-2}$ and the effective WS width is $2.8 \mu\text{m}$. For a triangular lattice, the relationship between n_e and the lattice constant is $a_e = \sqrt{2}/(3^{1/4} \sqrt{n_e})$. Therefore, for $n_e = 1.1 \times 10^{13} \text{ m}^{-2}$, it corresponds to a WS of lattice constant $a_e = 0.32 \mu\text{m}$. The estimation of number of rows N_y and columns N_x of a WS depends on the lattice orientation. Here we let the number of rows N_y equals to $N_y = w/(\sqrt{3}/2 \times a_e) + 1$, where $(\sqrt{3}/2 \times a_e)$ is the height of a triangle lattice of lattice constant a_e . We got $N_y \approx 11$ rows. For the finger-like electrodes of fixed period a_s of $1 \mu\text{m}$, $N_x = a_s/a_e + 1 \approx 4$. Thus, the commensurability between WS lattice constant a_e and substrate period a_s is about 4, i.e. about four electrons per substrate period.

A prominent feature observed in Fig. 5.4 (a) is suppression of the BC scattering plateau with increasing depth of periodic potential ΔV_F . One possible explanation of

ⁱThe fitted value $\beta = 0.77$ from Fig. 5.3 is close to the FEM simulated value $\beta = 0.844$, and the difference in the estimated n_e value by Eq. (2.5) is less than $0.05 \times 10^{13} \text{ m}^{-2}$.

this result is suppression of constructive interference of resonant riplons emitted by the electron lattice with spatially modulated lattice constant, due to imposed periodic potential, see Fig. 5.5. Another possible explanation is that the application of sufficiently strong periodic potential suppresses crystallization of the electron system into the long-range ordered WS phase [56].

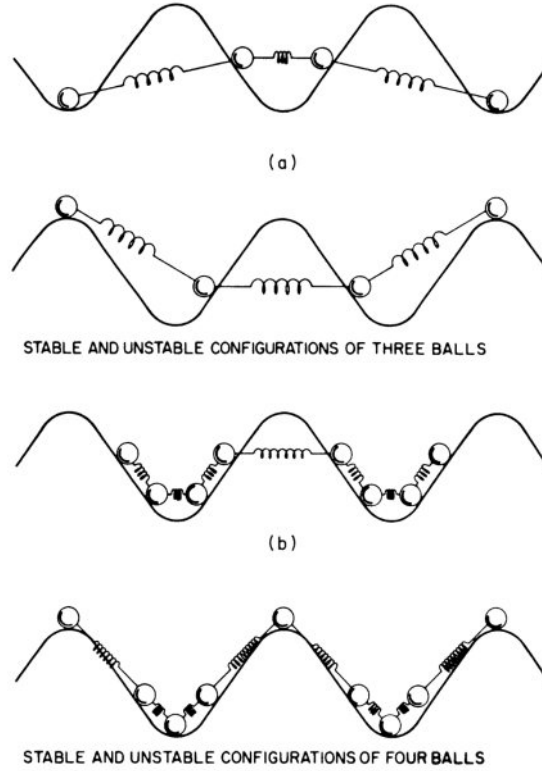


Figure 5.5: Ground state of odd/even number of particles in one period. (a) Stable and unstable configurations of three particles (typical of an odd number of particles). (b) Stable and unstable configurations of four particles (typical of an even number of particles). In both cases, the stable configuration does not have a particle at the top of a well. Figure is reproduced from [57].

Fig. 5.6 shows the measured electron current I_{out} against ΔV_F and split-gate potential V_{sg} under the conditions of $V_{\text{ch}} = 1.5$ V and $V_{\text{in}} = 5$ mV. At $\Delta V_F = 0$, the $I_{\text{out}}-V_{\text{sg}}$ curve demonstrates oscillations of I_{out} with V_{sg} , see the black curve of Fig. 5.6 (a). This oscillations are due to re-entrant melting of WS as mentioned in Sect. 5.3.1. For $\Delta V_F > 0.5$ V, the oscillation decreases and then totally disappears. This suggests that the application of sufficiently strong periodic potential suppresses crystallization of SSEs and formation of WS.

To understand effects of the spatially periodic potential on the electron system it is instructive to estimate the variation of the electron density n_e in the central microchannel using the parallel-plate capacitance approximation. As described in Sect. 2.2, the electron density can be estimated by Eq. (2.1). We find that at the middle of the channel the density varies nearly sinusoidally with average value \bar{n}_e and amplitude Δn_e . In particular, for $V_e = 0.92$ V, $V_{\text{sg}} = -0.8$ V, $V_{\text{ch}} = 1.5$ V, and $\Delta V_F = 0.7$ V using

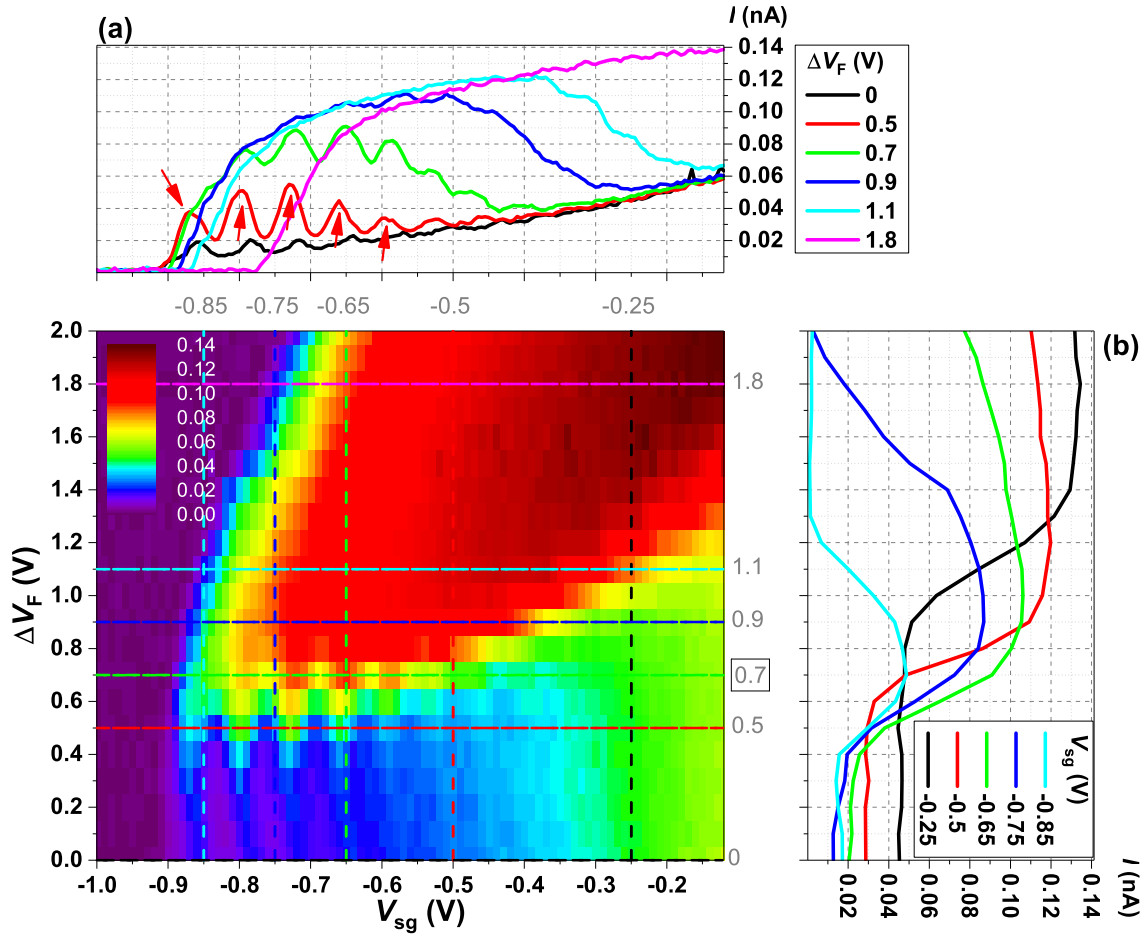


Figure 5.6: Measured electron current I_{out} versus split-gate potential V_{sg} and potential difference ΔV_{F} applied to the IDC electrodes. Magnitude of electron current I_{out} measured at $T = 0.86$ K for driving ac voltage $V_{\text{in}} = 5$ mV as a function of split-gate electrode potential V_{sg} for different values of potential different $\Delta V_{\text{F}} = |V_{\text{F1}} - V_{\text{F2}}|$ between channel electrodes. The common bias for two channel electrodes is fixed at $V_{\text{ch}} = 1.5$ V. (a) $I_{\text{out}}-V_{\text{sg}}$ curves for different values of periodic-potential depth ΔV_{F} as indicated. (b) $I_{\text{out}}-\Delta V_{\text{F}}$ curves for different values of split-gate voltage V_{sg} as indicated.

the above approximation we estimate $\bar{n}_e = 3.0 \times 10^{13} \text{ m}^{-2}$ and $\Delta n_e = 0.2 \times 10^{13} \text{ m}^{-2}$. For an infinite 2D electron system, the melting of WS is expected to happen when the value of plasma parameter $\Gamma = e^2 \sqrt{\pi \bar{n}_e} / (4\pi \epsilon_0 \epsilon k_B T)$ exceeds 130 ± 10 . For $T = 0.86 \text{ K}$, the critical density of electrons corresponds to $n_e = 1.4 \times 10^{13} \text{ m}^{-2}$. Therefore, a small variation of electron density due to applied periodic potential estimated above can not cause melting of WS for an infinite electron system. On the other hand, as was pointed out earlier the variation of lateral confinement of the electron system in the microchannel can cause loss of the long-range crystalline order in the quasi-1D WS due to the structural transitions between two stable configurations of the electron lattice corresponding to changing the number N_y of electron rows in the channel by one [39, 40]. This is exactly the mechanism that explains the phenomenon of re-entrant melting in this system. Therefore, one can expect that variation of N_y along the microchannel caused by the applied periodic potential can induce a similar loss of the long-range positional order, which in turn strongly changes the transport of electron system observed in the experiment. For $V_e = 0.92 \text{ V}$, $V_{sg} = -0.8 \text{ V}$, $V_{ch} = 1.5 \text{ V}$, and $\Delta V_F = 0.7 \text{ V}$ we estimate $\Delta N_y \approx 2$. In other words, the variation of confining potential due to applied periodic potential with $\Delta V_F = 0.7 \text{ V}$ is sufficient to cause the structural transition between N_y - and $(N_y + 1)$ -row configurations, which increases fluctuations in the positions of electrons and suppress nonlinear transport features usually associated with electron system in the long-range ordered WS phase.

5.4 Discussion

As shown in our work, the applied periodic potential has strong effect on transport of electron lattice, therefore our device can be used to study FK model in interaction system. Compared with the traditional FK model discussed in Sect. 5.1, the transport of WS system in our experiment is affected not only by the external periodic potential competing with the inter-electron interaction, but also the competing between WS and dimples. In fact, the interaction between the electron lattice and commensurate deformation of liquid surface has a loose analogy with FK model in the case when the mean distance between particles equals exactly to the spatial period of the substrate potential. This introduces additional physics into traditional FK model. In general, our system should be described by Hamiltonian

$$\hat{H} = \sum_i \frac{\hat{p}_i^2}{2m_e} + \hat{H}_{e-e} + \hat{H}_{e-b}, \quad (5.4)$$

where \hat{H}_{e-e} describes the inter-electron interaction, and \hat{H}_{e-b} represent the electron-background interaction. The background of SSE system above liquid helium, in particular at low temperature, is the 2D vibrations of the surface ripplons. When the SSE system is in the BC scattering regime, the DL will attribute a commensurate, periodic background potential such that the coupled WS-DL system acts like a 2D FK model. Indeed, coupled WS-DL system shows some typical features predicted by the FK model, such as a depinning transition, hysteresis, etc [58, 59]. The observed behavior of suppression of BC scattering due to the external periodic potential, may

represent an interesting issue of a substrate periodic potential composed of two characteristic periods.

The effects of external periodic potential on re-entrant melting have been observed in our experiments, see Fig. 5.6. The re-entrant melting, which results from competition between stable configurations corresponding to different numbers of electron rows, is particularly important in studies of finite-size crystalline systems where the spatial order of particles is strongly affected by their confinement [47]. The interplay between the electron lattice configuration and confining potential is an interesting problem of structural phase transitions [55]. In our experiment, the confinement is spatially modulated by the external periodic potential of varying strength. A characteristic feature of our observation in Fig. 5.6 is a certain (threshold) value of the amplitude of periodic potential above which the nonlinear transport of the electron system associated with its crystalline ordering is suppressed. Our estimations presented above show that this corresponds to about 10%-variation of the electron density in microchannel and variation of the number N_y of electron rows across the channel of the order one. More accurate estimations could be done by calculating the distribution of electrical potential and electron density across the microchannel (y -direction) using the FEM [40, 60]. However, to take a proper account for the granular nature of electrons the molecular dynamics (MD) calculation are preferable [47]. Therefore, we did not try to improve the continuous density approximation model used in the Sect. 5.3.1. The MD calculations for electron system in our device is currently under development.

As demonstrated here, the employed microchannel device can be used to study structural phase transitions in a quasi-1D electron systems; likewise, the device shows the potential for FK model study. As mentioned in our long-term motivation, we are interested to use similar devices to study the FK model employing a 1D chain of electrons subject to the periodic potential. Of particular interest is to realize an incommensurate case when the ratio of the mean distance between electrons to the spatial period of potential is equal to the "golden ratio", $(\sqrt{5} + 1)/2$. This is subject of our future experimental efforts.

5.5 Summary

We have investigated the transport properties of a WS on the surface of liquid helium confined in a long $5 \mu\text{m}$ -wide microchannel and subjected to an applied electrostatic potential with periodicity of $1 \mu\text{m}$ along the channel. The nonlinear features of WS transport were found to be suppressed by increasing the potential amplitude. We attribute this observation to structural transitions and suppression of the crystalline ordering of the electron system induced by the spatially modulated confinement.

Chapter 6

Electron flow in T-channel geometry

When a strongly-correlated system is driven by an external force, quite often it shows an unexpected strange behavior. In this last chapter, some intriguing and unexpected experimental observations on SSE transport in a T-shaped microchannel device is presented. The complete understanding of this observation is yet to be achieved.

6.1 Experiment

The microchannel device used in this study is shown in Fig. 6.1. The device is designed such that SSEs can flow between three reservoirs through a T-shaped microchannel structure. Each segment of T-shaped channel is $10\ \mu\text{m}$ -wide, $400\ \mu\text{m}$ -long, and $1\ \mu\text{m}$ -depth. The gaps between T-shaped channel bottom electrode and the reservoir bottom electrodes are $300\ \text{nm}$ -wide. A single guard electrode of the top layer is used for all three reservoirs and T-shaped channel.

In this experiment, the SSEs were driven by voltage ramp $V_{\text{in}}(t)$ applied to one of the reservoir electrodes, while the flow of electrons into/out of two other reservoirs was detected by the electrical currents induced by SSEs in the bottom electrodes of corresponding reservoirs. The induced currents were measured by a digital storage oscilloscope using current preamplifiers and averaged over 8000 ramp repetitions.

6.2 Results

First, the SSEs were driven out of and into the top reservoir R_{T} by applying a ramp of negative voltage ($V_{\text{in}} < 0$) to the bottom electrode of top reservoir as shown in Fig. 6.2 (a). The observed induced currents I_{L} and I_{R} at the left and right reservoirs, respectively, (the black and red traces in Fig. 6.2 (b)) due to SSEs flowing in and out into corresponding reservoirs are completely symmetric, as expected. The blue and green traces in Fig. 6.2 (b) are the values of the sum and difference, respectively, of currents I_{L} and I_{R} . According to the dc bias applied to the channel electrode and the guard electrode, the estimated electron density n_e is about $3.5 \times 10^{13}\ \text{m}^{-2}$, which corresponds to a melting temperature T_{M} of $1.3\ \text{K}$ and a saturated current I_{BC} of $0.4\ \text{nA}$ in the BC scattering region. Since $I = en_e w v$ and $I_{\text{T}} = I_{\text{L}} + I_{\text{R}}$, $v_{\text{L}} = v_{\text{R}} = \frac{1}{2}v_{\text{T}} = \frac{1}{2}v_{\text{BC}}$. Therefore, the current plateau at $0.4\ \text{nA}$ for the sum of I_{L}

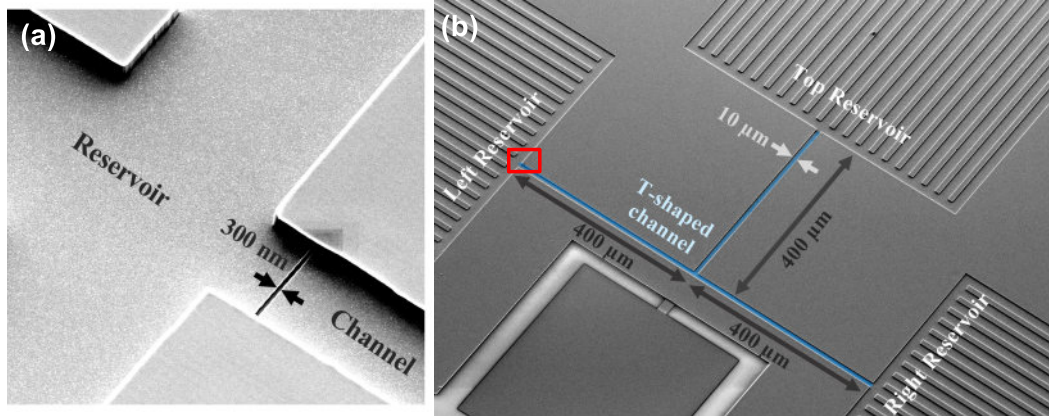


Figure 6.1: False-color scanning electron microscopic image of T-shaped microchannel device. The T-shaped microchannel is designed for SSEs to flow under the same geometry but in different orientations. It connects three reservoirs labeled as Left, Right and Top Reservoir as indicated in (b). An enlarged image of the area enclosed by the red rectangle in (b) is given in (a). It shows the gap between bottom electrodes of reservoir and T-shaped microchannel. The depth of microchannel is $1 \mu\text{m}$.

and I_R (the blue curve) implies that, although the SSEs in the whole T-channel are in solid phase, only the SSEs in the area between the top reservoir and adjacent junction are in the BC scattering regime. The difference of currents I_L and I_R (the green trace) is always zero, which shows that the current of SSEs splits equally into left and right channels, as expected.

Next, the same ramp of negative voltage was applied to the left reservoir R_L , while the induced currents I_T and I_R at the top and right reservoirs, respectively, were measured, as shown in Fig. 6.2 (c). Similar to the case of Fig. 6.2 (b), the sum $I_R + I_T$ (the blue curve) shows BC plateau of saturated current at 0.4 nA , which implies that the WS in the region between the left reservoir and adjacent junction is under the condition of BC scattering. However, the current of SSEs flowing into top and right reservoirs is not symmetric. Instead, we observed that the total current of electrons splits very asymmetrically between top and right reservoirs when pushed from the left reservoir, but flow symmetrically from the top and right reservoirs when pulled back into left reservoir (see Fig. 6.2 (c))ⁱ. The current difference $I_R - I_T$ (the green curve) clearly shows that, about $45 \mu\text{s}$ after start of the ramp up, all the SSE current from left reservoir flows into the right reservoir, while the current into top reservoir goes to zero. This unusual behavior lasts for about $50 \mu\text{s}$, after that the SSEs start to flow out of the right reservoir into the top reservoir. It is expected that as the SSEs are accumulating during the first $50 \mu\text{s}$ in the right reservoir, the resulted voltage difference between top and right reservoirs will cause a back flow of SSEs from right reservoir into the top reservoir until amount of SSEs in both reservoirs equalize.

When the voltage V_{in} at left reservoir is ramped back to zero, initially the current

ⁱSimilar asymmetry of electron flow is observed when voltage ramp is applied to right reservoir and currents at top and left reservoirs I_T and I_L are measured.

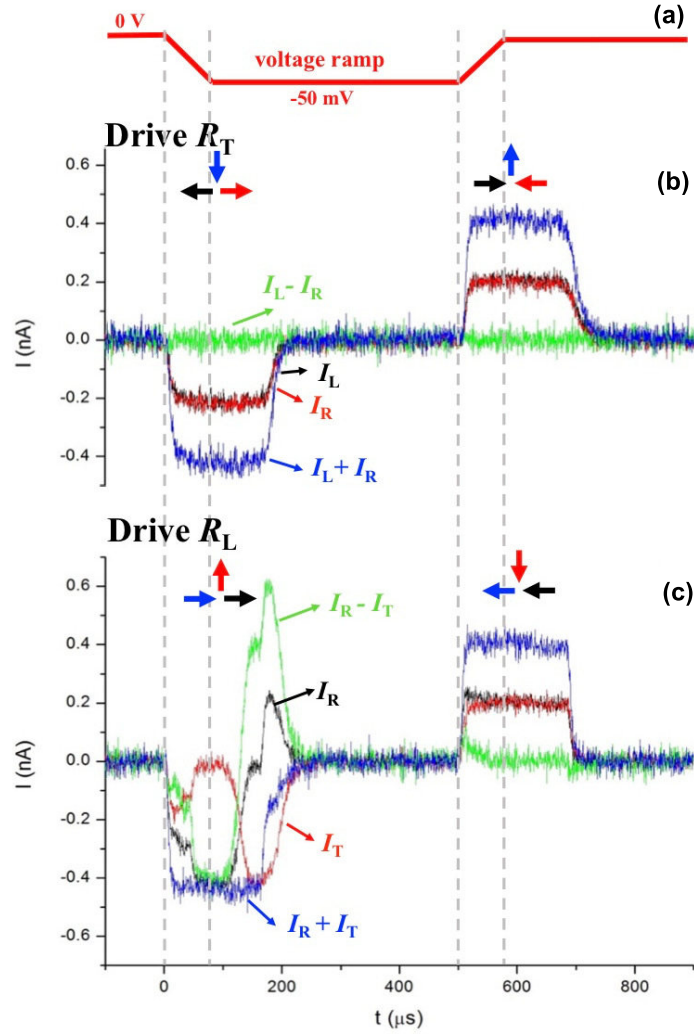


Figure 6.2: Flow of SSEs in T-channel at $T = 0.4$ K. (a) The applied negative ($V_{\text{in}} < 0$) voltage ramp plotted against time. (b) The measured induced currents at the left and right reservoirs I_L (black trace) and I_R (red trace) when the negative voltage ramp is applied to the top reservoir. The calculated sum and difference of induced currents, $I_L + I_R$ and $I_L - I_R$, are shown by the blue and green traces, respectively. (c) The measured current at the right and top reservoirs I_R (black trace) and I_T (red trace) when the negative voltage ramp is applied to the left reservoir. Similar to (b), the calculated sum and difference of induced currents, $I_L + I_R$ and $I_L - I_R$, are showed by the blue and green traces, respectively.

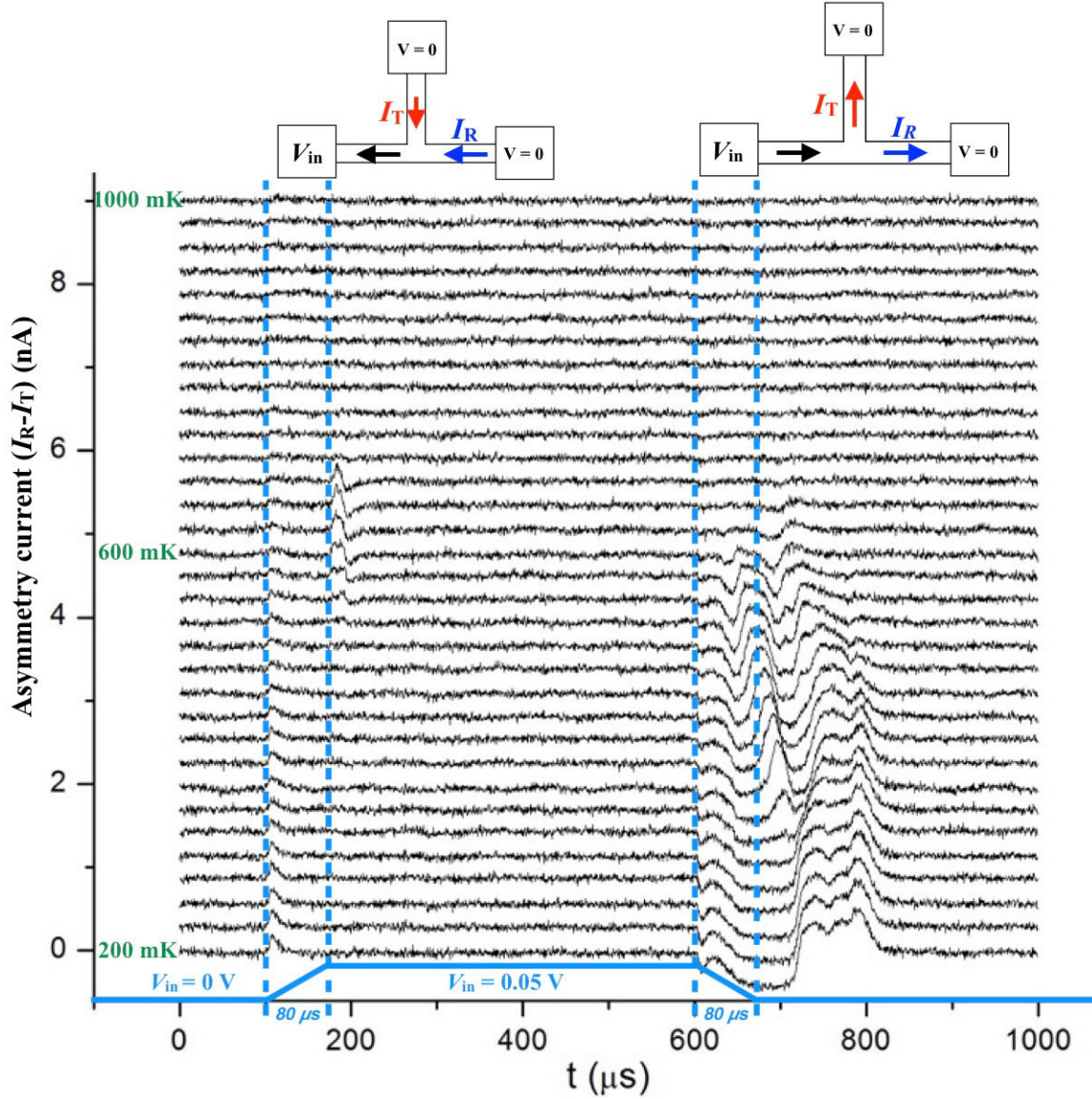


Figure 6.3: Temperature dependence of current difference $I_R - I_T$ when a positive ($V_{\text{in}} > 0$) voltage ramp is applied to the left reservoir. The current difference $I_R - I_T$ is given for different values of temperature. The estimated SSE density is $n_e \simeq 3.5 \times 10^{13} \text{ m}^{-2}$, which corresponds to the WS melting temperature $T_M \simeq 1.3 \text{ K}$.

I_R from the right reservoir is slightly larger than the current I_T from the top reservoir. However, the currents equalize quickly, and the overall flow of SSEs from the two reservoirs into the left reservoir is symmetric, see Fig. 6.2 (c). Similarly, when applying positive ($V_{\text{in}} > 0$) voltage ramp to left reservoir, we observe an almost symmetric flow of electrons from top and right reservoirs into the left reservoir and asymmetric flow of electrons when voltage is ramped back to zero.

The observed asymmetric flows also shows strong temperature dependence, which is shown in Fig. 6.3 for the case of applying positive ($V_{\text{in}} > 0$) voltage ramp to the left reservoir. Here, we plot the current difference $I_L - I_T$ for different temperatures from 200 mK to 1000 mK. Note that the asymmetry starts to disappear at around 600 mK, while the melting temperature of WS is expected to be $T_M > 1$ K.

6.3 Discussion

The observed behavior of SSE flow in the T-shaped microchannel is intriguing. The effect seems to appear only when there is an asymmetry in the orientation of electron flow, which suggests that the inertia of the driven system plays an important role in this experiment.

We propose one possible scenario for the observed behavior. The fact that the asymmetric flow of electrons happen at sufficiently high electron densities and low temperatures suggests that the dynamics of the BC scattering and coupling of WS to the dimple lattice plays important role. As discussed in the previous section, in the case of symmetric flow when the current of electrons splits equally between two reservoirs, SSEs are expected to be deep in the BC scattering regime only at the entrance of the T-shaped junction (let's say from the top reservoir). This suggests that SSEs are essentially free of dimples as they enter the two reservoirs (left and right). Oppositely, in the case of an asymmetric flow, SSEs flow mainly in the straight direction, which means that they enter the corresponding reservoir being deep in the BC scattering regime. This suggests that the observed behavior can be associated with the effect of inertia of the dimple lattice that carries the WS through the T-shaped junction predominantly in the straight direction.

While this explanation seems to be natural, it is surprising that the asymmetry in the SSE flow, which we attribute to the inertia of the dimples, disappear at temperatures well below the melting temperature of WS. However, it is important to consider also a strong temperature dependence of the ripplon damping rate, γ_{G_1} , and the corresponding amplitude of the DL, see Eq. (4.9) and Eq. (4.7) in Chapter 4. As temperature decreases, the damping rate rapidly decreases as T^4 . For $T \approx 0.8$ K, we estimated $\gamma_{G_1}^{-1} \approx 1 \mu\text{s}$. At such temperature, if SSEs free themselves from DL as they move through the T-shaped junction, the DL disappear on the same timescale of $\gamma_{G_1}^{-1} \approx 1 \mu\text{s}$ due to dissipation of ripplon energy into phonons of bulk liquid. This time is comparable with the typical time for the electrons to travel through the junction. As the temperature decreases, the typical time over which the uncoupled DL dissipates rapidly increases and can exceed the time during which SSEs travel through the junction, thus the dimples can trap the SSEs again. As a result, only at sufficiently low temperatures SSEs remain to be bound to the DL and show asymmetric transport

associated with DL inertia.

6.4 Summary

We have investigated the transport properties of SSEs in a T-shaped microchannel. No asymmetry in the split electron flows is observed when electrons are pushed out of or pulled into the top reservoir. Moreover, almost no flow asymmetry is observed when electrons are pulled from the T-shaped channel into either the left or right reservoir. However, there appears a strong asymmetry in the split electron flows when electrons are pushed into the T-shaped channel from either the left or right reservoir. From the analysis of the asymmetric flow, one can conclude that electrons prefer flowing straight rather than turn at the junction. We suspect that the observed SSE asymmetric flows are caused by the DL inertia which is sufficient to carry the WS through the T-shaped junction in the straight direction. The observed temperature dependence can be explained by the slow decay of uncoupled DL at low temperature, which thus can re-trap the WS. In a way, the re-trapping process is akin to inverse BC scattering where WS can reabsorb the energy of resonant ripplons ⁱⁱ. A more rigorous theoretical study of re-trapping process is required.

ⁱⁱThe concept of both the DL emission and absorption has already been mentioned in Dykman & Rubo's original work: "The Bragg-Cherenkov scattering is a coherent many-electron emission or absorption of vibrational excitations" [?].

Conclusion

As mentioned in the beginning of this thesis, electrical transport in strongly correlated electron systems is an important subject to study in order to understand fascinating phenomena in modern condensed matter and solid state physics, such as conventional and high-Tc superconductivity, the fractional Hall effect, melting of 2D electron crystals, etc. In this thesis we described a few experiments aimed at further studies of transport properties of a 2D electron crystal confined in microstructures. Some new intriguing phenomena, which need further studies and theoretical developments, were already observed in the experiments described here. More importantly, these works show viability and advantages to use the developed microchannel devices to study fascinating transport properties of SSEs on liquid helium. As a conclusion of this thesis, we outline some future plans.

In the described work, we mostly concentrated on the transport of an electron crystal, the Wigner solid, on liquid helium. However, the electrical transport of electron liquid could be also a very interesting subject of research. In particular, because for sufficiently high electron densities of such liquid and low enough temperatures the electron-electron collision time can greatly exceed the momentum relaxation time due to collisions with background scatterers, such a liquid can show hydrodynamic behaviour, as was demonstrated for example in 2D electrons in graphene [61–63]. The key point for possibility to observe hydrodynamic effects in the flow of electrons in graphene was an appropriate geometry of a sample. The flexibility in manufacturing the microchannel devices used in our experiments allows us to design a proper geometry of the device where hydrodynamic features of electron flow in SSE liquid could be observed. For example, we do not exclude possibility that some hydrodynamic features of electron flow, such as vorticity, could be also responsible for the unusual transport of SSEs in the T-channel geometry as was described in Chapter 6. This is certainly a very interesting and new direction of research to pursue further.

As was described in Chapter 5, our motivation to study transport of WS subject to a spatially periodic potential comes from the possibility to use SSE system to simulate the FK model. In our experiments we realized a case of about four electrons per period of the spatial potential. A more clear-cut and interesting case would be to have a single particle per period to study effect of commensurability. It would be also advantageous to carry out such experiments with electron liquid rather than WS to avoid effects of strong coupling of WS to the commensurate deformation of the surface of liquid helium, as well as use a single chain of electrons in a microchannel rather than a 2D system. Such experiments require further developments in device manufacturing, in particular employing a shallow channels with height below 200 nm.

While all experiments described here were done with the many-electron system, our original motivations to employ microchannel devices for experiments with SSEs on liquid helium also come from the possibility of trapping and detecting a single electron in the microchannel. Such work is mostly driven by the proposals to employ electrons on helium to build qubits for a scalable quantum computer architecture [64–67]. While this is a very challenging task, the possibility of single-electron detection on liquid helium has been already demonstrated using a single-electron transistor (SET) device [68, 69]. Employing a suitable microchannel geometry might provide some advantages for control of the number of electrons, as was already demonstrated by Rees *et al.* in experiments with a point contact device [36, 70]. Trapping of a single electron in the microchannel (subsequent detection of its quantum states) is one of the key points for successful implementation of SSEs on liquid helium for qubits.

Bibliography

- [1] A. O. Badrutdinov, A. V. Smorodin, D. G. Rees, J. Y. Lin, and D. Konstantinov, *Physical Review B* **94**, 195311 (2016).
- [2] J.-Y. Lin, A. V. Smorodin, A. O. Badrutdinov, and D. Konstantinov, *Physical Review B* **98**, 085412 (2018).
- [3] J. Quintanilla and C. Hooley, *Physics World* **22**, 32–37 (2009).
- [4] I. García-Mata, O. V. Zhirov, and D. L. Shepelyansky, *The European Physical Journal D* **41**, 325–330 (2007).
- [5] A. Bylinskii, D. Gangloff, and V. Vuletic, *Science* **348**, 1115 (2015).
- [6] A. Vanossi, N. Manini, M. Urbakh, S. Zapperi, and E. Tosatti, *Reviews of Modern Physics* **85**, 529–552 (2013).
- [7] K. K. Y. Monarkha, *Two-Dimensional Coulomb Liquids and Solids*, Springer, Berlin, Heidelberg (2004).
- [8] E. Y. Andrei, *Electrons on Helium and Other Cryogenic Substrates*, Kluwer Academic, Dordrecht (1997).
- [9] M. W. Cole and M. H. Cohen, *Physical Review Letters* **23**, 1238 (1969).
- [10] V. B. Shikin, *Soviet Journal of Experimental and Theoretical Physics* **31**, 936 (1970).
- [11] R. Mehrotra, C. J. Guo, Y. Z. Ruan, D. B. Mast, and A. J. Dahm, *Physical Review B* **29**, 5239 (1984).
- [12] W. T. Sommer, *Physical Review Letters* **12**, 271 (1964).
- [13] B. Burdick, *Physical Review Letters* **14**, 11 (1965).
- [14] C. C. Grimes and G. Adams, *Physical Review Letters* **36**, 145 (1976).
- [15] L. D. Landau and E. M. Lifshitz, *Quantum mechanics: non-relativistic theory*, Butterworth-Heinemann, 3rd edition (2003).
- [16] R. S. Crandall, *Physical Review A* **6**, 790 (1972).
- [17] P. M. Platzman and G. Beni, *Physical Review Letters* **36**, 626 (1976).

-
- [18] M. Saitoh, *Journal of the Physical Society of Japan* **42**, 201 (1977).
- [19] R. Kubo, *Reports on Progress in Physics* **29**, 255 (1966).
- [20] G. F. Giuliani and G. Vignale, *Quantum theory of the electron liquid*, Cambridge university (2005).
- [21] T. R. Brown and C. C. Grimes, *Physical Review Letters* **29**, 1233 (1972).
- [22] K. Shirahama, S. Ito, H. Suto, and K. Kono, *Journal of Low Temperature Physics* **101**, 439–444 (1995).
- [23] T. Ando, *Journal of the Physical Society of Japan* **44**, 765 (1978).
- [24] V. A. Buntar, V. N. Grigoriev, O. I. Kirichek, Y. Z. Kovdrya, Y. P. Monarkha, and S. S. Sokolov, *Journal of Low Temperature Physics* **79**, 323–339 (1990).
- [25] E. Wigner, *Physical Review* **46**, 1002 (1934).
- [26] Y. P. Monarkha and V. B. Shikin, *Soviet Journal of Experimental and Theoretical Physics* **41**, 710 (1975).
- [27] K. Shirahama and K. Kono, *Physical Review Letters* **74**, 781 (1995).
- [28] S. P. Denisov, *Physics-Uspekhi* **50**, 377–379 (2007).
- [29] I. Frank and I. Tamm. *Coherent Visible Radiation of Fast Electrons Passing Through Matter*, pages 29–35. Springer Berlin Heidelberg, Berlin, Heidelberg, (1991).
- [30] J. D. Jackson, *Classical Electrodynamics*, John Wiley and Sons, 3rd edition (1999).
- [31] A. Kristensen, K. Djerfi, P. Fozooni, M. J. Lea, P. J. Richardson, A. Santrich-Badal, A. Blackburn, and R. W. van der Heijden, *Physical Review Letters* **77**, 1350 (1996).
- [32] K. Shirahama and K. Kono, *Journal of Low Temperature Physics* **104**, 237–264 (1996).
- [33] D. G. Rees, N. R. Beysengulov, J. J. Lin, and K. Kono, *Physical Review Letters* **116**, 206801 (2016).
- [34] W. F. Vinen, *Journal of Physics: Condensed Matter* **11**, 9709 (1999).
- [35] F. R. Bradbury, M. Takita, T. M. Gurrieri, K. J. Wilkel, K. Eng, M. S. Carroll, and S. A. Lyon, *Physical Review Letters* **107**, 266803 (2011).
- [36] D. G. Rees, I. Kuroda, C. A. Marrache-Kikuchi, M. Hofer, P. Leiderer, and K. Kono, *Physical Review Letters* **106**, 026803 (2011).
- [37] D. G. Rees, I. Kuroda, C. A. Marrache-Kikuchi, M. Höfer, P. Leiderer, and K. Kono, *Journal of Low Temperature Physics* **166**, 107–124 (2012).

-
- [38] H. Ikegami, H. Akimoto, and K. Kono, *Physical Review B* **82**, 201104(R) (2010).
- [39] H. Ikegami, H. Akimoto, D. G. Rees, and K. Kono, *Physical Review Letters* **109**, 236802 (2012).
- [40] D. G. Rees, H. Ikegami, and K. Kono, *Journal of the Physical Society of Japan* **82**, 124602 (2013).
- [41] H. Ikegami, H. Akimoto, and K. Kono, *Journal of Physics: Conference Series* **400**, 012020 (2012).
- [42] J. Klier, A. Würfl, P. Leiderer, G. Mistura, and V. Shikin, *Physical Review B* **65**, 165428 (2002).
- [43] A. Valkering, J. Klier, and P. Leiderer, *Physica B: Condensed Matter* **284-288**, 172–173 (2000).
- [44] H. Ikegami, H. Akimoto, and K. Kono, *Journal of Low Temperature Physics* **179**, 251–263 (2015).
- [45] D. G. Rees, S.-S. Yeh, B.-C. Lee, K. Kono, and J.-J. Lin, *Physical Review B* **96**, 205438 (2017).
- [46] Y. P. Monarkha and K. Kono, *Low Temperature Physics* **35**, 356–364 (2009).
- [47] D. G. Rees, N. R. Beysengulov, Y. Teranishi, C.-S. Tsao, S.-S. Yeh, S.-P. Chiu, Y.-H. Lin, D. A. Tayurskii, J.-J. Lin, and K. Kono, *Physical Review B* **94**, 045139 (2016).
- [48] P. Roche, G. Deville, K. O. Keshishev, N. J. Appleyard, and F. I. B. Williams, *Physical Review Letters* **75**, 3316 (1995).
- [49] P. Roche, M. Roger, and F. I. B. Williams, *Physical Review B* **53**, 2225 (1996).
- [50] G. Grüner, *Reviews of Modern Physics* **60**, 1129 (1988).
- [51] S. C. Ying, *Physical Review B* **3**, 4160 (1971).
- [52] H. Z. Cummins, *Physics Reports* **185**, 211–409 (1990).
- [53] C. Reichhardt, C. J. Olson, N. Grønbech-Jensen, and F. Nori, *Physical Review Letters* **86**, 4354 (2001).
- [54] B. Bhushan, J. N. Israelachvili, and U. Landman, *Nature* **374**, 607–616 (1995).
- [55] S. Fishman, G. D. Chiara, T. Calarco, and G. Morigi, *Physical Review B* **77**, 064111 (2008).
- [56] K. Moskovtsev and M. Dykman, APS March Meeting **K45.00002**, <https://meetings.aps.org/Meeting/MAR18/Session/K45.2> (2018).
- [57] S. N. Coppersmith and D. S. Fisher, *Physical Review B* **28**, 2566 (1983).

-
- [58] A. Vanossi, N. Manini, F. Caruso, G. E. Santoro, and E. Tosatti, *Physical Review Letters* **99**, 206101 (2007).
- [59] C.-L. Wang, W.-S. Duan, X.-R. Hong, and J.-M. Chen, *Applied Physics Letters* **93**, 153116 (2008).
- [60] H. Ikegami, H. Akimoto, and K. Kono, *Journal of Low Temperature Physics* **179**, 251 (2015).
- [61] D. A. Bandurin, I. Torre, R. K. Kumar, M. Ben Shalom, A. Tomadin, A. Principi, G. H. Auton, E. Khestanova, K. S. Novoselov, I. V. Grigorieva, and et al., *Science* **351**, 1055–1058 (2016).
- [62] J. Zaanen, *Science* **351**, 1026–1027 (2016).
- [63] L. Levitov and G. Falkovich, *Nature Physics* **12**, 672–676 (2016).
- [64] P. M. Platzman and M. I. Dykman, *Science* **284**, 1967 (1999).
- [65] M. I. Dykman, P. M. Platzman, and P. Seddighrad, *Physical Review B* **67**, 155402 (2003).
- [66] S. A. Lyon, *Physical Review A* **74**, 052338 (2006).
- [67] D. I. Schuster, A. Fragner, M. I. Dykman, S. A. Lyon, and R. J. Schoelkopf, *Physical Review Letters* **105**, 040503 (2010).
- [68] G. Papageorgiou, P. Glasson, K. Harrabi, V. Antonov, E. Collin, P. Fozooni, P. G. Frayne, M. J. Lea, D. G. Rees, and Y. Mukharsky, *Applied Physics Letters* **86**, 153106 (2005).
- [69] E. Rousseau, D. Ponarin, L. Hristakos, O. Avenel, E. Varoquaux, and Y. Mukharsky, *Physical Review B* **79**, 045406 (2009).
- [70] D. G. Rees, H. Totsuji, and K. Kono, *Physical Review Letters* **108**, 176801 (2012).